# Novel Vision Based Estimation Techniques for the Analysis of Cavitation Bubbles

by

Gökhan Alcan

**Submitted to**
**the Graduate School of Engineering and Natural Sciences**
**in partial fulfillment of**
**the requirements for the degree of**
**Master of Science**

**SABANCI UNIVERSITY**

August, 2015

Novel Vision Based Estimation Techniques for the Analysis of Cavitation Bubbles

Gökhan Alcan

APPROVED BY

Prof. Dr. Mustafa Ünel ..............................................
(Thesis Supervisor)

Assoc. Prof. Dr. Ali Koşar ..............................................

Assist. Prof. Dr. Hüseyin Üvet ..............................................

DATE OF APPROVAL: ..............................................

Novel Vision Based Estimation Techniques for the
Analysis of Cavitation Bubbles

Gökhan Alcan

ME, Master's Thesis, 2015

Thesis Supervisor: Prof. Dr. Mustafa Ünel

**Keywords:** Cavitation Bubbles, Cone Angle Estimation, Kalman Filter, Image Segmentation, Visual Tracking, Elliptic Fourier Descriptors

## Abstract

Visualization and analysis of micro/nano structures throughout multiphase flow have received significant attention in recent years due to remarkable advances in micro imaging technologies. In this context, monitoring bubbles and describing their structural and motion characteristics are crucial for hydrodynamic cavitation in biomedical applications.

In this thesis, novel vision based estimation techniques are developed for the analysis of cavitation bubbles. Cone angle of multiphase bubbly flow and distributions of scattered bubbles around main flow are important quantities in positioning the orifice of cavitation generator towards the target and controlling the destructive cavitation effect. To estimate the cone angle of the flow, a Kalman filter which utilizes 3D Gaussian modeling of multiphase flow and edge pixels of the cross-section is implemented. Scattered bubble swarm distributions around main flow are assumed to be Gaussian and geometric properties of the covariance matrix of the bubble position data are exploited. Moreover, a new method is developed to track evolution of single, double and triple rising bubbles during hydrodynamic cavitation. Proposed tracker fuses shape and motion features of the individually detected bubbles and employs the well-known Bhattacharyya distance. Furthermore, contours of the tracked bubbles are modeled using elliptic Fourier descriptors (EFD) to extract invariant properties of single rising bubbles throughout the motion. To verify the proposed techniques, hydrodynamic cavitating bubbles are generated under 10 to 120 bars inlet pressures and monitored via Particle Shadow Sizing (PSS) technique. Experimental results are quite promising.

Kavitasyon Kabarcıklarının Analizi için Görmeye Dayanan
Özgün Kestirim Teknikleri

Gökhan Alcan

ME, Master Tezi, 2015

Tez Danışmanı: Prof. Dr. Mustafa Ünel

**Anahtar kelimeler:** Kavitasyon Kabarcıkları, Koni Açısı Kestirimi, Kalman Süzgeci, Görüntü Bölütleme, Görsel Takip, Eliptik Fourier Tanımlayıcıları

# Özet

Mikro görüntüleme teknolojilerindeki kayda değer gelişmeler sayesinde mikro/nano yapıların çok fazlı akış boyunca görüntülenmesi ve analizi son yıllarda oldukça ilgi görmüştür. Bu bağlamda, kabarcıkların izlenmesi ve onların yapısal ve hareket karakteristiklerinin tanımlanması biyomedikal uygulamalardaki hidrodinamik kavitasyon için oldukça önemlidir.

Bu tezde, kabarcıklı kavitasyonun analizi için görme tabanlı özgün kestirim teknikleri geliştirilmiştir. Çok fazlı kabarcıklı akışın koni açısı ve ana akış etrafındaki saçılmış kabarcıkların dağılımları kavitasyon üreticisinin ağzını hedefe doğru pozisyonlamada ve tahrip edici kavitasyon etkisini kontrol etmede oldukça önemli niceliklerdir. Akışın koni açısını kestirmek için çok fazlı akış 3B Gaussian olarak modellenmiş ve ara kesitin kenar piksellerinden faydalanan Kalman süzgeci uygulanmıştır. Ana akış etrafında saçılmış kabarcık sürü dağılımlarının Gaussian olduğu varsayılıp kabarcık pozisyon verilerinin kovaryans matrisinin geometrik özelliklerinden faydalanılmıştır. Dahası, hidrodinamik kavitasyon boyunca tekli, ikili ve üçlü doğan kabarcıkların gelişimini takip etmek için yeni bir yöntem geliştirilmiştir. Önerilen takip edici, bireysel tespit edilen kabarcıkların şekil ve hareket özelliklerini birleştirmekte ve iyi bilinen Bhattacharyya mesafesini kullanmaktadır. Ayrıca, takip edilen kabarcıkların dış hatları tekli doğan kabarcıkların hareket boyunca değişmeyen özelliklerini çıkarmak için eliptik Fourier tanımlayıcılar (EFD) kullanılarak modellenmiştir. Önerilen teknikleri doğrulamak için, hidrodinamik kavitasyon kabarcıkları 10 - 120 bar giriş basınçları altında üretilmiş ve parçacık gölge boyutlama tekniğiyle izlenmiştir. Deneysel sonuçlar oldukça umut vericidir.

# *Acknowledgements*

It is a great pleasure to express my sincere gratitude and indebtedness to my thesis advisor Prof. Dr. Mustafa Unel for his priceless academic and personal guidance, consistent moral and material support, motivation and immense knowledge. His unique supervision has widened and shaped my research perspective. I feel myself lucky for having a chance to develop my world-view and form a regular working discipline in the light of his stimulating advises and encouragements.

I would gratefully thank Assoc. Prof. Dr. Ali Koşar and Assist. Prof. Dr. Hüseyin Üvet for spending their valuable time to serve as my jurors. It was also an honour for me to work with them in the same project.

I would like to acknowledge the financial support provided by The Scientific and Technological Research Council of Turkey (TUBITAK) through the project "Hidrodinamik Kavitasyona Dayanan Medikal Uygulamalar için Kullanılacak Ulusal Endoskopik Cihaz Tasarımı ve Geliştirilmesi" under the grant 113S092.

I would like to thank every single member of Control, Vision and Robotics research group. Many thanks to Talha Boz, Sanem Evren, Ahmet Eren Demirel and Fırat Yavuz for their help and sharing all they know; to Morteza Ghorbani for excellent collaboration in the same TUBITAK project, Gökay Çoruhlu, Mert Gülhan and Ugur Sancar for useful discussions and special thanks to Orhan Ayit.

I would like to thank my precious parents Ramazan and Nezahat and my beloved sister Gülşah for their invaluable love, caring and never ending support from the beginning of my life.

Finally, I would like to thank my fiancee Fatoş Olgun for her priceless love, encouragement and support throughout my graduate education.

# Contents

# List of Figures

# List of Tables

# List of Algorithms

# Chapter 1

# Introduction

Richard Feynman talked about the problems and possibilities of small (and even atomic) scale manipulation and control in 1959. According to him, physical rules in atomic level could be very distinctive, so different forces and effects may exist that we don't encounter in macro world. In his famous talk, he expressed his expectations about exploring the atomic level possibilities with developing technology [4]. His foresighted considerations could be realized after 20 years with advancements in micro electro mechanical systems (MEMS) [5] and recent technological developments enable us to search for atomic level structures.

In addition to atomic level manipulation and control, investigation and intervention of micro/nano fluidics have gained excessive attention in recent years. Designs of micro fluidic channel structures contribute to achieve several micron level tasks such as micro-manipulation, micro-fabrication, micro-assembly, micro-sensing and micro-actuation. Micro fluidic studies are older than Feynman's talk. One of the most well-known and oldest micro fluidic experiments belongs to Reynolds [6]. His experiments were based on pipe flow that was driven by pressure and he explained the transition to turbulence.

## 1.1 Motivation

After 2000, interest and research studies about micro/nano fluidics rose rapidly and became an important constituent in both academia and industry. Micro fluidics based structures are employed in several industrial applications such as 2D/3D printers, agglutination machines and electronic cooling devices. In literature, specialized forms of microchannels as Lab-on-Chip (LOC) or biochips are used in biology to investigate the cell behaviours under various conditions and find possible diagnostics. Figure 1.1 shows the published patents and journal articles to demonstrate the ascending interest in microfluidics research study and an increasing potential in commercial applications.

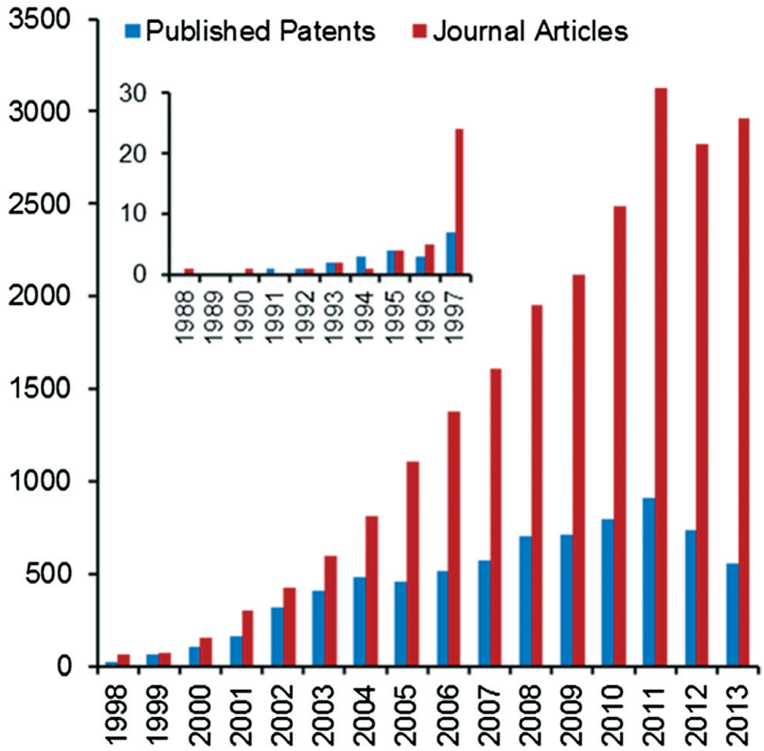


FIGURE 1.1: Published patents and journal articles about microfluidics until 2013 [1]

Visualization of the microfluidic process has an extreme importance on making progress in research studies and developing novel products in industrial applications. Many microscale visualization systems aim to extract the velocity fields, profiles and motion of the flow [7]. Advances in visualization components such as power LEDs and lasers as illumination sources, high speed CCD and CMOS cameras as capturing elements, advance image and video processing algorithms and high computational capabilities allow to design sophisticated imaging system architectures. Particle Image Velocimetry, Laser/Phase Doppler Anemometry, Interferometric Particle Imaging and Particle Shadow Sizing architectures are most commonly preferred techniques depending on the needs of applications.

Hydrodynamic cavitation is a specialized form of multiphase flow which occurs when flow is exposed to sudden pressure change [2]. Cavitation-induced bubbles are unwanted due to their destructive effect. Recent research studies [2, 8] employ devastating hydrodynamic cavitation bubbles in biomedical applications. Therefore, visualization of hydrodynamic cavitation phenomenon with several up-to-date imaging technologies and analysis of cavitation caused bubbles with advanced computer vision algorithms are very evocatory.

## 1.2 Contributions of the thesis

This thesis aims to design a visualization system architecture for monitoring hydrodynamic cavitation and proposes particular solutions to the analysis of cavitation bubbles for employing this multiphase phenomenon in biomedical applications. In the first part of the thesis, Kalman filter based virtual cone angle estimation is presented in order to position the orifice of bubbly flow generator effectively. To control the destructive cavitation effect, scattered bubble swarms distributions around the main flow is analyzed by utilizing the covariance matrix of bubble positions data. In the second part, a new tracking by detection method is developed by utilizing the morphological and motion characteristics of individually detected bubbles. Fusion of shape and motion features are employed in well-known Bhattacharyya distance to provide a robust tracker. Evolutions of single, double and triple rising bubbles are tracked and analyzed during hydrodynamic cavitation. In the third part, contour edges of previously tracked single bubbles are modeled using elliptic Fourier descriptors (EFD) to extract invariant properties throughout the motion.

## 1.3 Outline of the thesis

**Chapter 2** explains hydrodynamic cavitation phenomenon, demonstrates several micro/nano imaging systems including the implemented Particle Shadow Sizing (PSS). Then, an overview of segmentation and tracking algorithms with specialized to bubble tracking as well are presented. **Chapter 3** is on visual analysis of cavitation flow. In this context, Kalman filter based multiphase bubbly flow cone angle estimation and scattered bubble distribution modeling are proposed. **Chapter 4** introduces a new single, double and triple cavitation bubbles tracker that utilizes structure and motion information. In **Chapter 5**, contour edges of single tracked bubbles are modeled using elliptic Fourier descriptor. **Chapter 6** is on the experimental results which are implemented on the images of hydrodynamic cavitating bubbles generated under 10 to 120 bars inlet pressures. Finally thesis is concluded in **Chapter 7** and possible future works are discussed.

## 1.4 Publications

- G. Alcan, M. Ghorbani, A. Kosar, M. Unel, "Vision Based Cone Angle Estimation of Bubbly Cavitating Flow and Analysis of Scattered Bubbles using Micro Imaging Techniques", *41st Annual Conference of the IEEE Industrial Electronics Society* (IECON 2015), Yokohama, Japan, November 9-12,2015

- M. Ghorbani, G. Alcan, D. Yilmaz, M. Unel, A. Kosar, "Visualization and image processing of spray structure under the effect of cavitation phenomenon", *9th International Symposium on Cavitation* (CAV 2015), EPFL, Lausanne, Switzerland, December 6-10, 2015

- M. Ghorbani, G. Alcan, S. E. Yalcin, Z. Zhakypov, M. Unel, D. Gozuacik, S. Ekici, H. Uvet, A. Sabanovic, A. Kosar, "Visualization of Microscale Bubbly Cavitation Flow via Particle Shadow Sizing Imaging and Vision Based Estimation of the Cone Angle", Journal Paper (**under preparation**)

# Chapter 2

# Literature Survey and Background

## 2.1 Hydrodynamic Cavitation Phenomenon

Sudden pressure drop down below the vapor pressure of the liquid results in vaporization and bubble generation. This phenomenon is called hydrodynamic cavitation. When a liquid flowing through an inlet channel is exposed to pass through the micro orifice throat, velocity of the flow increases and subsequently decrease in pressure causes formation of gas bubbles [2]. Several research studies enable physical explanations, applications and visualizations of hydrodynamic cavitation [9–13].

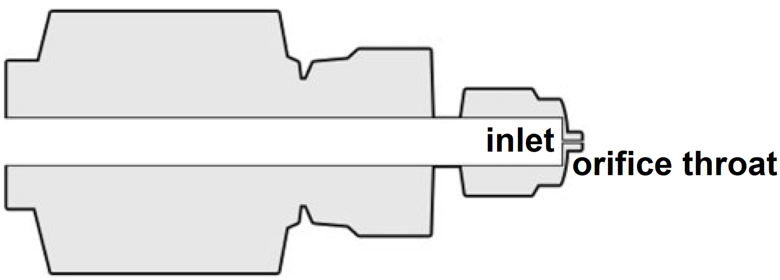


Figure 2.1: Hydrodynamic cavitation generator microchannel [2]

Generated bubbles in lower inlet pressure, may collapse when they are subjected to atmospheric pressure. Highly destructive shock waves are generated by the collapse of cavitation-caused bubbles. Continuous collision of solid surfaces and generated bubbles leads to cavitation erosion [14].

Destructive effect of hydrodynamic cavitation is normally undesirable and must be minimized in machines closely interact with liquids such as ships' propellers and hydraulic turbines [15]. Turning destructive effect into an advantage is possible in many biological and biomedical applications. Perk et. al [2] utilized hydrodynamic cavitation as a tool in kidney stone erosion and showed that hydrodynamic cavitation can be used as an alternative in biomedical applications. Similarly, prostate cells are killed and benign prostatic hyperplasia tissue is ablated by hydrodynamic cavitation in [8].

Gogate and Pandit [16] present the future of hydrodynamic cavitation within the context of hydrodynamic cavitation reactors design, modeling and analysis of bubble dynamics and cavitation yields, investigation of bubble-bubble and bubble-flow interactions.

## 2.2 Micro/Nano Visualization Systems

### 2.2.1 Particle Image Velocimetry (PIV)

Particle Image Velocimetry (PIV) is a measurement technique that provides instantaneous velocity fields of the particles during the flow motion [17, 18]. To visualize the flow velocity, micron sized small particles called "seeding" are mixed into the fluid which reflect the light and enable to monitor the motion (Figure 2.2). Tracer particles are captured in consecutive frames and local displacements are calculated with several correlation techniques [19]. By utilizing the fundamental speed definition as derivative of positions, high accuracy velocity fields are obtained with the help of precise calibration and exact correlations.

Generally fluid is illuminated with a plane light sheet source which provides to obtain 2 component velocity vectors in cross-section of the flow (Figure 2.3). Since

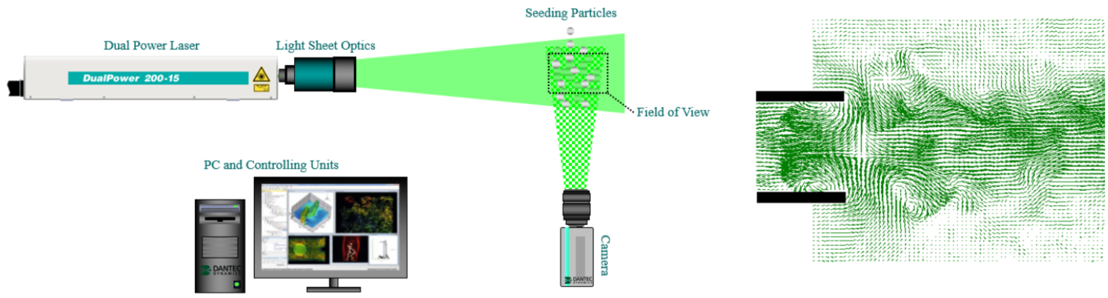


FIGURE 2.2: PIV configuration and obtained example velocity fields [3]

flow motion can be very fast, power LEDs or more preferably high power lasers are used to illuminate tracers. To increase the accuracy of velocity fields, double pulsed led or laser sources are preferred to obtain double consecutive frames with a few nano seconds delays.

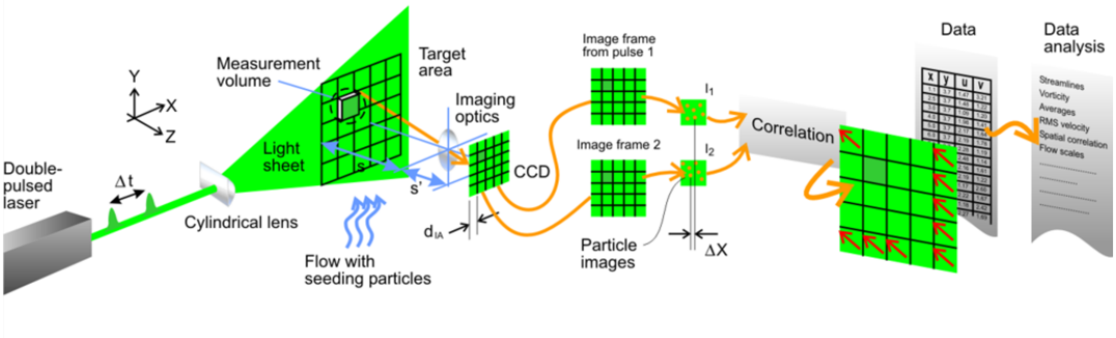


FIGURE 2.3: PIV measurement principles [3]

High frequency illumination sources necessitate the high speed cameras. Recent advances in imaging technologies such as high speed CCS and CMOS cameras make it possible to acquire real-time velocity maps [20].

Since classical PIV provides only 2 component velocity map in a plane, the visualization can be enhanced by utilizing more cameras with different configurations (Figure 2.4). Stereoscopic PIV provides three velocity components but the velocities still belong to a plane by employing 2 cameras appropriately [21, 22].

During PIV and Stereo PIV measurements, particle correlation accuracy may lessen due to partial or fully occlusions. A tracer particle detected in one frame may not be detected in the following frame as well. To recover the positions of almost each tracer seedings, particles should be followed in a volume instead of a plain. Volumetric PIV includes more than 2 cameras (ideally four) to achieve three velocity components in a volume, not a plain [23].

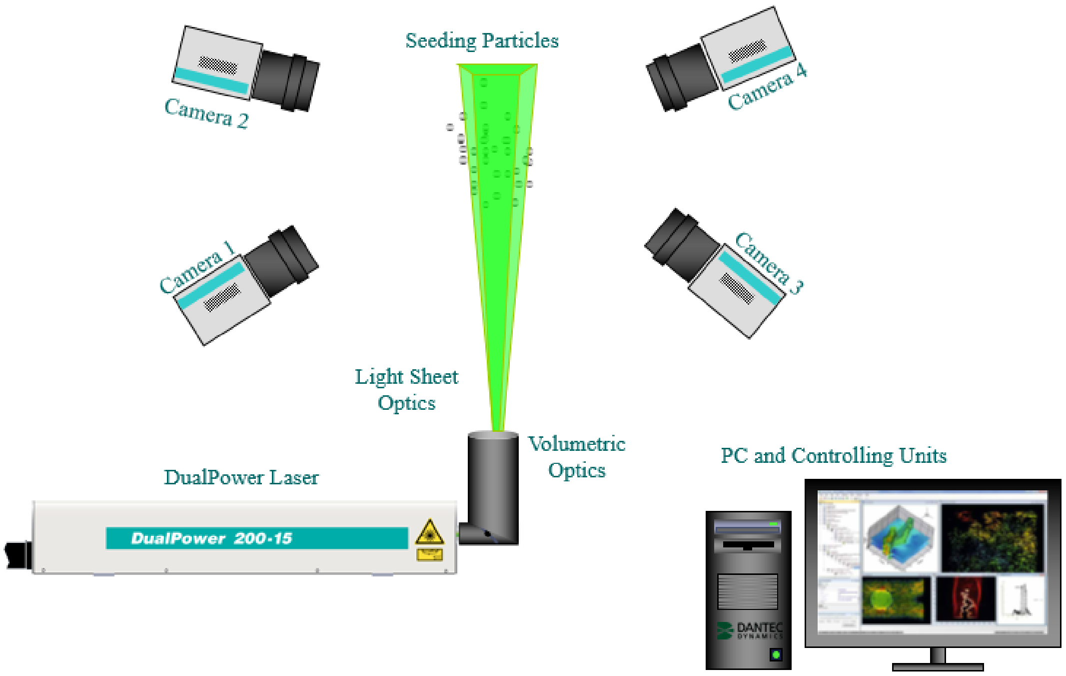


FIGURE 2.4: Stereo PIV (2 cam.), Volumetric PIV (4 cam.) Configurations [3]

### 2.2.2 Laser Doppler Anemometry (LDA)

Laser Doppler Anemometry (LDA), also known as Laser Doppler Velocimetry (LDV) utilizes well-known Doppler shift effect in laser beam to measure the velocity of gas or fluid flows [24].

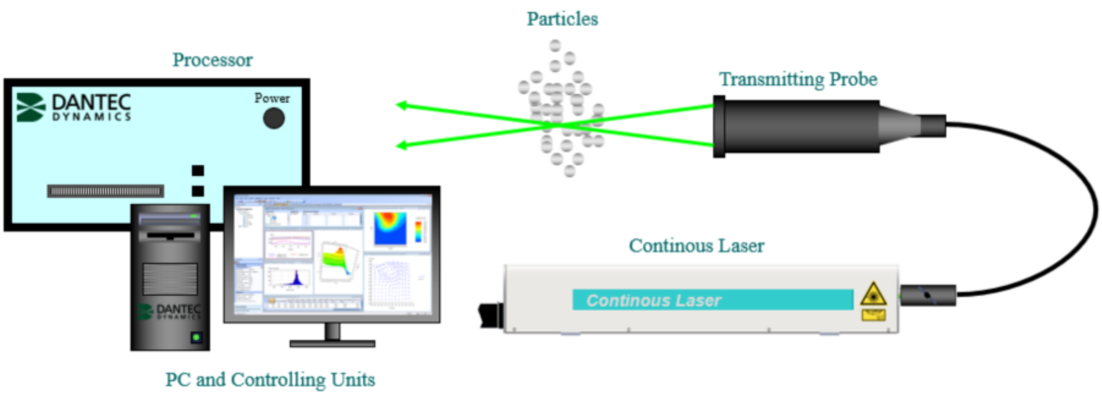


FIGURE 2.5: LDA configuration [3]

Measurement probe includes transmitting and receiving optics as well. When a seeding particles moves around the intersection points of transmitting laser beams, received light intensity changes due to Doppler shift (Figure 2.6). After a series of signal processing algorithms applied, velocity components of the corresponding points can be recovered [25].

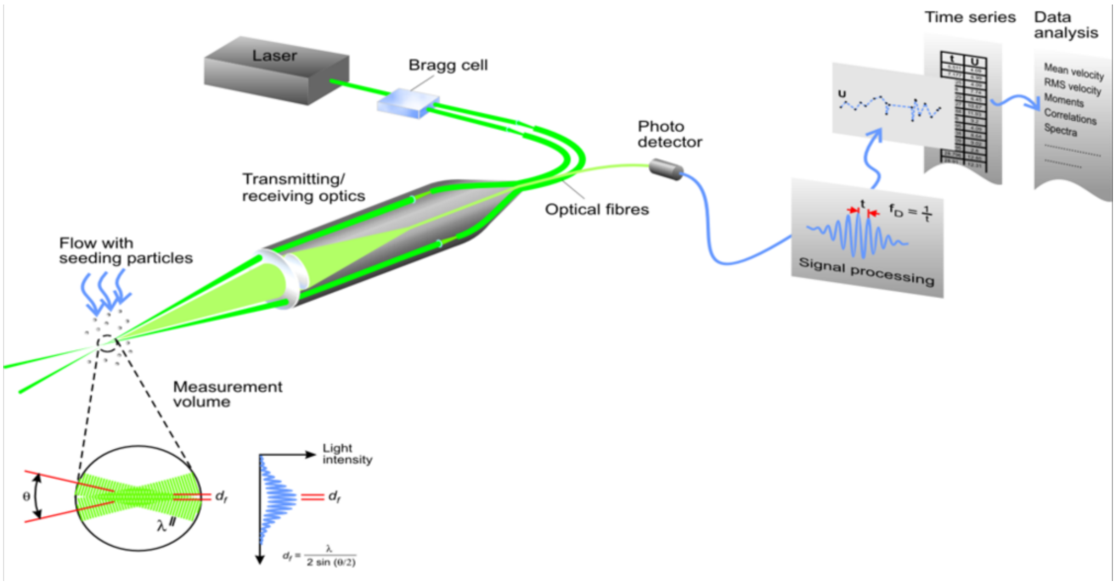


FIGURE 2.6: LDA measurement principles[3]

As distinct from PIV, which is a whole field measurement technique, LDA transmitting probe is targeted to a single point in gas or fluid flow (Figure 2.5). In addition to turbulence, up to three component velocity of a single point can be measured with LDA. Deen applied both single camera PIV with LDA gas-liquid flow in a bubble column and stated the advantages and disadvantages of these techniques. PIV can measure whole plane without distorting the flow but temporal resolution in PIV is very low, e.g. 15 Hz for digital PIV. On the other hand, temporal resolution in LDA is very high e.g. 1kHz, but LDA can measure just single point, so velocities of different phases cannot be measured [26].

### 2.2.3 Phase Doppler Anemometry (PDA)

Phase Doppler Anemometry is an extension of Laser Doppler Anemometry. PDA transmitting probe is also targeted to a single point but different from LDA, three receiving probes are separated from transmitting probe and they measure the scattered angle of the particle (Figure 2.7).

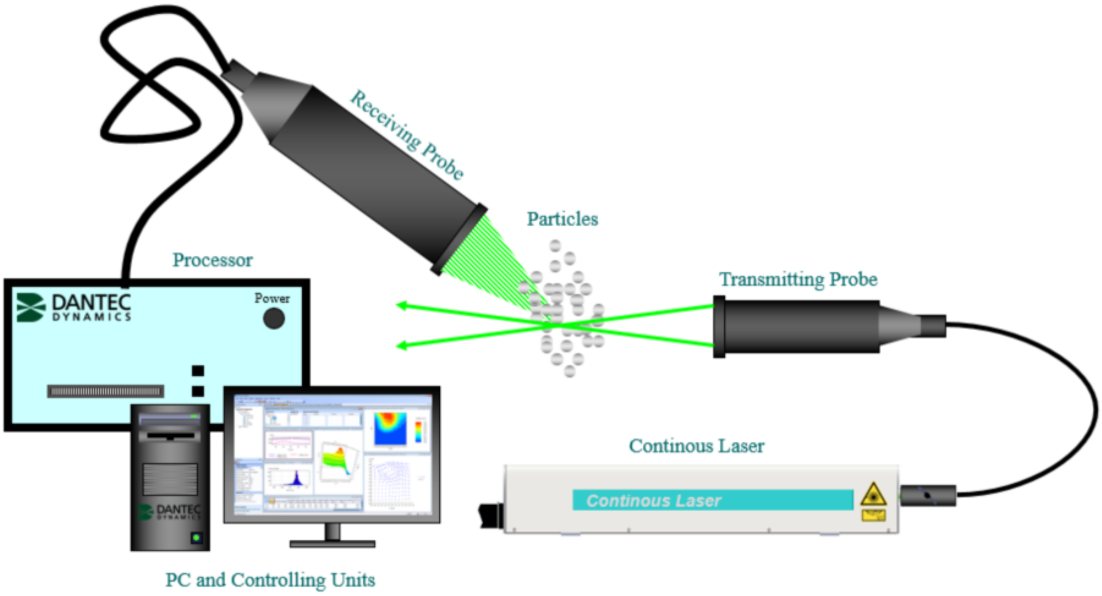


FIGURE 2.7: PDA configuration[3]

Spherical particles such as droplets, bubbles and solid seeding particles, reflects waves which are proportional to their velocities in return to two laser beam coming from transmitting probe. Receiving probes sense these waves with different phases and this phase shift is also proportional to the diameters of spherical particles [27].

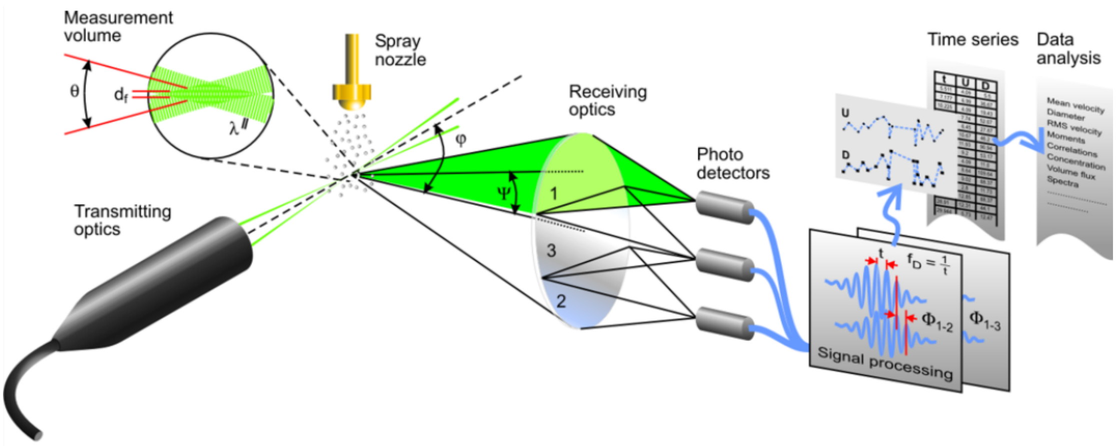


FIGURE 2.8: PDA measurement principle [3]

Measurement principles of PDA also provide measurements related to sizes and shapes of particles. Consequently, PDA is often preferred in research studies such as analysis of bubbly multiphase flows, spray characterization, liquid atomization [28–30].

### 2.2.4 Interferometric Particle Imaging (IPI)

Interferometric Particle Imaging (IPI) also known as Interferometric Mie Imaging (IMI) is based on utilizing the focused and defocused images of spherical particles [31]. Obtaining focused and defocused images can be done via a single camera with moving platform or dual camera with adjusted positions. 'Interferometric' term explains that the reflection and refractions of shiny points are interfered to generate a fringe pattern in overlapping region (Figure 2.9).

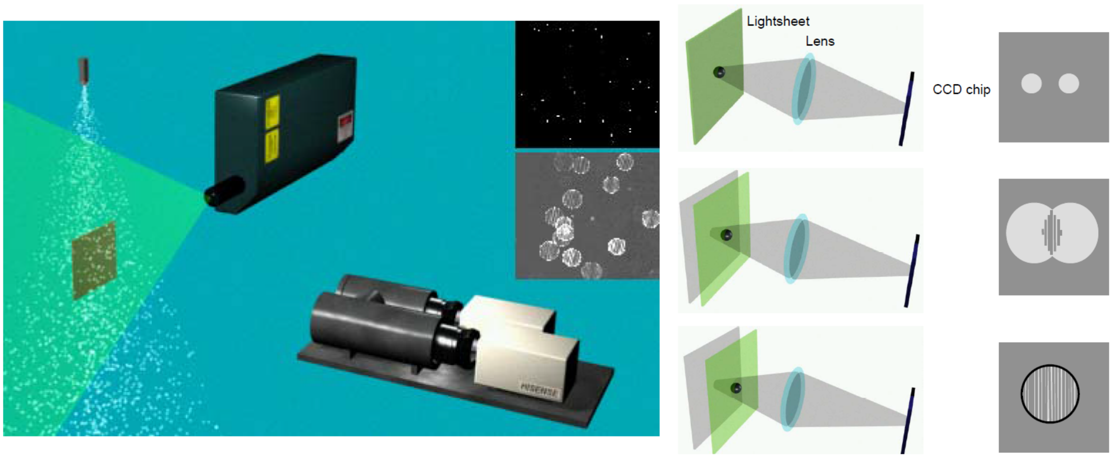


FIGURE 2.9: IPI configuration and fringe pattern generation in overlapping area [3]

Mie theory [32] explains that obtained fringe patterns corresponds to the far field scattering. Number of fringes in overlapping region increases with the larger diameter of shiny points. Aperture angle is another important parameter for IMI. Angle between laser sheet and high speed camera's focal axis should be 90 degree for parallel polarization and 68 degree for perpendicular polarization [33].

In several research studies [34–36] Interferometric Particle (Mie) Imaging is implemented to measure the sizes, velocities and positions of transparent spherical particles in gas or fluid flows.

### 2.2.5 Particle Shadow Sizing (PSS)

Particle Shadow Sizing (PSS) also known as Particle Shadow Velocimetry (PSV) is a whole field optical imaging technique like PIV. Differently, light source is located on the optical axis of high speed camera and particle shadows are monitored (Figure 2.10).

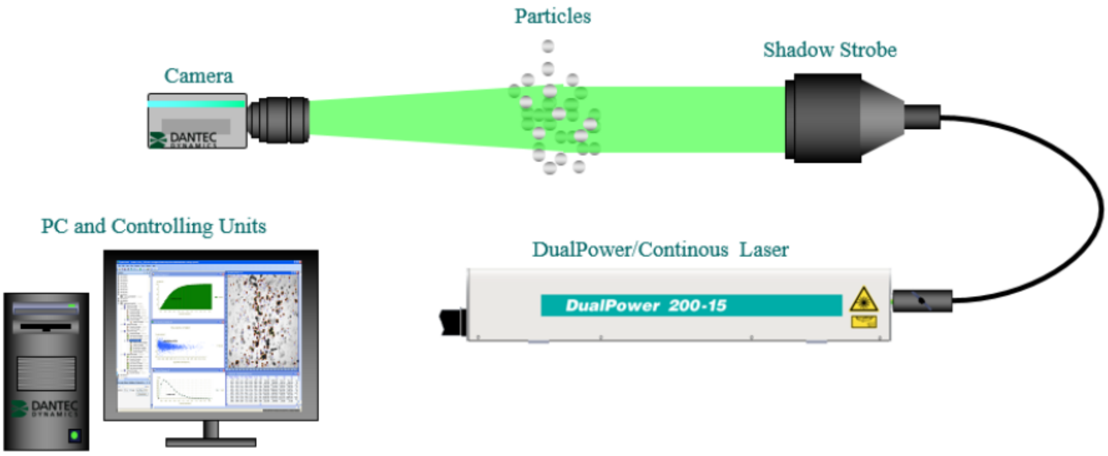


FIGURE 2.10: PSS configuration [3]

Particles, droplets, bubbles and small solid structures such as powder could be visualized in the scope of micron scale with appropriate magnification levels [37]. High speed laser sources, long distance microscopes and high speed CCD and CMOS cameras enable not only recovering the two component velocity fields but also size and shape information thanks to advanced image acquisition and processing methods [38]. Observed particles do not need to be shiny or spherical as in the case of LDA, PDA and IPI to recover their shape information, since PSS measurement principle does not depend on the scattering light from the surface of the particle. Instead, direct in-line illumination is employed to visualize the particle shadows on bright background [39].

Since observed particle speed may be very high due to the motion of the gas or fluid flow, non-coherent high power LEDs or single/dual high power lasers are employed as illumination sources. Recently, non-coherent power LED illumination based high magnified PSV imaging architectures are exploited to investigate micro bubbles and micro structures, so this procedure is also called $\mu$PSV [40, 41].

Within the scope of this thesis, PSS imaging system architecture with different illumination configurations is designed to visualize multiphase flow and analyze hydrodynamic cavitation bubbles and droplets.

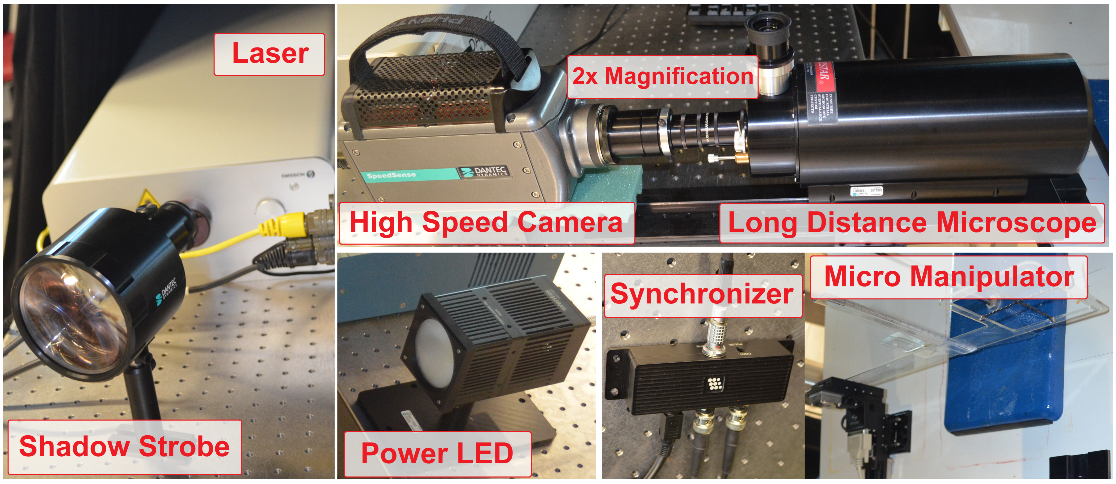


FIGURE 2.11: Particle Shadow Sizing components

Visualization system includes Dantec Dynamics Dual Power TR laser, Dantec Dynamics Shadow Strobe, alternatively Power LED, Phantom v9.1 high speed camera, Questar QM 100 long distance microscope, synchronization component and Sutter Instruments MP-285 micromanipulator (Figure 2.11).

Dual Power TR Laser has up to 30 mJ energy and up to 10 kHz repetition rate, which allows to illuminate high speed micro particles. Targeting the laser directly to the camera optical axis is very hazardous since laser is a focused form of scattered light beams. Thus, Shadow Probe is needed to scatter laser beam and create a homogeneous light bundle. Shadow Strobe carries focused laser beam through the 2 meter liquid light guide cable and scatter the beam with several mirrors and lenses. Spotlight adjustment behind the strobe (Figure 2.13) can be manipulated linearly to change spotlight size from few mm$^2$ to 1000 mm$^2$ and working distance from 10 cm to 1 m [42]. By this adjustment Shadow Strobe can be used in "telecentric" or "microscope" mode, as we prefer telecentric mode because of its easy-to-use structure.

In our former experiments, we employed Phantom v310 CMOS camera with Infinity Model K2 DistaMax Long Distance Microscope, that provides 10.000 fps 8

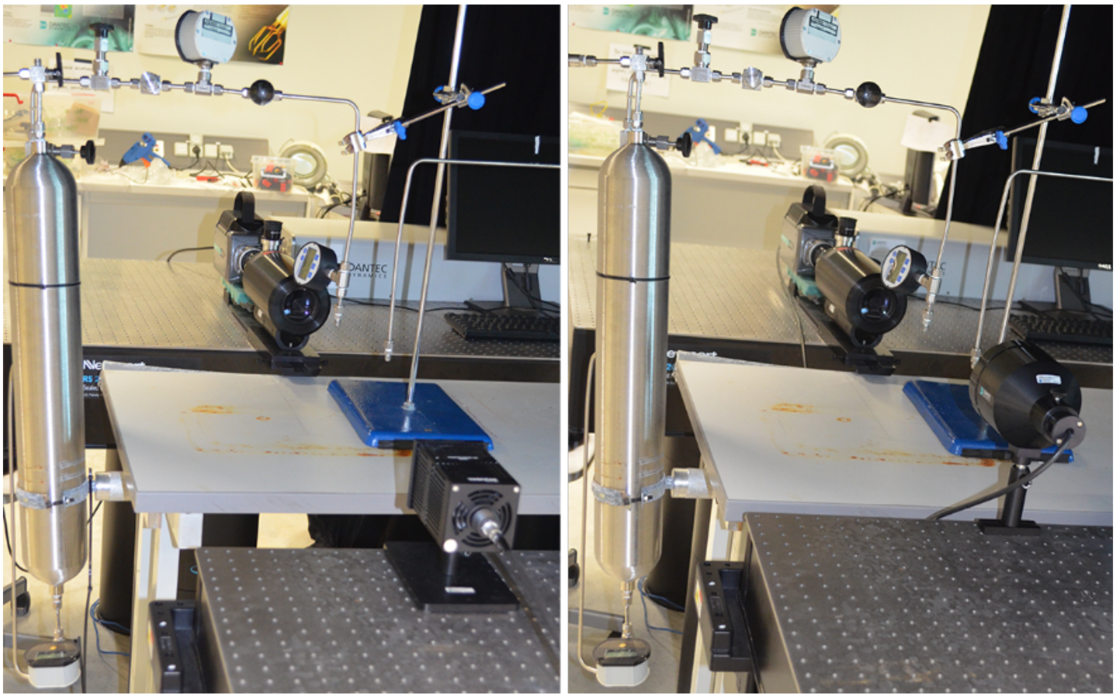

FIGURE 2.12: PSS configuration with Power LED (left) and Shadow Strobe (right)

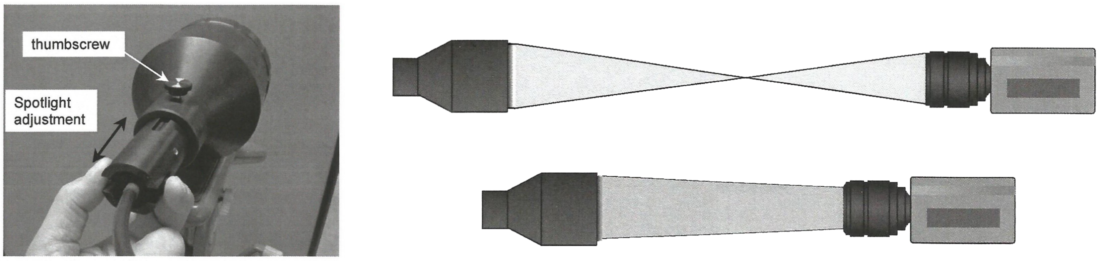


FIGURE 2.13: Left: Spotlight adjustment Right: Microscope (up) and Telecentric(bottom) Modes

bit images with 600×800 resolution. Covered area corresponds to $4578\mu\times6104\mu$. 2 pulsed 198 LED array was used as illumination sources.

In new visualization system, Phantom v9.1 high speed camera provides up to 10 kHz frame rate and 1600×1200 pixel resolution. To increase the magnification 2× lens and Questar QM 100 Long-Distance Microscope are equipped with the camera. Questar QM 100 supplies 16× magnification in 15 cm - 35 cm working distance. Final 32× magnification covers the $857\mu\times610\mu$ area. Synchronization component is assigned in timings of single and double frame modes of power LED or laser source. It also adjusts the shutter time of camera to capture the stage.

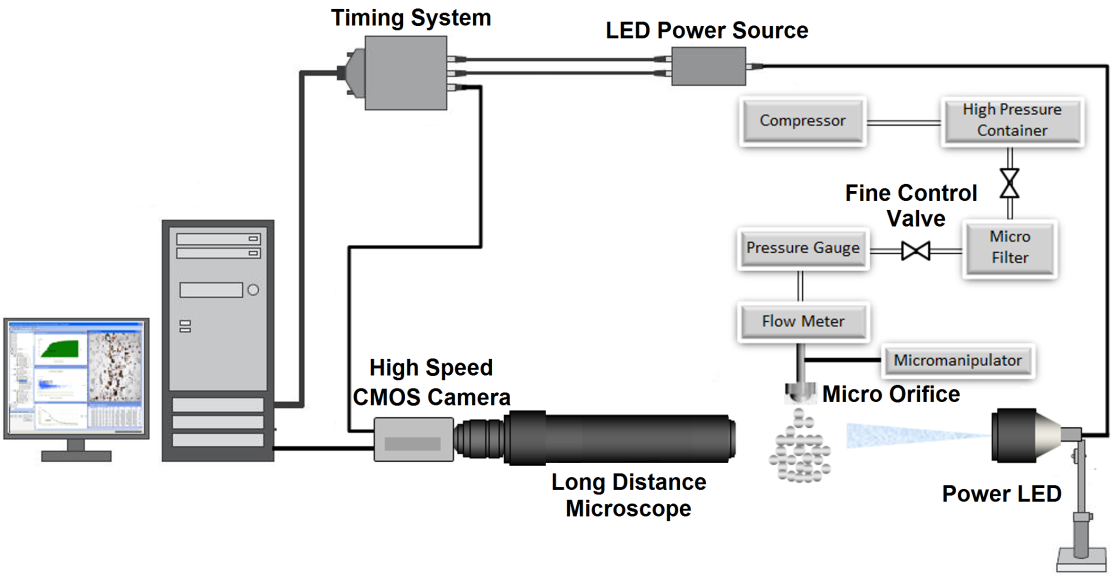


FIGURE 2.14: Hydrodynamic cavitation visualization system

Before acquiring shadow images, the most challenging issue is to focus the system on the desired location. Since we employ very high magnification levels, it is not easy to find the focus point exactly for a few trials. To ease the focusing period, MP-285 micromanipulator, which has a few submicron sensitivity, is utilized to find focus points accurately. Finally, a complete particle shadow sizing based hydrodynamic cavitation visualization system architecture is obtained as in Figure 2.14.

## 2.3 Segmentation and Visual Tracking Methods

**Image segmentation** is one of the most fundamental approaches in computer vision which enables and contributes various other vision methodologies as well such as recognition and tracking. Typically image segmentation methods start with image preprocessing steps to eliminate noises and proceed with specific tasks that put forward desired region(s) of the image. Segmentation can be based on searching for a predefined single object or multiple regions that behave in the same manner. Starting from the earliest techniques to up-to-date algorithms, segmentation methods can be investigated in 6 groups.

1. ***Thresholding methods*** as initially Otsu [43] defined, convert multilevel grayscale images into binary images according to specific threshold level, which can be categorized into three such as global thresholding, local thresholding and dynamic thresholding based on the selection of threshold level T.

2. ***Edge detection based segmentation*** necessitates to find the edges between the regions. In computer vision, edges are defined as the pixels which have sudden transition change in intensity. Edge detection is one of the most primitive and fundamental segmentation method. Kittler and Illingworth [44] proposed a gray histogram techniques which was based on modifications to Otsu's [43] threshold method. Instead of gray histogram, Canny presented a novel computational approach to edge detection which was a gradient based method [45].

3. ***Region based segmentation methods*** rely on connected pixel groups in whole image and segmented into sub regions. Chang and Xiaobo [46] proposed a method which does not require any parameter tuning or a priori knowledge. The method mainly includes region growing, region splitting and merging techniques.

4. ***Partial Differential Equation (PDE) based segmentation methods*** propose to solve the partial differential equation model by a numerical scheme to segment the image. Snakes (active contours) [47], Level set model [48], Mumford Shah [49] model and C-V model [50] are powerful examples of PDE based image segmentation methods.

5. ***Artificial Neural Network (ANN) based segmentation methods*** involve in conversion of segmentation problem into Neural Network problem, where every pixel is mapped as neurons and segmentation is considered as an energy minimization problem [51].

6. ***Clustering based segmentation methods*** are unsupervised methodologies which necessitate to define a set of categories as clusters by classifying the pixels. Hard clustering [52] and Fuzzy clustering [53] are two different ways of clustering based segmentation.

**Visual object tracking** is very challenging problem which aims to locate moving object(s) throughout the sequential video frames. Tracking process includes detection tracking and analysis of predefined interested objects, which enables this technique to be used in various applications such as motion-based recognition, automated surveillance systems human-machine interactions, vision based vehicle navigation, traffic monitoring and video indexing [54].

Simply, visual object tracking can be considered as an estimation problem to predict the target object(s) in upcoming video frames, which makes representation of target object very crucial in visual tracking. Within this context, tracking methods can be categorized according to types of target representation as point tracking, kernel tracking and silhouette tracking.

1. ***Point tracking*** requires to represent the target object by distinct feature points and these points may necessitate to be detected again during the consecutive video frames. Point tracking can be investigated in two groups according to representation of modeling as deterministic or probabilistic:

    - Modifying Greedy Exchange (MGE) tracker [55] and Greedy Optimal Assignment (GOA) [56] tracker are examples of deterministic point tracking methods, which mainly target to handle occlusion and wrong detection problems.

    - Kalman filter based tracker [57], Joint Probabilistic Data Association Filter (JPDAF) tracker [58] and Probabilistic Multi-Hypothesis Tracking (PMHT) [59] are instances of statistical point tracking models, which include probabilistic approaches to track single or multiple targets.

2. ***Kernel tracking*** requires the object shape and appearance, so tracking can be performed by computing the motion of the related kernel representing the shape of the target object. Rotation, translation and affine transformations are fundamentals of computed motions.

- Mean-shift [60], Kanade-Lucas-Tomasi [61] and Layering tracking methods [62] are based on a template or distribution based appearance models which can be obtained by several distinct features of interested target(s).
- Eigen tracking [63] and Support Vector Machine (SVM) tracker [64] require multi-view appearance models, which can be acquired by multiple cameras or a single moving camera during the motion.

3. ***Silhouette tracking*** is based on the estimation of the target object region in consecutive frames and tracker is focused on the object region such as area, orientation, form of edge maps, appearance density. Shape matching or contour evolution is applied to track the silhouettes.

    - State space models [65], Variational methods [66] and Heuristic methods [67] are silhouette tracking methods which investigate the change of outer boundary of target(s) during the video frames.
    - Hausdorff [68], Hough transform [69] and Histogram [70] models track the silhouette(s) of the interested object(s) by shape matching.

A common characteristic of these methods is representing the target in a specific form and they differ from each other within the concept of how to do it. However, various tracking applications show that target object's shape may be deformed, pose could be varied or environmental factors such as varying illumination, occlusions and camera motion can disturb the target representation, which created a need for online learning techniques that capable of updating these changes during the video frames [71].

Online learning based tracking algorithms can be investigated in two groups as generative and discriminative methods. In generative method, updating the appearance of the target object is proposed to achieve robust tracking [72–74], whereas in discriminative methods (as known as *tracking by detection*) sets of features to identify both object and background are utilized to train a classifier to learn the changes and segment the interested target(s) during consecutive video frames [75–77].

### 2.3.1 Bubble/Droplet Tracking

In literature, there exist several micron sized particles, bubbles and droplets tracking algorithms applied in various visualization systems. Bubble/droplet tracking techniques in literature can be investigated in 3 groups such as shape/contour modeling based tracking, label-free tracking and matching based tracking.

Cheng and Burkhardt develop a bubble contour tracking system by assuming their shape as circular. Positions of the bubbles are recovered by radial scans and the method is able to handle with overlapping issues [78]. Tomiyama et al. demonstrate 3D bubble tracking method in vertical pipe, which mainly depends on shape models and proper boundary conditions [79]. Okawa et al also utilizes the bubble shape function to track the rising bubbles in a pipe. Additionally phase coupling models are proposed due to the requirement of that conservation of the equations must be solved simultaneously [80].

Basu presents a time-resolve analysis of droplets via droplet morphology and velocimetry (DMV), which includes several preprocessing steps to distinguish foreground from background and correlation steps. Proposed label-free technique supplies several motion and structural information related to micron scale droplets [81]. Jüngst et al also propose a label free tracking for long term observation of lipid droplets throughout the cells by Coherent Anti-Stokes Raman Scattering (CARS) microscopy [82].

Qian et al. propose matching and tracking method, which utilizes genetic algorithm. Method can distinguish similar sized and shaped bubble in even kinetic occlusion cases as well [83]. Xue et al. present a tracking and 3D reconstruction method in stereo vision by matching correspondences of bubble distinct features from different half views [84].

# Chapter 3

# Visual Analysis of Cavitation Flow

Visualization of micro scale cavitation bubbles using the Particle Shadow Sizing (PSS) imaging technique and processing acquired images using appropriate algorithms are very crucial visual tasks. Extracting visual information from microscopic images and estimating important parameters of the underlying physical phenomenon have been the focus of several research studies in the past [85–87].

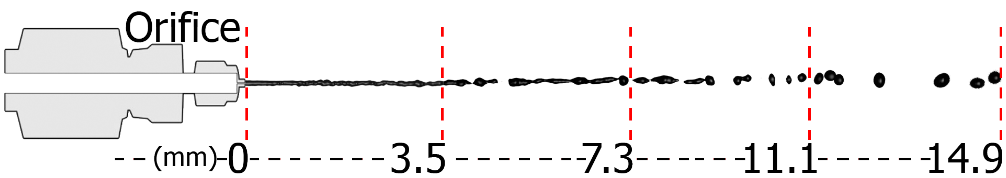


FIGURE 3.1: Bubbly flow at different inlet pressures was recorded in 4 segments

Cavitating flows emerging from the short microchannel were recorded at different inlet pressures from 10 bars to 120 bars while outlet pressure was 1 atm. Due to narrow depth of field of visualization system, only a 4.5 mm x 6.1 mm local area could become possible to monitor with proposed visualization system. Starting from the beginning of the orifice, systems field of view is moved toward to end of the flow with around 3.5 mm distances to investigate the entire of bubbly flow motion (Figure 3.1).

A virtual cone starting from the orifice of the bubbly flow generator along with the flow was formed during the cavitation process. Angle of the virtual cone have to be determined to control the orifice position of bubbly flow generator towards the target and estimate the covered area in various deterioration operations.

Ascending pressure level naturally leads to an increase in the speed of multiphase bubbly flow, complicating to visualize the entire of the flow motion and detect bubbles individually. Visualization of hydrodynamic cavitation was implemented with different illumination sources.

- **Experiment 1:** Commonly used dual LEDs were utilized as illumination sources. Since illumination power is lower due to LEDs, scattered bubbles around main jet flow could not be caught, resulting that first segments of the flow until medium inlet pressure (Pi $\leq$ 50 bars) were observed as solid pipeline (Figure 3.2). With ascending inlet pressures after 50 bars, virtual cone angle formed in segment 1 got widened. Additionally, until the medium inlet pressure, ***droplets*** could be visualized individually in $3^{rd}$ and $4^{th}$ segments, which became impossible with higher inlet pressures due to obvious ascending flow motion.

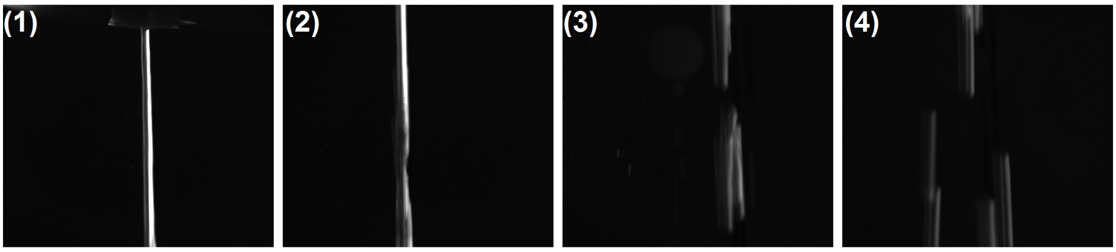


FIGURE 3.2: *Exp 1*: Visualization of the flow in 4 segments (Pi = 50 bars)

- **Experiment 2:** Dual LEDs were replaced by a single power LED to enhance the illumination. Scattered bubbles around main jet flow in first segments became visible with new illumination source (Figure 3.3). ***Bubbles*** could be easily separated from the main multiphase jet flow in $3^{rd}$ segment with the pressure level below 30 bars and in $4^{th}$ segment with 40 to 50 bars, whereas it was impossible to detect bubbles individually with the pressure level above

60 bars since multiphase bubbly flow jet abode its partial solidarity due to high pressure.

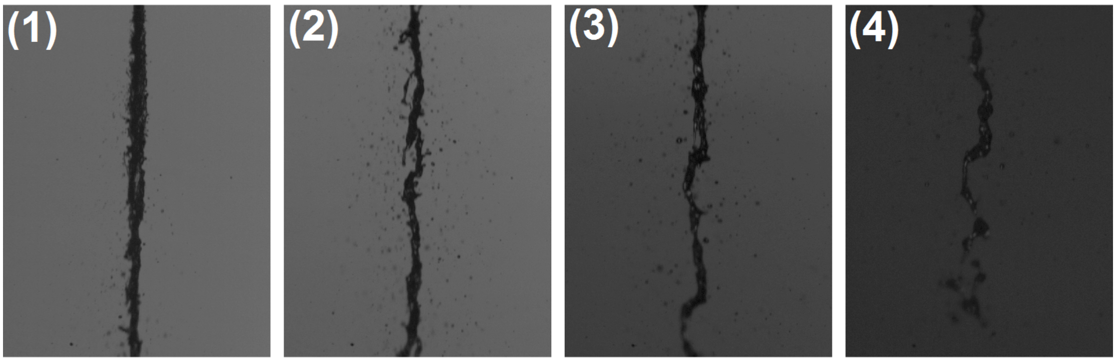


FIGURE 3.3: *Exp 2*: Visualization of the flow in 4 segments (Pi = 50 bars)

In both experiments, acquired images were not appropriate enough to calculate the virtual cone angle without any processing steps, so several image preprocessing techniques are applied to each frame throughout the recorded video to enhance the image quality.

## 3.1 Cone Angle Estimation

During the hydrodynamic cavity flow visualization, main multiphase flow jet and scattered bubbles around the main jet constitute a rough virtual cone in each frame. In order to employ the hydrodynamic cavitation in various biomedical applications such as kidney stone erosion, one must position the orifice of bubbly flow generator towards the target specimen (e.g. kidney stone) accurately and be aware of the manipulated area of multiphase bubbly flow. Hence, estimation method of virtually obtained cone angle is proposed based on the processing of each frames in recorded bubbly flow video. Since estimation of the cone angle from a single frame could be unreliable, superimposition of preprocessed binary frames is applied to construct 3D structure, which is then modeled as Gaussian and utilized to take cross-section for detection of bubbly flow edges. Finally, best lines are fitted to extracted edge points and Kalman filter [88, 89] is employed for robust estimation of cone angle.

### 3.1.1 Image Preprocessing Methods

In recorded images, the main multiphase flow jet and bubbles around it may not be distinguished from the background easily due to shadows, noises and undesired particles. In order to segment the pertinent parts of the bubbly flow, several image preprocessing steps must be applied to acquired data. These steps involves contrast stretching, morphological operations, thresholding and connected component analysis. Since the quality of illumination source was different in Experiment 1 and 2, necessity and the order of the mentioned steps may vary depending upon the needs of visualization system. Appropriate combination of image preprocessing methods were employed to pick out droplets individually in Segment 3 of Experiment 1, main jet flow and scattered bubbles around it in Segment 1 of Experiment 2 from the background.

#### 3.1.1.1 Contrast Stretching

Illumination is very crucial factor to obtain well distinguishable images of particles/flow in several micro imaging techniques such as Particle Shadow Sizing. Due to narrow field of view, contrast of the acquired images may not be sufficient enough. In such cases, before starting to implement any visual algorithm, contrast stretching method is usually employed which enables to enhance the grayscale level (Figure 3.4 , 3.6).

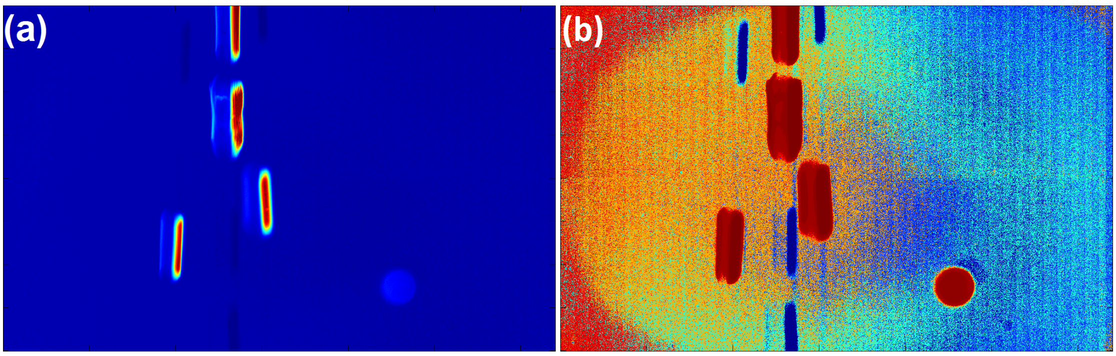


FIGURE 3.4: *Exp.1* (a) Unprocessed original image (b) Contrast adjusted image

With a convenient form of contrast transformation function, below a certain reference point levels are darkened and above the same point levels are brightened in original image to achieve higher contrast [90]. Contrast stretching is a specialized form of histogram equalization technique which distributes the grayscale levels uniformly (Figure 3.5 , 3.7) to sharpen the image and upgrade the discernibility.

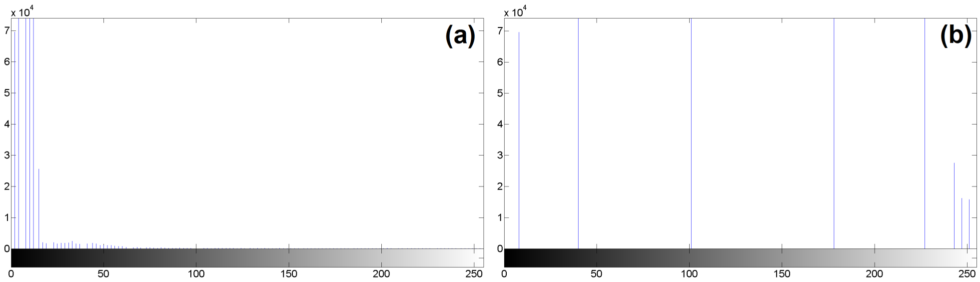


FIGURE 3.5: *Exp.1* (a) Histogram of original image (b) Histogram of contrast adjusted image

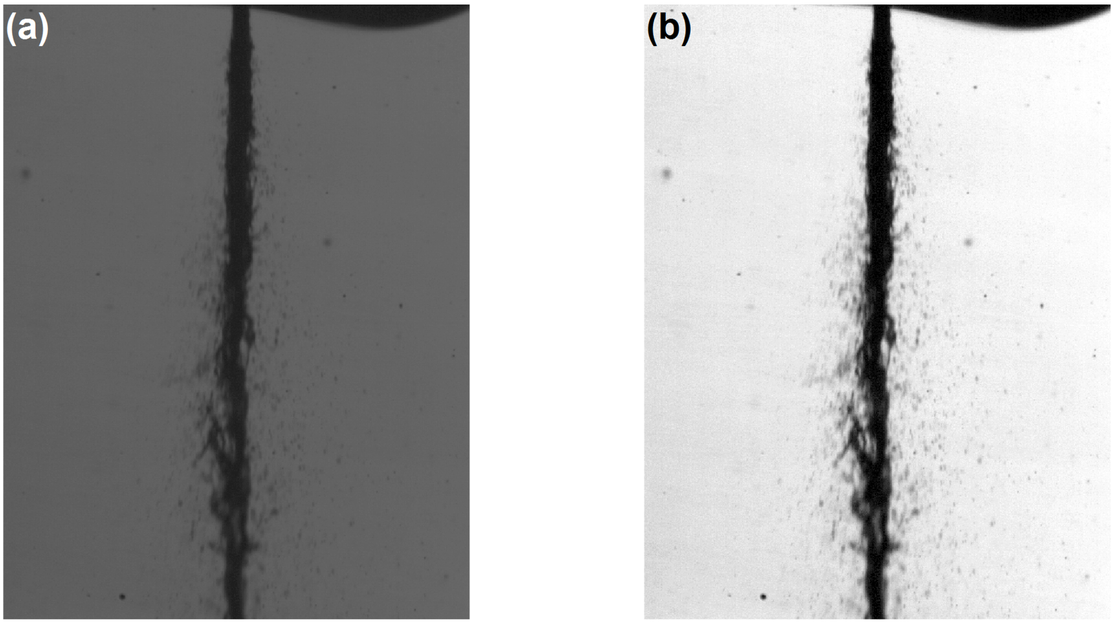


FIGURE 3.6: *Exp.2* (a) Unprocessed original image (b) Contrast adjusted image

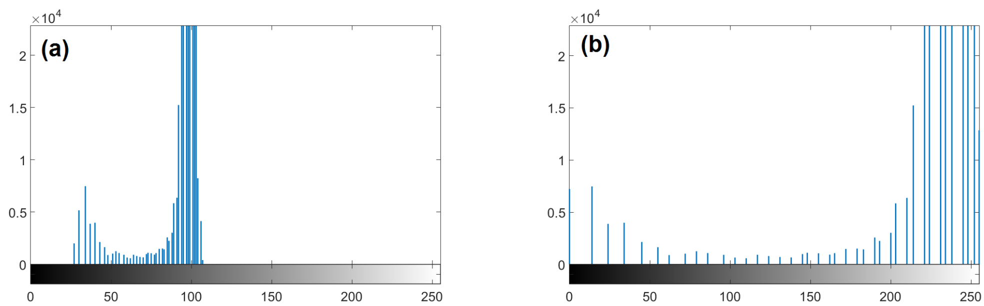


FIGURE 3.7: *Exp.2* (a) Histogram of original image (b) Histogram of contrast adjusted image

#### 3.1.1.2 Morphological Operations

Morphological operations are nonlinear transformations of binary images which alter the shape or structure of an object in the image [90–92]. Two main morphological operators, erosion and dilation are originated from set theory in Mathematics [92]. Erosion of $A$ by $B$ ($A \ominus B$) and dilation of $A$ by $B$ ($A \oplus B$) are defined respectively as follows

$$A \ominus B = \{z|(B)_z \subseteq A\} \tag{3.1}$$

$$A \oplus B = \{z|(\hat{B})_z \cap A \neq \emptyset\} \tag{3.2}$$

The combinations of these fundamental operators with different orders also define new operators such as closing and opening. Closing is the erosion of the dilation and opening is the dilation of the erosion. Opening operator can clean the small objects from the foreground, whereas closing operator can clean the small gaps in foreground [90]. The opening of set $A$ by structuring element $B$ ($A \circ B$) and the closing of set $A$ by structuring element $B$ ($A \bullet B$) are defined respectively as follows

$$A \circ B = (A \ominus B) \oplus B \tag{3.3}$$

$$A \bullet B = (A \oplus B) \ominus B \tag{3.4}$$

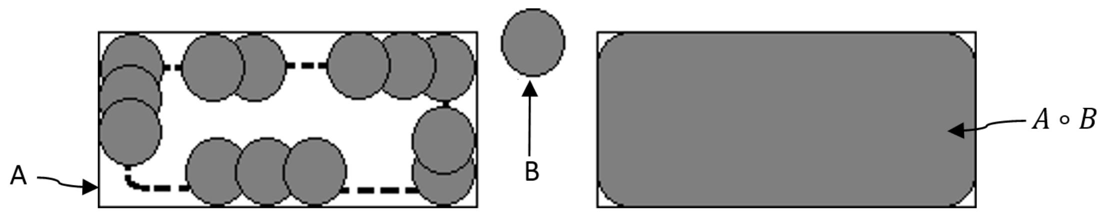


FIGURE 3.8: Representation of opening A by structuring element B

Gonzalez and Wood [90] depict the opening operator as rolling the structuring element along through the inner boundary of the object (Figure 3.8), which enhance the images as a tool of noise removal and gaps filling. Additionally, a wisely-determined structuring element of opening operator can bring out the preferred segments of the image and eliminate the rest. In this sense, during Experiment 1, 3×13 vertical rectangle structuring element was chosen due the shapes of droplets in segment 3, enabling droplet candidate regions distinguishable from background easily (Figure 3.9).

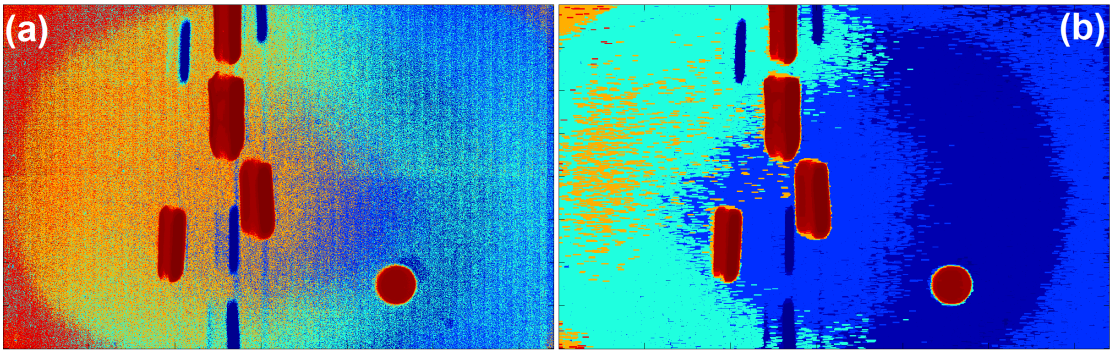


FIGURE 3.9: *Exp.1* (a) Contrast adjusted image (b) Opening operation

#### 3.1.1.3 Thresholding

Since morphological operations disambiguated the droplets in Experiment 1 and contrast adjusted images make it feasible to distinguish hybrid bubble and main multiphase bubbly flow structure from the background in Experiment 2, segmentation of droplets and hybrid structure were done by thresholding with an appropriate level (Figure 3.10 , 3.11). Optimum threshold level was designated by Otsu's clustering-based method [43], which converts grayscale image to binary image based on two clusters as foreground and background.

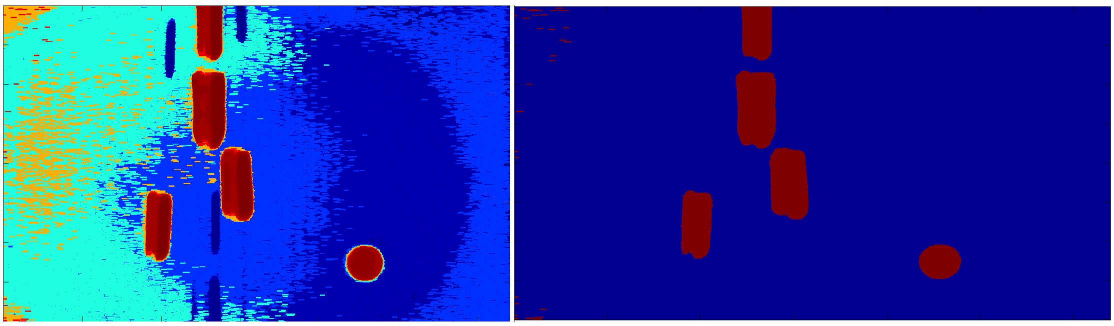

FIGURE 3.10: *Exp.1* (a) Opened image (b) Thresholding the opened image

Thresholding based segmentation may sometimes lead to introduce some disturbances, noises and bring about some gaps or missing data in the binary image,

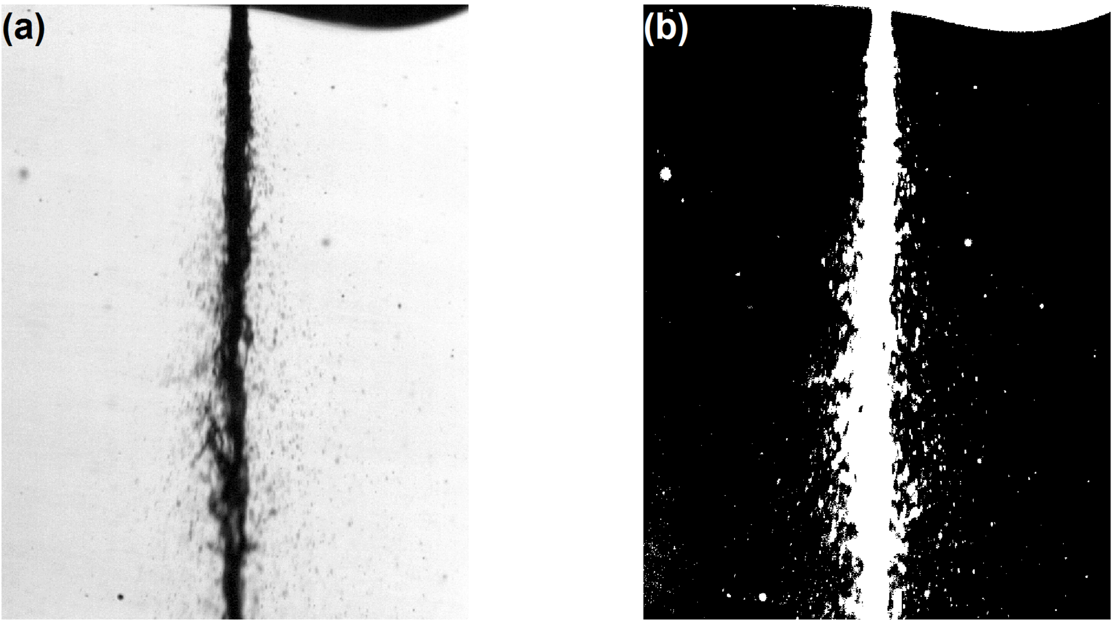


FIGURE 3.11: *Exp.2* (a) Contrast adjusted image (b) Thresholding the contrast adjusted image

which creates need for structural improvements and enhancements. Morphological operations are employed to purify the binary image from noises and fill the blank holes that are caused by thresholding (Figure 3.12). Structuring element B is determined as a disk with small enough radius, enabling to clean adventitiously generated noise particle and filling the unintentionally comprised holes.

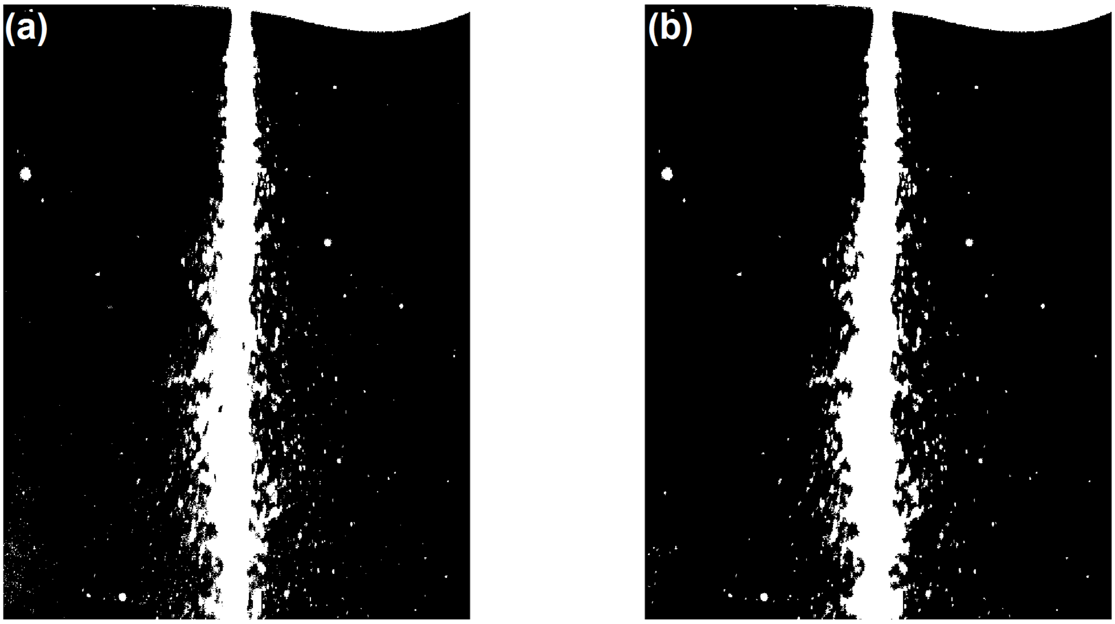


FIGURE 3.12: *Exp.2* (a) Thresholded image (b) Opening of thresholded image

#### 3.1.1.4 Connected Component Analysis

Nonlinear filtering based preprocessing steps may not always end up with perfect noise free results. To bring out the pertinent regions and eliminate the rest, region based Connected Component Analysis (CCA) can be employed. CCA looks for the relationships between pixels and divides them into different groups. In each group, pixels are located in the neighborhood of each other and labeled with pre-specified properties.

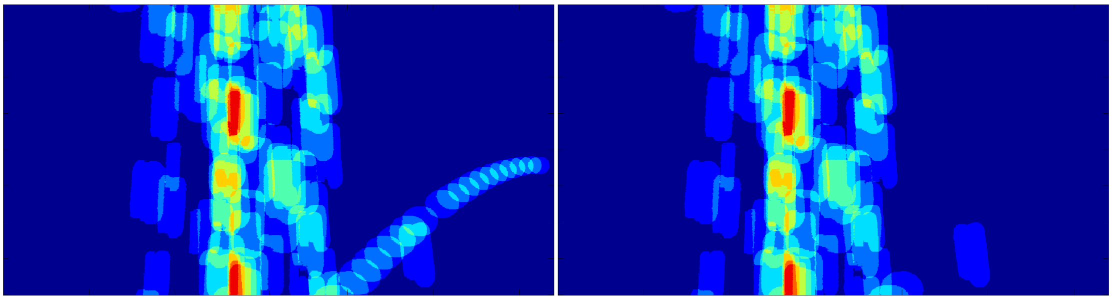

FIGURE 3.13: *Exp.1* (a) Existence of circular noise (b) Removal of circular noise

In Experiment 1, all labeled regions in pre-processed binary images were candidates of droplets. With prior observed knowledge, droplets had some considerable amount of pixel wise areas between 5000 and 15000. Thus, less than a certain pixel wise area, regions could be seen as noise and excluded.

Apart from less amount of pixel wise area, it is observed that there were some circular regions which did not flow like other droplets (Figure 3.13(a)). After superimposition of several images, which will be presented in the following section, circular noise trajectory could be easily distinguished from usual droplets' trajectories. The shapes of droplets were utilized in this case to get rid of circular noise. In geometry, eccentricity of a shape represents how it is close to a pure circle. This number is between 0 - 1 and it is close to 1 if the shape is pure circle. Obviously eccentricities of droplets and circular noises were far from each other, which made it possible to increase the droplet detection accuracy by eliminating the non-droplet regions (Figure 3.13(b)).

### 3.1.2 3D Gaussian Modeling

After some preprocessing steps explained in Section 3.1.1 are applied to each frames, acquired binary images are considered as instant positions of the droplets in Experiment 1, the bubbles and main bubbly flow jet in Experiment 2. In place of calculating the cone angle from each single frames, instant positions are accumulated and each binary frames are superimposed to gather information about the motion during the whole process of bubbly flow.

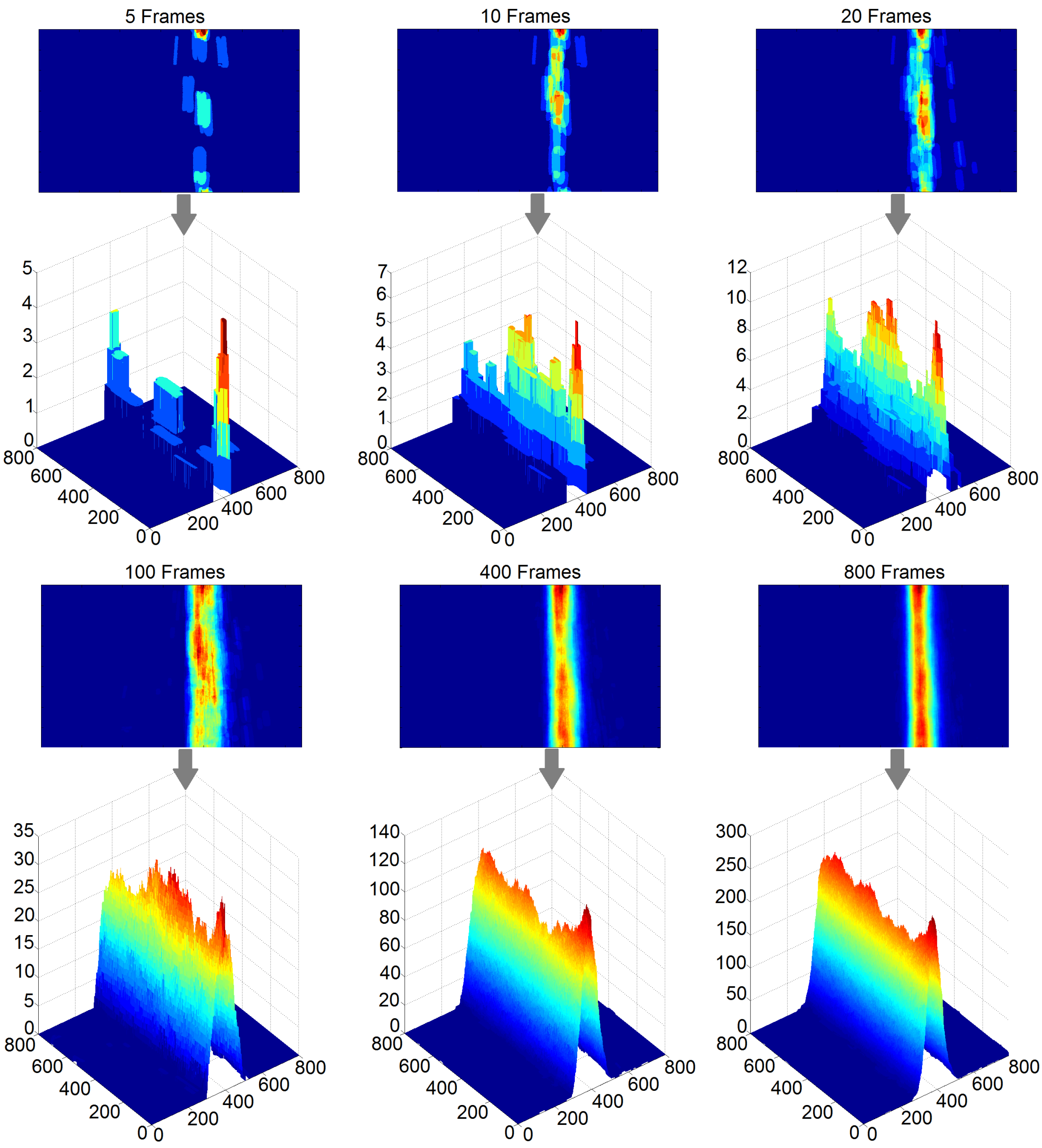


FIGURE 3.14: *Exp.1* Superimposition of frames

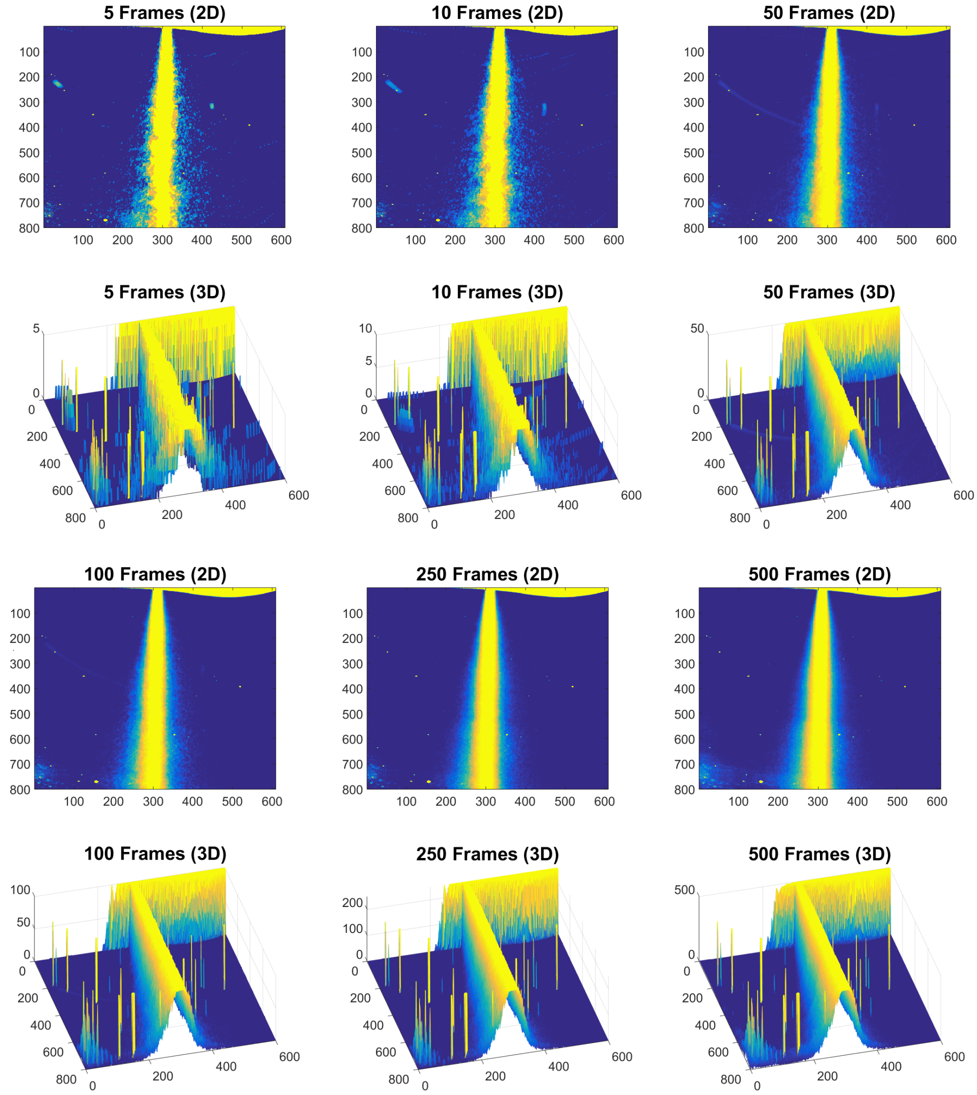


FIGURE 3.15: *Exp.2* Superimposition of frames

As shown in Figure 3.14 and 3.15, red peaks and lighter segments of the image represent the places where flow occurs most frequently. 2D representation of superimposed structure encourages to construct its 3D form to reach detailed information about the flow. Indeed 3D structure of superimposed bubbly flow indicated Gaussian distribution.

Superimposition procedure is applied in Experiment 2 with various inlet pressures from 10 bars to 120 bars (Figure 3.16), which showed that ascending pressure level results in obtaining wider Gaussian distribution.

Since droplets could be visualized individually in $3^{rd}$ segments until the medium

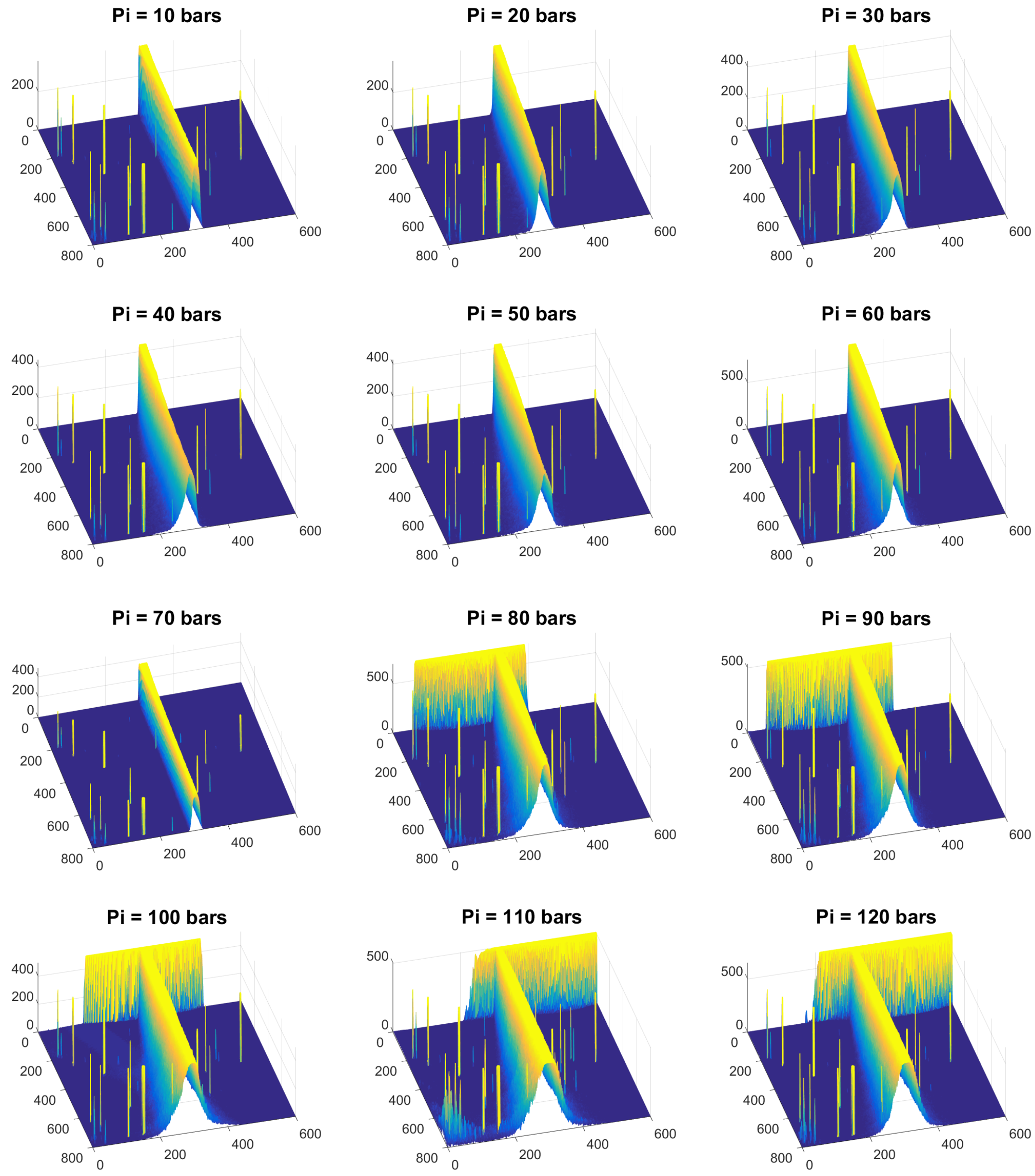


FIGURE 3.16: *Exp.2* Obtained 3D Gaussian structure for each inlet pressures 10-120 bars

inlet pressure (Pi $\leq$ 50 bars) in Experiment 2, superimposition was not applied to images belonging to inlet pressure higher than medium pressure. Instead, each frame was assumed to be superimposed by several undistinguished droplets, accordingly 3D representation of each acquired (and preprocessed) frames were indeed Gaussian distribution instinctively (Figure 3.17).

In order to investigate the influence of ascending pressure level and determine a convenient interval for cross-section, second order Gaussian polynomial function

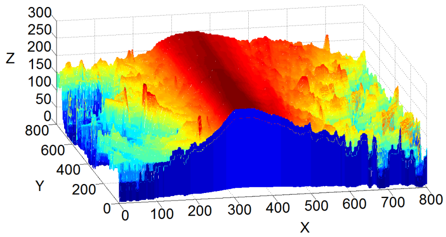


FIGURE 3.17: *Exp.1* 3D structure at higher inlet pressure levels (Pi > 50 bars)

is fitted to data belongs to the cross section of formed 3D structure along Z axis (perpendicular to image plane) by nonlinear least squares method and trust-region algorithm (Figure 3.18). Goodness of fit (Fit R-Square and RMSE) and Gaussian functions with its parameters ($\sigma$ and $\mu$) are demonstrated in Table 3.1 and Table 3.2 respectively for each inlet pressures from 10 bars to 120 bars.

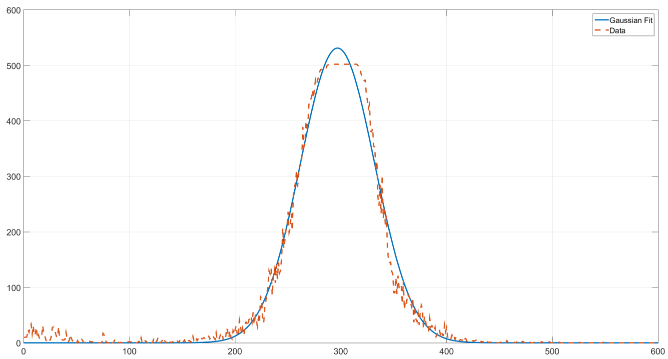


FIGURE 3.18: *Exp.2* Gaussian function fit (Pi=110 bars)

| **Pressure (bars)** | **Fit R-Square** | **Fit RMSE** |
|---|---|---|
| 10 | 0.9997 | 1.075 |
| 20 | 1 | 0.4328 |
| 30 | 0.9996 | 1.518 |
| 40 | 0.9995 | 1.739 |
| 50 | 0.9997 | 1.294 |
| 60 | 0.9996 | 3.078 |
| 70 | 0.9996 | 2.279 |
| 80 | 0.9996 | 3.578 |
| 90 | 0.9997 | 2.406 |
| 100 | 0.9998 | 2.068 |
| 110 | 0.9998 | 1.922 |
| 120 | 0.9999 | 1.802 |

TABLE 3.1: *Exp.2* Gaussian function fit goodness for each inlet pressures

| Pressure (bars) | Standard Deviation ($\sigma$) | Mean ($\mu$) | Equation |
|---|---|---|---|
| 10 | 8.5489 | 305.8 | $f(x) = 399.7e^{-\left(\frac{x-305.8}{12.09}\right)^2}$ |
| 20 | 13.0320 | 284.5 | $f(x) = 342.5e^{-\left(\frac{x-284.5}{18.43}\right)^2}$ |
| 30 | 14.7361 | 282.9 | $f(x) = 377e^{-\left(\frac{x-282.9}{20.84}\right)^2}$ |
| 40 | 16.2493 | 289.3 | $f(x) = 370.3e^{-\left(\frac{x-289.3}{22.98}\right)^2}$ |
| 50 | 18.0524 | 288.4 | $f(x) = 352.4e^{-\left(\frac{x-288.4}{25.53}\right)^2}$ |
| 60 | 17.1049 | 282.5 | $f(x) = 724.3e^{-\left(\frac{x-282.5}{24.19}\right)^2}$ |
| 70 | 18.9999 | 284.5 | $f(x) = 480.5e^{-\left(\frac{x-284.5}{26.87}\right)^2}$ |
| 80 | 24.5336 | 286.2 | $f(x) = 694.8e^{-\left(\frac{x-286.2}{34.85}\right)^2}$ |
| 90 | 25.5336 | 288.8 | $f(x) = 532.8e^{-\left(\frac{x-288.8}{36.11}\right)^2}$ |
| 100 | 31.5228 | 290.5 | $f(x) = 496.1e^{-\left(\frac{x-290.5}{44.58}\right)^2}$ |
| 110 | 35.2210 | 296.8 | $f(x) = 531.1e^{-\left(\frac{x-296.8}{49.81}\right)^2}$ |
| 120 | 31.8693 | 306.7 | $f(x) = 686.2e^{-\left(\frac{x-306.7}{45.07}\right)^2}$ |

TABLE 3.2: *Exp.2* Gaussian function and its parameters for each inlet pressures

### 3.1.3 Best Line Fitting

To estimate the cone angle of bubbly flow, edges of the main flow jet is required to be extracted by thresholding the 3D structure at some level along Z axis. One can notice that thresholding the structure from a Z level closest to peak or bottom cannot provide sufficient edge information regarded to overall flow. By utilizing the Gaussian function nature, $Z_{max}$ and $Z_{min}$ levels are designated in relation to standard deviation ($\sigma$) and mean ($\mu$) parameters as follows

$$Z_{max} = f(\mu \mp \sigma) \tag{3.5}$$

$$Z_{min} = f(\mu \mp 2\sigma) \tag{3.6}$$

High fidelity side edge points of bubbly flow can be obtained by thresholding the 3D structure at appropriate Z levels (Figure 3.19(a)), where

$$f(\mu \mp 2\sigma) \leq Z \leq f(\mu \mp \sigma) \tag{3.7}$$

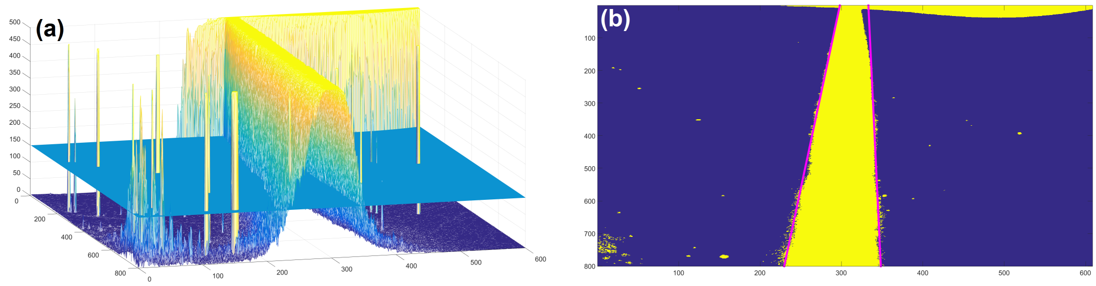


FIGURE 3.19: *Exp.2* (a) Thresholding the 3D structure at a certain Z level (b) Best lines fitting to the side edges of bubbly flow

Z levels are selected randomly in compliance with above condition and best lines are fitted to edge points (Figure 3.20(a)) acquired by thresholding the structure at this Z level.

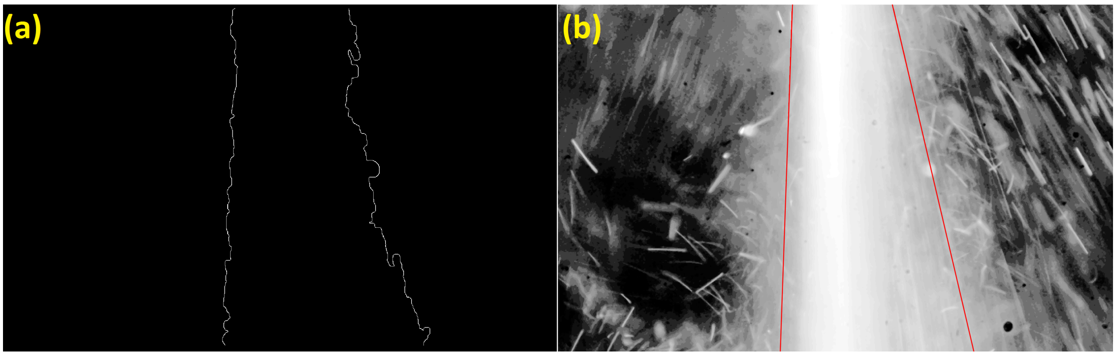


FIGURE 3.20: *Exp.2* (Pi > 50 bars) (a) Detected flow edges (b) Best line fitting

Minimization of sums of squares of geometric (perpendicular) distance from data points to the best line is implemented and the equation of the line is written as

$$sin(\alpha)x - cos(\alpha)y = \rho \tag{3.8}$$

where $\rho$ is the distance of the line from the origin and $\alpha$ is the angle between the line and positive x axis. Slope of the line (m) can be written as

$$m = -\frac{sin(\alpha)}{-cos(\alpha)} = tan(\alpha) \tag{3.9}$$

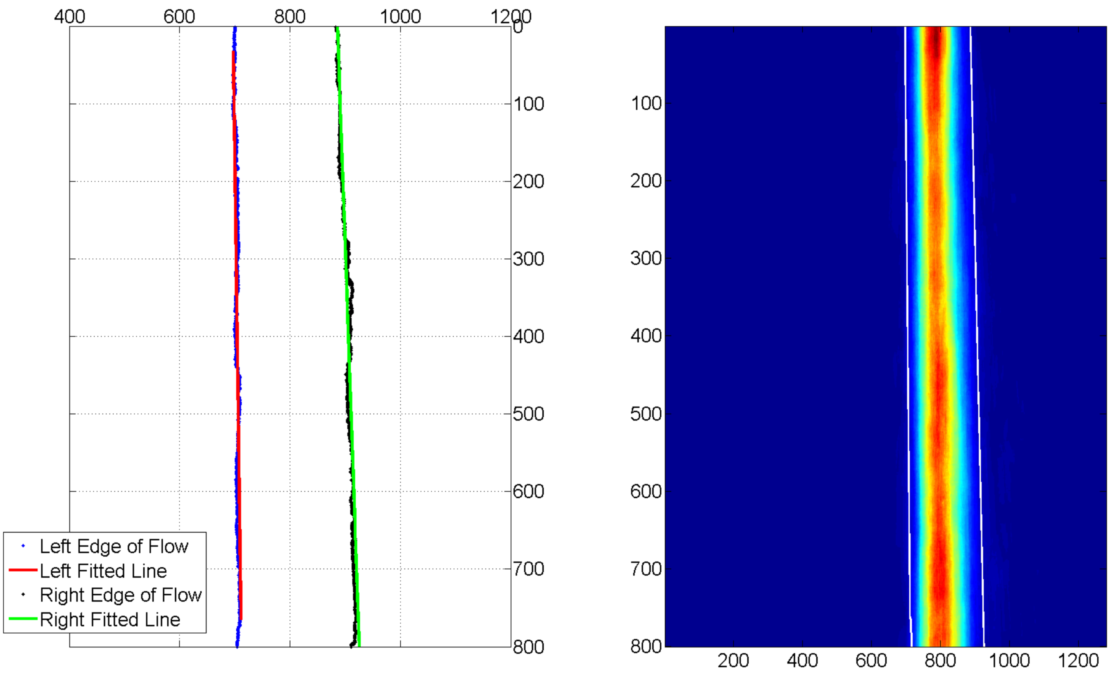


FIGURE 3.21: *Exp.1* (Pi $\leq$ 50 bars) Best lines fitting to edges

Two distinct best lines are fitted to left and right sides of the flow (Figure 3.19(b), 3.20(b) and 3.21). Cone angle of the bubbly flow can be considered as the angle between these lines (Figure 3.22) and can be calculated as

$$\theta = arctan(\frac{m_1 - m_2}{1 + m_1 m_2}) \tag{3.10}$$

where $m_1$ and $m_2$ are slopes of the lines, and $m_1 > m_2$.

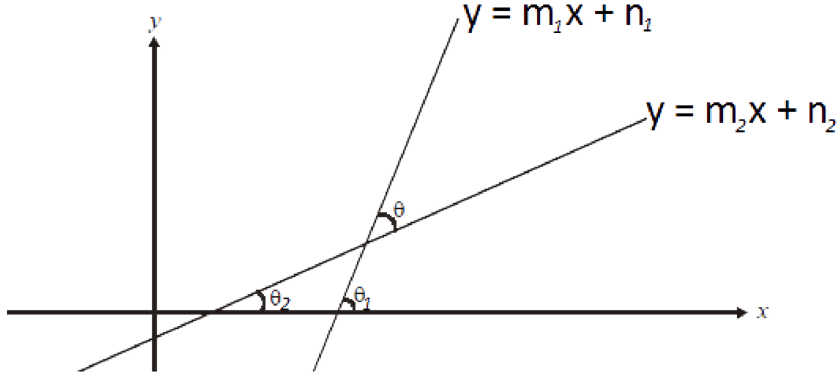


FIGURE 3.22: Angle between two lines

### 3.1.4 Kalman Filter Estimation

Cone angle ($\theta$) of the flow and angle measurements from subsequent images would be assumed to remain the same if there were no noises or disturbances. More realistically, the cone angle can be defined as the state of a dynamical system where calculated angles are considered as measurements, and both are corrupted with additive noises; i.e.

$$\theta(k+1) = \theta(k) + w(k) \tag{3.11}$$

$$z(k) = \theta(k) + v(k) \tag{3.12}$$

where $\theta(k)$ is the state of the process, $w(k)$ is the process noise, $z(k)$ is measurement and $v(k)$ is the measurement noise. Process and measurement noises are modeled by zero mean Gaussian noise with constant covariances, $C_w$ and $C_v$, respectively. Optimal state (cone angle) can be estimated by the following Kalman filter

$$\hat{\theta}(k+1|k) = \hat{\theta}(k) \tag{3.13}$$

$$P(k+1|k) = P(k) + C_w \tag{3.14}$$

$$K(k+1) = P(k+1|k)\Big(P(k+1|k) + C_v\Big)^{-1} \tag{3.15}$$

$$\hat{\theta}(k+1) = \hat{\theta}(k+1|k) + K(k+1)\Big(z(k+1) - \hat{\theta}(k+1|k)\Big) \tag{3.16}$$

$$P(k+1) = \Big(I - K(k+1)\Big)P(k+1|k) \tag{3.17}$$

where is $\hat{\theta}(k+1|k)$ the state prediction at time k+1 given all measurements and estimations up to time k, $\hat{\theta}(k)$ is the optimal state at time k. $P(k{+}1|k)$ and $P(k{+}1)$ are a priori and a posteriori covariance matrices associated with predicted and updated state estimates. $z(k+1)$ is the measurement, i.e. calculated angle from frame k+1, taken at time k+1. Covariance of the process noise ($C_w$) is initialized with a low value such as 0.001 and covariance of the measurement noise ($C_v$) is determined experimentally from calculated angles. To initialize the Kalman filter, the optimal state estimate is initialized with $\hat{\theta}(0) = 0$ and a posteriori covariance is initialized as $P(0) = 50$.

## 3.2 Scattered Bubbles Modeling

Throughout the process of hydrodynamic cavitation, multi-phase bubbly flow involves scattered bubbles around it starting from the orifice of bubbly flow generator. These initially originated bubbles are considered as the most devastating forms because of harboring the initial power depending on sudden pressure change. Intrinsically, amount of scattered bubbles depends on the inlet pressure level. To investigate the catastrophic effect of newborn bubbles just after the orifice of generator, determination of their distributions along with various inlet pressures is very essential.

As explained in Section 3.1.1, acquired shadow images were purified from the noise and disturbance and enhanced to put emphasis on pertinent regions (Figure 3.23(b)). With the help of CCA explained in Section 3.1.1.4, main jet flow and the orifice of the probe were excluded from the images based on the pixel wise area difference (Figure 3.23(c)).

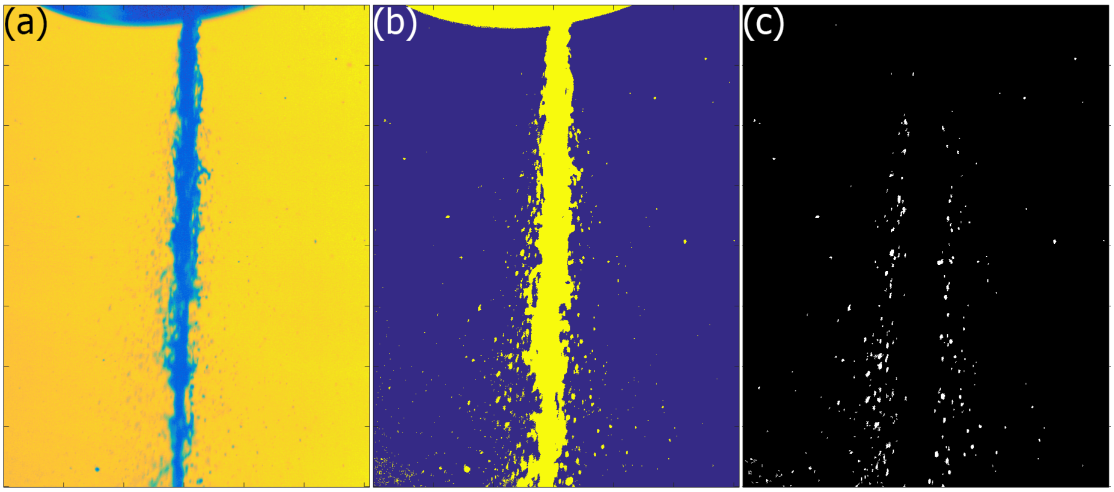


FIGURE 3.23: (a) Exit from the orifice (b) Pre-processed and labelled image (c) Scattered bubbles around main flow

All scattered bubbles under various inlet pressures ($10 \leq \mathrm{Pi} \leq 120$ bars) were extracted as far as possible. The entities of them became more frequent close to main jet flow and rare farther. Distributions are obtained by segmenting the bubbles in specified horizontal intervals and two peak Gaussian distribution forms were observed (Figure 3.24).

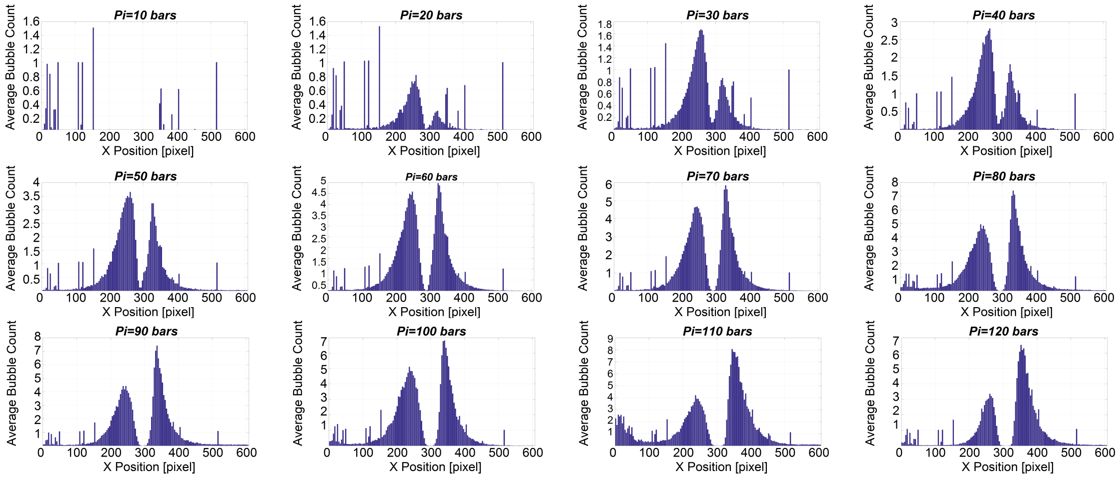


FIGURE 3.24: Scattered bubbles distributions ($10 \leq \mathrm{Pi} \leq 120$ bars)

Characterization of the scattered bubbles distribution was done by modeling the left and right side of bubbles separately as Gaussian (normal) distribution and exploration of semi-axis lengths of ellipse based on covariance matrix is proposed (Figure 3.25).

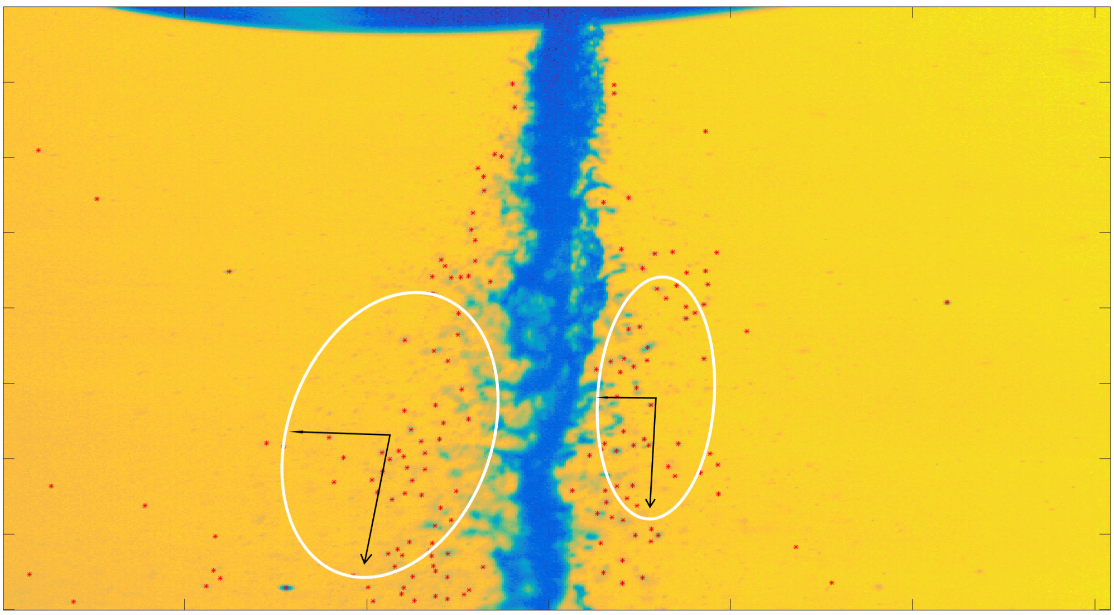

FIGURE 3.25: Scattered bubbles detection and distribution modeling

Under ascending inlet pressures, the orientation and semi-axis lengths of the ellipses change in different manners, which are depicted with 3 different random frames for each inlet pressures in Figure 3.26.

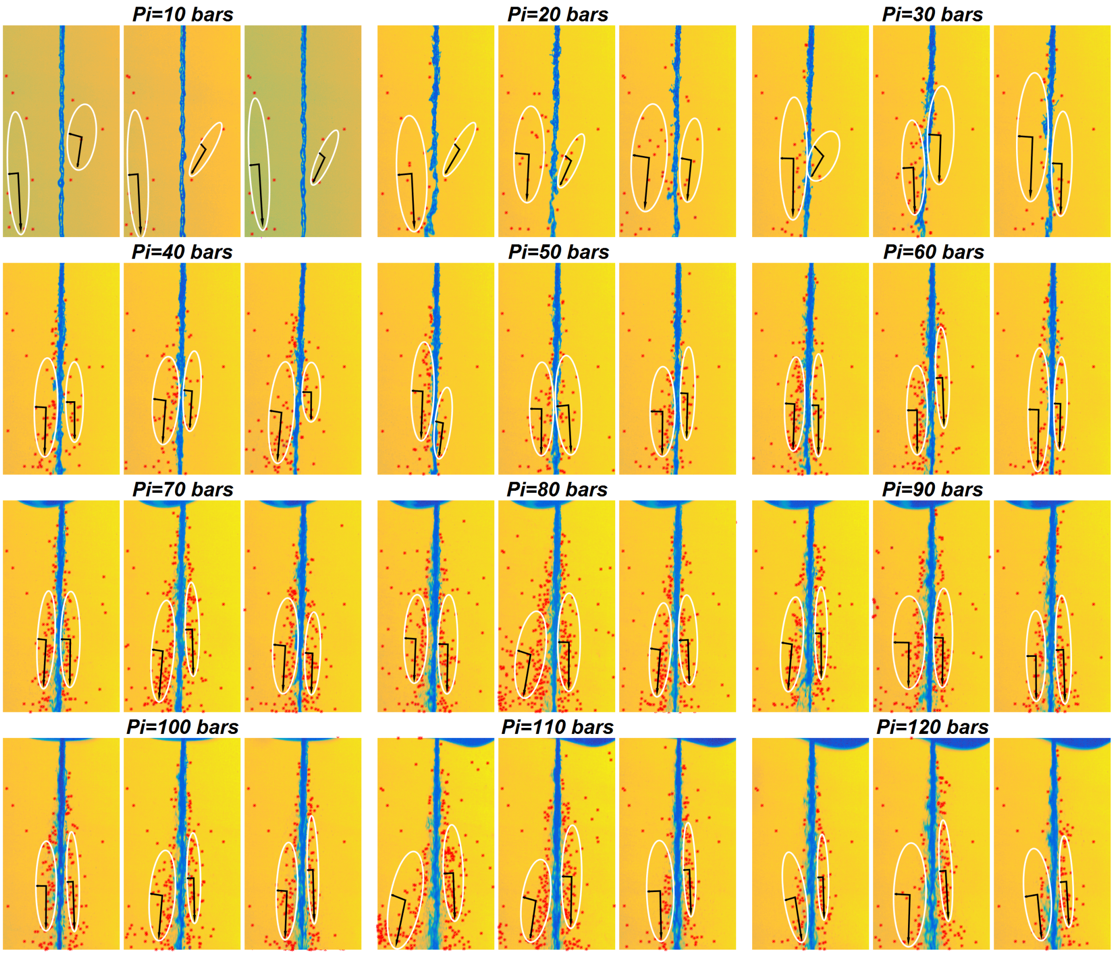


FIGURE 3.26: Changing orientation and axis lengths of the ellipses in various inlet pressures

The distribution of bubble centroids could be represented by axes magnitudes and orientation of an ellipse, which based on the variance of the centroid data. If the axes of this ellipse, parallel to x-y, then equation can be written in terms of standard deviations as

$$\left(\frac{x}{\sigma_1}\right)^2 + \left(\frac{y}{\sigma_2}\right)^2 = s \tag{3.18}$$

s is the scale of ellipse, which represents the confidence level according to Chi-Square likelihood [93].

Corresponding ellipses don't have to be aligned along with x-y axis, so non-zero covariance can exist. Eigenvalues and eigenvectors of covariance matrix of the bubble centroid data were utilized to determine semi-axis lengths and directions of the ellipse. Major (a) and minor (b) axis lengths of the ellipses can be calculated as follows

$$a = \sqrt{\lambda_{max}} \tag{3.19}$$

$$b = \sqrt{\lambda_{min}} \tag{3.20}$$

where $\lambda_{max}$ and $\lambda_{min}$ are largest and smallest eigenvalues of covariance matrix of bubble centroid data respectively and semi-axis directions are determined by corresponding eigenvectors ($v_{max}$,$v_{min}$). Angle between major axes and horizontal axes can be calculated from the largest eigenvector as

$$\alpha = atan2(v_{max}(2), v_{max}(1)) \tag{3.21}$$

Ultimately, points on the ellipse can be generated by the mean of the centroid position data $[X_\mu, Y_\mu]^T$ and $\beta \in [0, 2\pi)$ as

$$\begin{bmatrix} X_e \\ Y_e \end{bmatrix} = \begin{bmatrix} cos(\alpha) & -sin(\alpha) \\ sin(\alpha) & cos(\alpha) \end{bmatrix} \begin{bmatrix} a.cos(\beta) \\ b.sin(\beta) \end{bmatrix} + \begin{bmatrix} X_\mu \\ Y_\mu \end{bmatrix} \tag{3.22}$$

# Chapter 4

# Visual Tracking of Single, Double, Triple Cavitation Bubbles

Hydrodynamic cavitation generates several bubbles/droplets which size, amount, speed and shape depend on varying inlet pressure levels. These physical quantities are key features determining the devastating impact during hydrodynamic cavitation as a biomedical application tool. To investigate the relations between these physical features and destructiveness in various inlet pressures and designate the optimum required pressure level for a specific task during biomedical applications, hydrodynamic cavitation caused bubbles must be detected and tracked throughout the multiphase flow and their morphological properties have to be extracted.

Although recent advances in imaging technologies enable us to visualize structures in micro scale with high speed cameras, robust image and video processing algorithms are still needed to handle the problems in detection and tracking processes. Within this context, some specific problems in bubble detection and tracking procedure can be listed as:

1. Simultaneous illumination changes may result in undesired reflections and shadows.

2. Monitored bubbles can be very similar and cannot be distinguished from each other.

3. Tracked single bubble can undergo dramatic morphological changes during the motion.

4. Tracking may be disturbed by partial or full occlusions by another bubbles.

5. Several bubbles can merge and form a bigger one.

6. One big bubble can split into several small ones.

7. Split and merge events may follow each other frequently.

To overcome some of these problems and achieve a high tracking performance, a new bubble tracking method is presented. Proposed tracking method can be implemented with two consecutive stages: **(i)** segmentation of bubbles individually and **(ii)** tracking of predefined single, dual or triple bubbles in upcoming video frames.

## 4.1 Bubble Segmentation

Particle Shadow Sizing (PSS) technique provides grayscale image sequence and illumination in each frames depends on bubbles' structures and concentration. As stated in Chapter 3, imaging system architecture enables to visualize the bubbles individually and separate from the main multiphase jet flow in $3^{rd}$ segment, corresponds to 9 mm distance after the orifice (Figure 3.1) with the inlet pressure level below 30 bars. Segmentation of bubbles in each frames individually requires a series of image processing steps similar to Section 3.1.1.

Since obtained images have insufficient contrast to segment foreground and background easily, stretching operation is applied as depicted in Section 3.1.1.1 to enhance the noticeability (Figure 5.4).

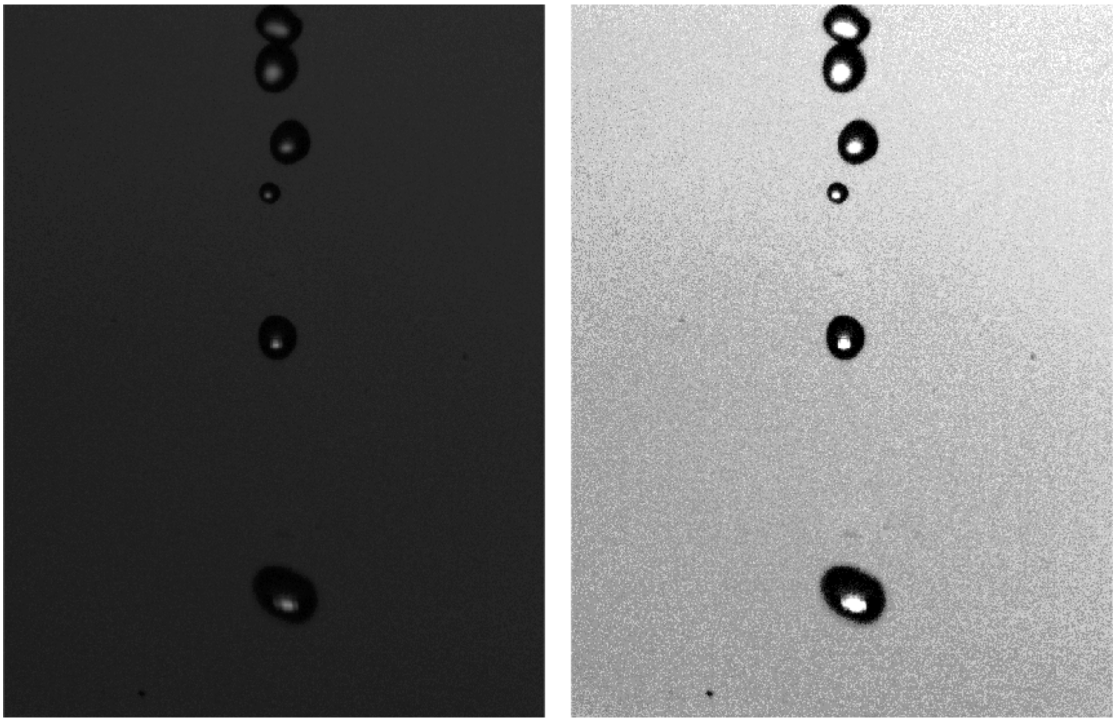

FIGURE 4.1: (a) Unprocessed original image (b) Contrast adjusted image

Stretching operation distributes the grayscale levels roughly uniformly along the histogram scale to increase the contrast (Figure 4.2).

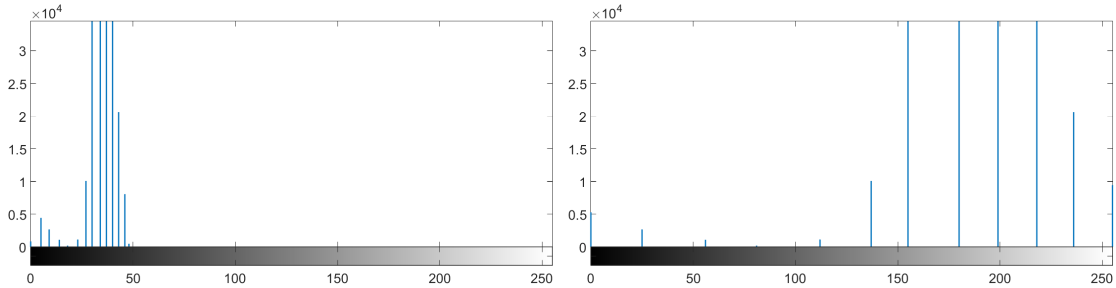


FIGURE 4.2: (a) Unprocessed histogram (b) Contrast adjusted histogram

As distinct from common segmentation methods, extracting the contours of the bubbles with high precision is important for both robustness of tracker and accurate contour modeling. For this purpose, wisely selected structuring element is utilized in morphological opening operation to eliminate noises and sharpen the edges of bubbles (Figure 4.3 (a)).

An optimum threshold level is determined as in Section 3.1.1.3 and applied to morphologically opened image. Since some parts of bubbles reflect the light and rest absorb, shadow images may contain some gaps after thresholding (Figure 4.3 (b)). Thus, image filling operation is applied as a final step (Figure 4.3 (c)).

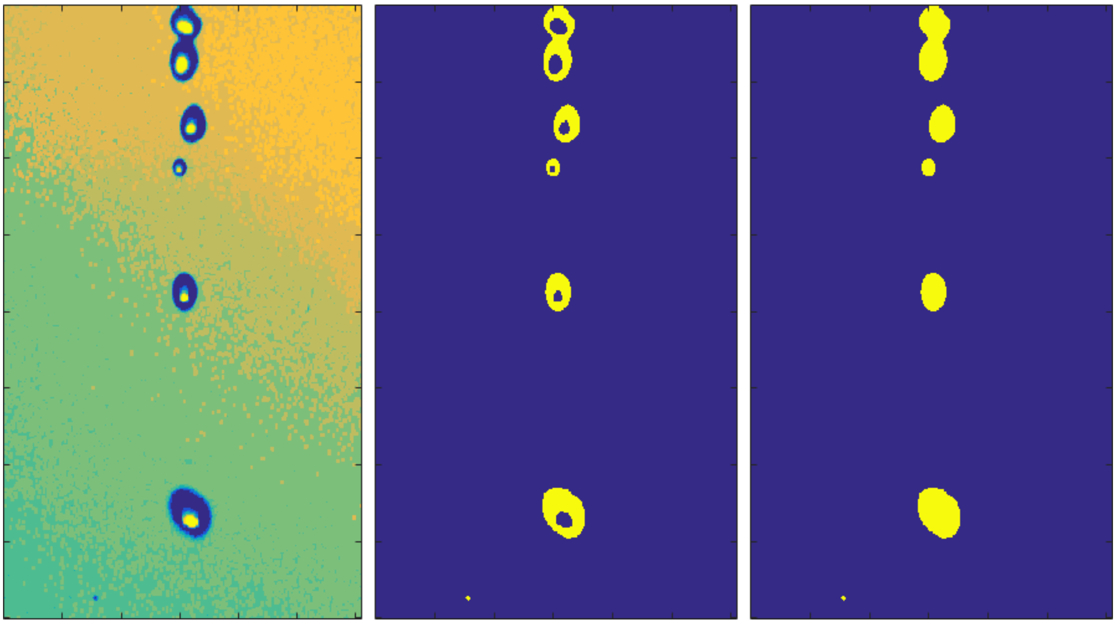

FIGURE 4.3: (a) Morphological operation (b) Thresholding (c) Image filling

Finally obtained binary image represents the locations of bubbles as foreground, which are then labelled via Connected Component Analysis (CCA) and important properties of bubble regions are extracted such as

- Center of mass coordinates ($C_x$,$C_y$)
- Area
- Eccentricity

Segmented/labelled bubble regions are stored in vertical centroid location order and identification number is assigned each of them according to this order. In addition to these properties, Canny edge detection algorithm [45] is implemented to find the edge pixels of the image and calculate the circumferences of the bubble regions.

# 4.2 Tracking

## 4.2.1 Single Bubble Tracking

In Section 2.3, various tracking methods are investigated under several groups based on the representation of the target. Particle shadow sizing technique provides us the silhouettes of the bubbles, thus images contain only structural information, color and texture information cannot be recovered by this visualization. Profitably the imaging architecture supply remarkable motion information with high speed cameras.

Taking into account all of these, structural and motion characteristics of bubbles are utilized to represent the target of the tracking. Motion information is then checked again to increase the robustness and accuracy. Feature vector of a bubble object based on structural properties are formed as

$$Obj = \begin{bmatrix} C_x \\ C_y \\ E \\ p \\ A \\ T \end{bmatrix} \tag{4.1}$$

where $C_x$ and $C_y$ are the center of mass coordinates, E is eccentricity, p is circumference, A is area and T is thinness ratio which is calculated as

$$T = \frac{4\pi A}{p^2} \tag{4.2}$$

Feature vectors (Eq 4.1) of each segmented bubble regions are calculated in consecutive frames. Since a single bubble may change its shape during the flow motion, instead of looking for a match of the object precisely in candidates, smallest shape variations are searched. It is assumed that mass/volume of a bubble must be conserved, so changes in eccentricity, thinness ratio, area and circumference should compensate each other. Bubble vertical center of mass is directly related to the velocity of the bubble against gravitational force, which could be assumed as slightly changing for a single bubble.

Preselected one single bubble feature vector (Obj) is compared with the feature vectors (Tar) in next frame and well-known Bhattacharyya distance [94] is employed to find the similarity between two feature vectors. Bhattacharyya distance can be calculated as

$$D_B(Obj, Tar) = \frac{1}{4} ln\left(\frac{1}{4}\left(\frac{\sigma^2_{Obj}}{\sigma^2_{Tar}} + \frac{\sigma^2_{Tar}}{\sigma^2_{Obj}} + 2\right)\right) + \frac{1}{4}\left(\frac{(\mu_{Obj} - \mu_{Tar})^2}{\sigma^2_{Obj} + \sigma^2_{Tar}}\right) \tag{4.3}$$

where $D_B(Obj, Tar)$ is Bhattacharyya distance between object feature vector (Obj) and target feature vector (Tar), $\sigma^2_{Obj}$ and $\sigma^2_{Tar}$ are variances, $\mu_{Obj}$ and $\mu_{Tar}$ are means of the object and target feature vectors respectively.

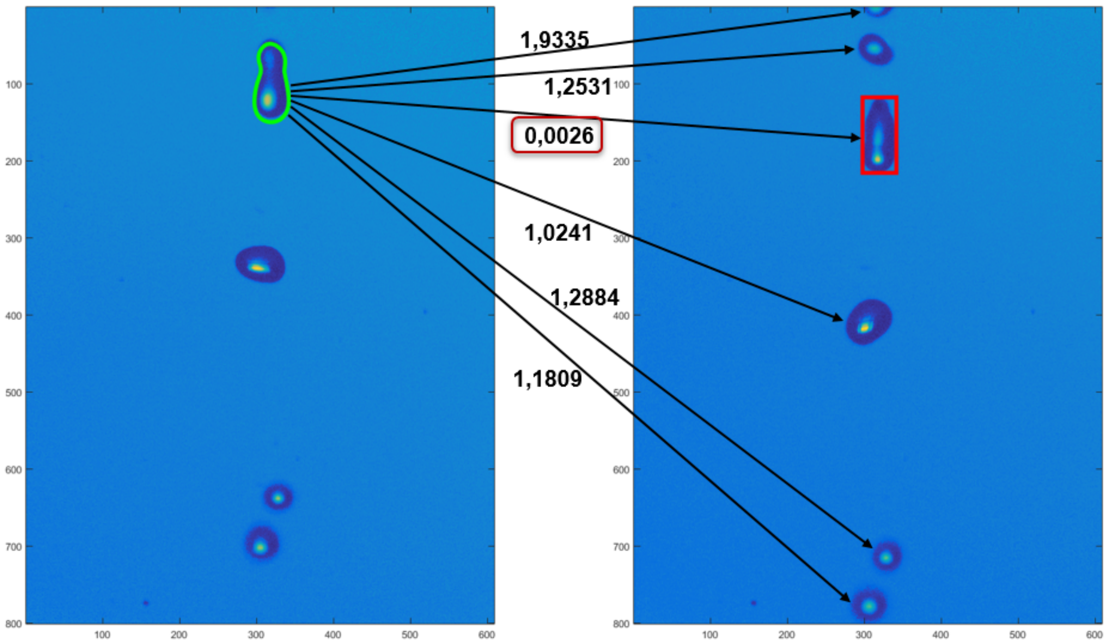


FIGURE 4.4: Bhattacharyya distances between consecutive frames

If object bubble is monitored in the next frame, minimum Bhattacharyya distance between these vectors would belong to the targeted bubble (Figure 4.4). In addition to minimum $D_B$, vertical position change is also checked. Since bubbles flow downward and their speed is slightly changing, negative vertical change and abnormal traveled distance are penalized via increasing the corresponding $D_B$ (Algorithm4.1).

**Algorithm 4.1** Single Bubble Tracking

```
Construct Object feature vector via segmentation
Initialization:
    IsTracked=true;
    d=maximum possible travel distance;
    maxDB=maximum Bhattacharyya distance to go on tracking;
while IsTracked == true do
    Segment the next frame
    Construct the target feature vectors of each bubble regions
    Calculate each of D_B(Obj,Tar)
    if (Tar(2)-Obj(2) < 0) || (Tar(2)-Obj(2) > d)
        Penalizing: Increase the D_B
    endif
    Select the target bubble according to minimum D_B
    if (min(D_B) > maxDB)
        End of tracking: IsTracked = false
    else
        Obj ← Tar
    endif
end
```

Finally, selected single bubble can be tracked throughout the flow until it exits from the field of view (Figure 4.5).

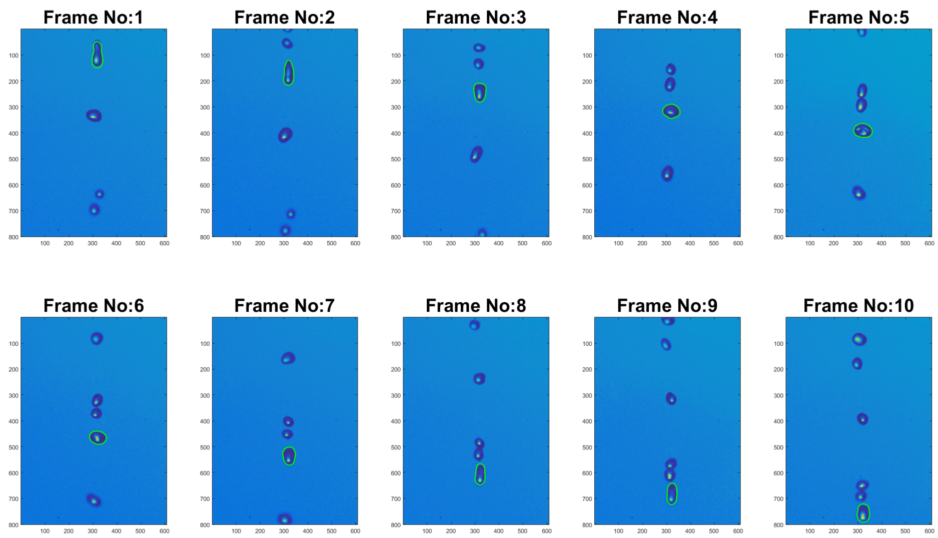


FIGURE 4.5: Single bubble tracking throughout the flow

### 4.2.2 Double and Triple Bubble Tracking

During hydrodynamic cavitation, it is observed that frequently two single bubbles come together and merge to form a bigger one, additionally big bubbles also tend to split into two single bubbles as well. Two close bubbles do not always merge but prefer to move as attached each other.

When the amount of bubbles increase within the field of view, more than two bubbles are also come together to merge or attach each other. Ordinarily triple bubbles interact each other since obtained bubbles are in micro scale. In case of more than three interactions, closely interacted two or three bubbles merge together.

To investigate the relation between closely travelling bubbles and to decide the merge or attach condition, tracking of double and triple bubbles must be performed. In order to achieve double/triple bubble tracking, selected two/three bubbles are considered as a whole structure, a slight modification is applied to Equation 4.1 and Algorithm 4.2 can be implemented by

$$Obj = \begin{bmatrix} C_{totalx} \\ C_{totaly} \\ p_{total} \\ A_{total} \\ T_{total} \end{bmatrix} \tag{4.4}$$

where $C_{totalx}$ and $C_{totaly}$ are center of mass coordinates of double/triple bubble structure. Since eccentricity is meaningless for separate structures, E is excluded from the feature vector. Thinness ratio (T), circumference (p) and area (A) values are calculated by assuming the double/triple bubbles as a single structure.

Obviously, tracker must follow the target in cases of merge and split, so it must change its mode as single, double or triple bubble tracking with respect to minimum Bhattacharyya distance (Figure 4.6, 4.7, 4.8). To visualize the current mode of tracker, just contour of the bubble is highlighted for single bubble tracking, contours of the bubbles and also convex hull of the bubbles are highlighted for double bubble tracking (Figure 4.9) and finally contours of bubbles and the triangle obtained by three centers of the bubbles are highlighted for triple bubble tracking.

**Algorithm 4.2** Double/Triple Bubble Tracking

Construct Object feature vector via segmentation (Single/Double/Triple)
**Initialization:**
    IsTracked=true;
    d=maximum possible travel distance;
    maxDB=maximum Bhattacharyya distance to go on tracking;
**while** IsTracked == true **do**
    Segment the next frame
    Construct the target feature vectors of each single bubble regions
    Order the segmented regions vertically ascending
    Construct the target feature vectors of each consecutive double bubbles
    Construct the target feature vectors of each consecutive triple bubbles
    Calculate each of $D_B(Obj, Tar)$ for single, double and triple
    **if** (Tar(2)-Obj(2) $<$ 0) || (Tar(2)-Obj(2) $>$ d)
        *Penalizing:* Increase the $D_B$
    **endif**
    Select the target bubble according to minimum $D_B$
    **if** (min($D_B$) $>$ maxDB)
        *End of tracking:* IsTracked = false
    **else**
        Obj $\leftarrow$ Tar
    **endif**
**end**

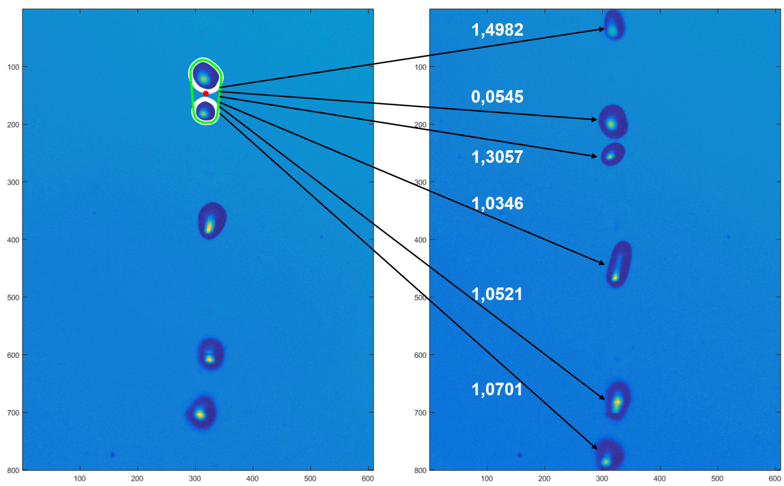


FIGURE 4.6: $D_B$ values between object vector and single target vectors

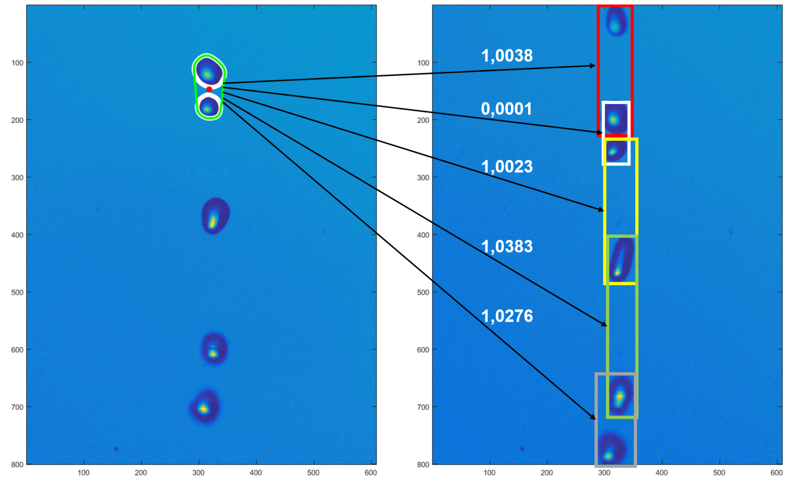


FIGURE 4.7: $D_B$ values between object vector and double target vectors

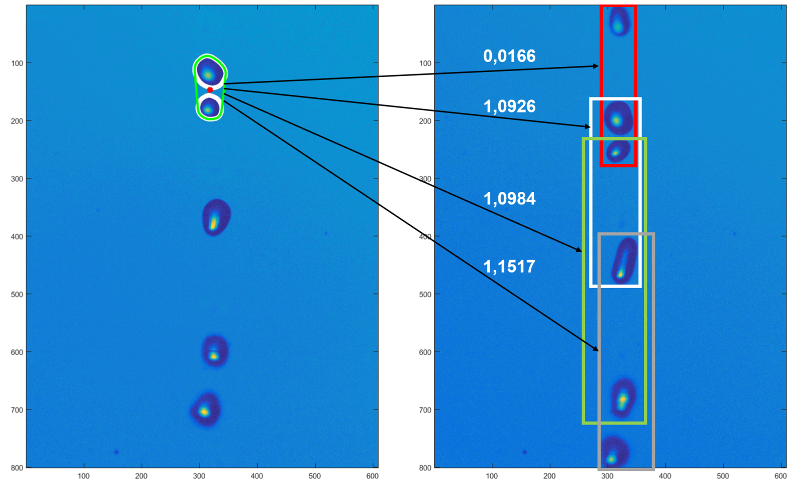


FIGURE 4.8: $D_B$ values between object vector and triple target vectors

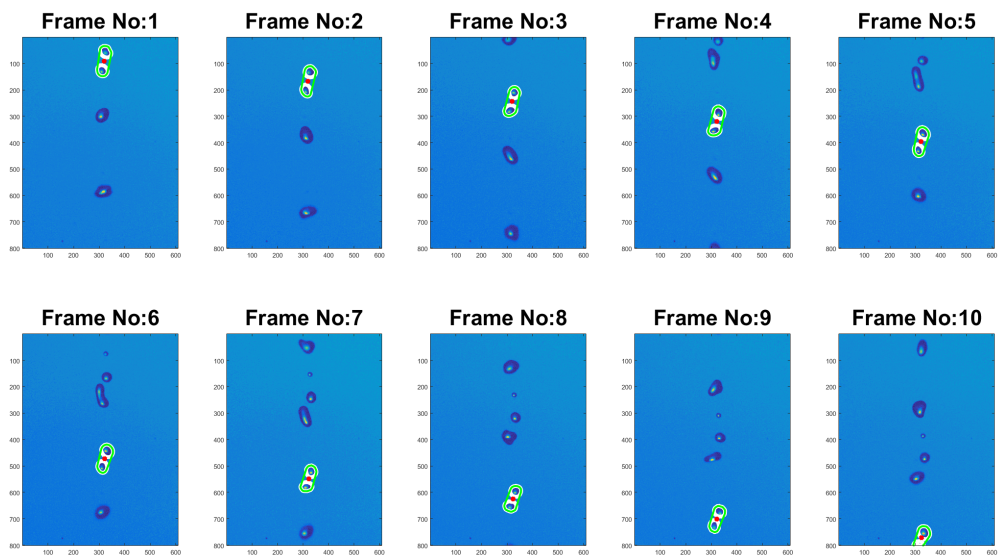


FIGURE 4.9: Double bubble tracking throughout the flow

# Chapter 5

# Modeling of Cavitation Bubbles using Elliptic Fourier Descriptors

Throughout the tracking of cavitation bubbles in Section 4, structural and motion properties are utilized. In each frame, tracked bubbles' contours are segmented from background to extract circumferences and areas, and construct the feature vector for the tracker. Segmented contours show the evolution of the bubble along with the fluid flow. It is suspected that the evolution of the bubble contours may contain useful information related to hydrodynamic cavitation and the released opinions could be exploited in the usage of hydrodynamic cavitation as a tool for several biomedical applications.

Shape evolution of cavitation bubbles can be considered as a closed curve changing over time. Curve's data points are the edge pixels of segmented bubble contours and can be written as

$$\begin{aligned} x(s) &= x(s+L) \\ y(s) &= y(s+L) \end{aligned} \tag{5.1}$$

where $x(s)$ and $y(s)$ are horizontal and vertical functions of closed curve with arc length parameter $s$ and total length of the curve $L$. Since equations in 5.1 are periodic with $L$, the well-known elliptic Fourier descriptors (EFD) [95] can be employed as

$$x(\theta) = a_0 + \sum_{k=1}^{n} (a_k cosk\theta + b_k sink\theta)$$
$$y(\theta) = c_0 + \sum_{k=1}^{n} (c_k cosk\theta + d_k sink\theta) \tag{5.2}$$

where edge pixel locations of segmented contours, $x$ and $y$ are written as a function of normalized parameter $\theta$ as

$$\theta = \frac{s}{L} 2\pi \tag{5.3}$$

where $\theta \in [0, 2\pi)$ for $s \in [0, L)$. Since $\theta$ is an angle and can be written as $\theta = wt$ where $w$ is angular velocity of moving pixel point on the closed edge contour, by assigning $w = 1$ rad/sec, $\theta$ can be easily related to time as $\theta = t$. Now, edge pixel locations x and y are described with periodic functions of $t$ with period $\frac{2\pi}{w}$.

In equation 5.2, $n$ is total number of harmonics, so it is a positive integer. Initial coefficients, which are actually the center of mass coordinates, can be calculated by

$$a_0 = \frac{1}{N} \sum_{i=1}^{N} x_i$$
$$c_0 = \frac{1}{N} \sum_{i=1}^{N} y_i \tag{5.4}$$

Rest of the coefficients in EFD can be found as

$$a_k = \frac{2}{N} \sum_{i=1}^{N} x_i cos(kwt)$$
$$b_k = \frac{2}{N} \sum_{i=1}^{N} x_i sin(kwt)$$
$$c_k = \frac{2}{N} \sum_{i=1}^{N} y_i cos(kwt) \tag{5.5}$$
$$d_k = \frac{2}{N} \sum_{i=1}^{N} y_i sin(kwt)$$

First harmonic gives an ellipse located at $(a_0,c_0)$ and covers the whole closed curve. After that few harmonics construct the curve roughly. Increasing the number of the harmonics enable to embrace the details related to closed curve. Theoretically, infinite number of harmonics must recover the whole closed curve with precise details but in practice, high precision in closed curve modeling may not be necessary depending on the scenario.

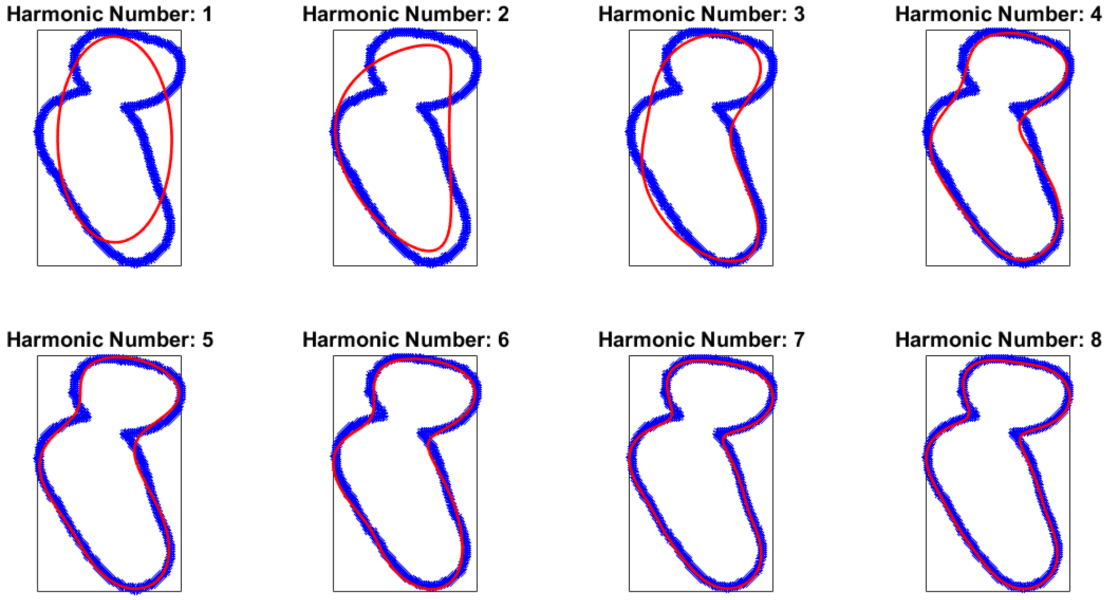


FIGURE 5.1: Blue: Data points Red: EFD Modeling

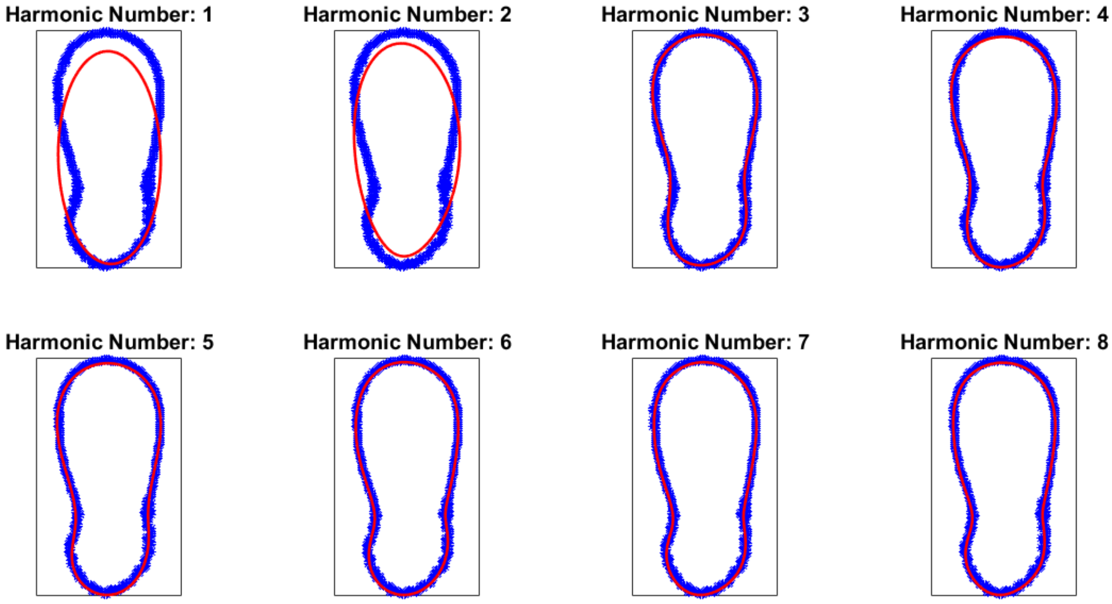


FIGURE 5.2: Blue: Data points Red: EFD Modeling

In the case of EFD modeling of segmented bubble contours, data points are extracted from the images with the help of a series segmentation techniques 4.1. Naturally these points are disturbed by noises and trying to find best fit with higher number of harmonics is an inconvenient idea. Since complex contours can be roughly represented by 5-10 harmonics, optimum number of harmonics $n$ is chosen to be 8 for EFD modeling of cavitation bubbles.

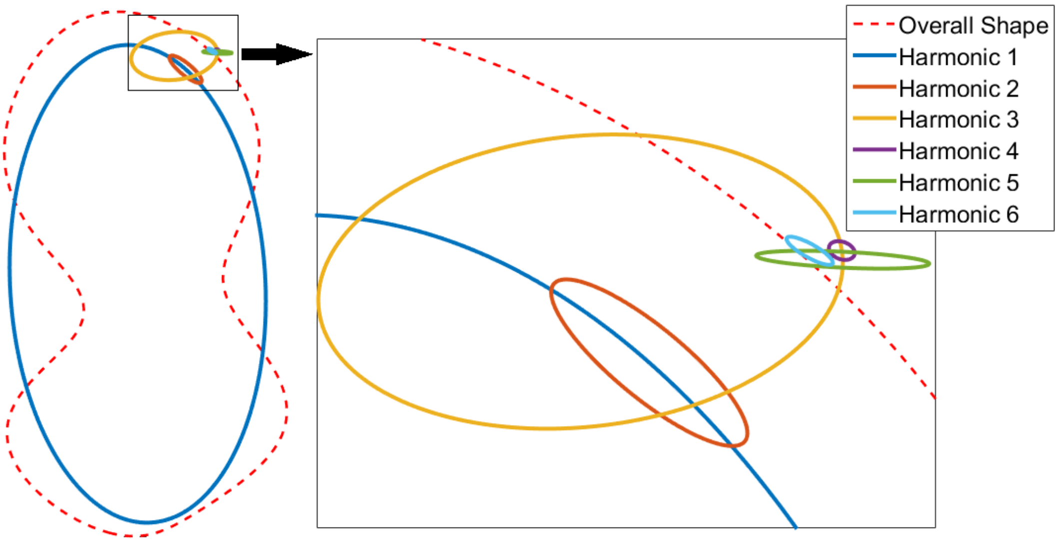


FIGURE 5.3: 6 Harmonic ellipses

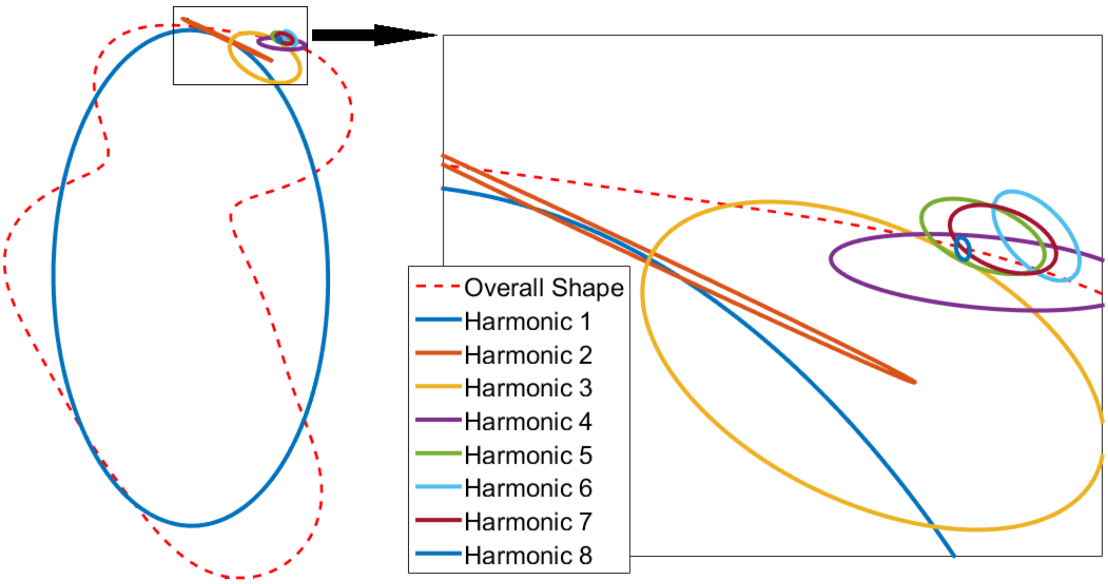


FIGURE 5.4: 8 Harmonic ellipses

Once the closed curve is modeled by elliptic Fourier descriptors, it can be represented by $n$ harmonic ellipses used in 5.2. Major and minor semi axis lengths and the angle between horizontal line and major axis can be retrieved with the corresponding coefficients $(a_k, b_k, c_k, d_k)$ by forming the matrix $E$ as follows:

$$E = \begin{bmatrix} a_k & b_k \\ c_k & d_k \end{bmatrix} \tag{5.6}$$

$EE^T$ can be decomposed into eigenvalues and corresponding eigenvectors by

$$EE^T = R_\phi S R_\phi^T \tag{5.7}$$

Major axis length $(a)$, minor axis length $(b)$ and angle between major axis and horizontal axis $(\theta)$ can be calculated as

$$a = \sqrt{\lambda_{max}} \tag{5.8}$$

$$b = \sqrt{\lambda_{min}} \tag{5.9}$$

$$\theta = atan2(V(2), V(1)) \tag{5.10}$$

where $\lambda_{max}$ and $\lambda_{min}$ are maximum and minimum eigenvalues of $EE^T$ respectively (diagonal elements of S) and $V$ is the eigenvector corresponding to the largest eigenvalue of $EE^T$.

Obtained characteristic properties of each ellipse $(a, b, \theta)$ are utilized to investigate invariant properties of EFD modeled cavitation bubbles. Feature vectors of $i^{th}$ frame for each characteristic properties with $N$ harmonics are formed as

$$\begin{aligned} f_{ai} &= [a_1 \quad a_2 \quad \dots \quad a_N]^T \\ f_{bi} &= [b_1 \quad b_2 \quad \dots \quad b_N]^T \\ f_{\theta i} &= [\theta_1 \quad \theta_2 \quad \dots \quad \theta_N]^T \end{aligned} \tag{5.11}$$

Covariance of each feature data can be calculated as

$$\begin{aligned}
\Sigma_a &= \frac{1}{m}\sum_{i=1}^{m}(f_{ai}-\bar{f}_a)(f_{ai}-\bar{f}_a)^T \\
\Sigma_b &= \frac{1}{m}\sum_{i=1}^{m}(f_{bi}-\bar{f}_b)(f_{bi}-\bar{f}_b)^T \\
\Sigma_\theta &= \frac{1}{m}\sum_{i=1}^{m}(f_{\theta i}-\bar{f}_\theta)(f_{\theta i}-\bar{f}_\theta)^T
\end{aligned} \tag{5.12}$$

where $m$ is total number of tracked frames and $\bar{f}_a, \bar{f}_b, \bar{f}_\theta$ are calculated as

$$\begin{aligned}
\bar{f}_a &= \frac{1}{m}\sum_{i=1}^{m} f_{ai} \\
\bar{f}_b &= \frac{1}{m}\sum_{i=1}^{m} f_{bi} \\
\bar{f}_\theta &= \frac{1}{m}\sum_{i=1}^{m} f_{\theta i}
\end{aligned} \tag{5.13}$$

Root-mean-square (RMS) values of each columns of covariance matrices demonstrate the dominance of the corresponding feature with respect to other features.

# Chapter 6

# Experimental Results

## 6.1 Cone Angle Estimation

As stated in Chapter 3, cone angle estimation procedure is implemented to the images acquired by two different illumination configurations. Angle estimation is performed via random selection of Z values according to Equation 3.7 below medium inlet pressure ($Pi < 60$ bars) in **Experiment 1**

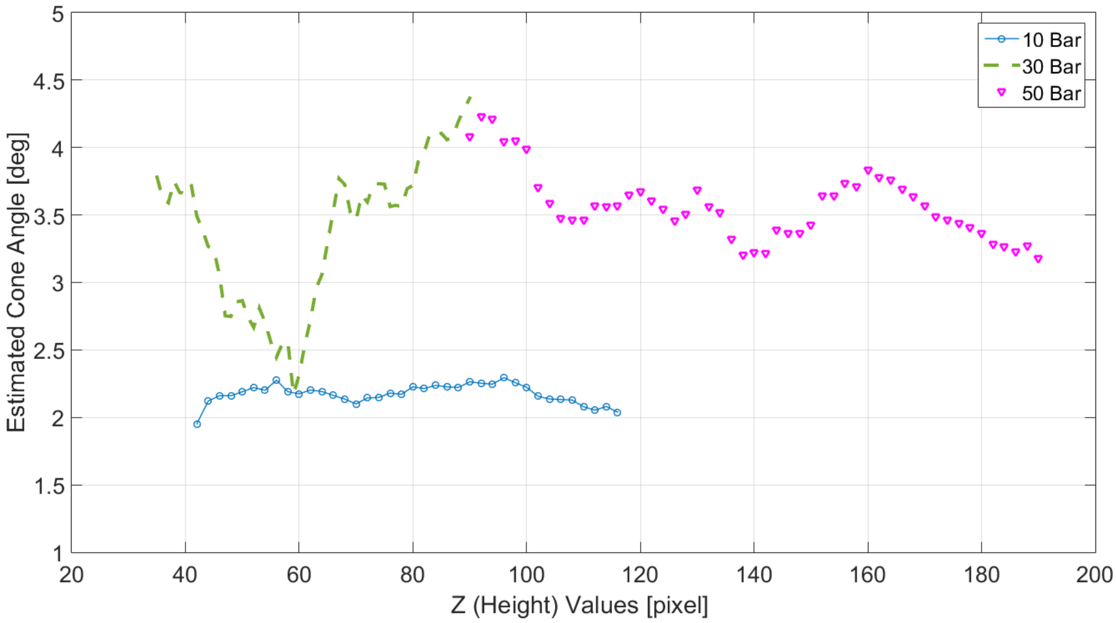


FIGURE 6.1: *Exp.1* Estimated cone angles with different inlet pressures (10, 30, 50 bars)

Results in Figure 6.1 show that with $Pi = 10$ bars pressure, virtual cone angle can be estimated around 2.1 degrees. Increasing the Pi pressure, leads to increase in cone angle as well. 30 bars inlet pressure forms around 3.3 degrees cone angle, whereas the angle is around 3.5 degrees with 50 bars inlet pressure.

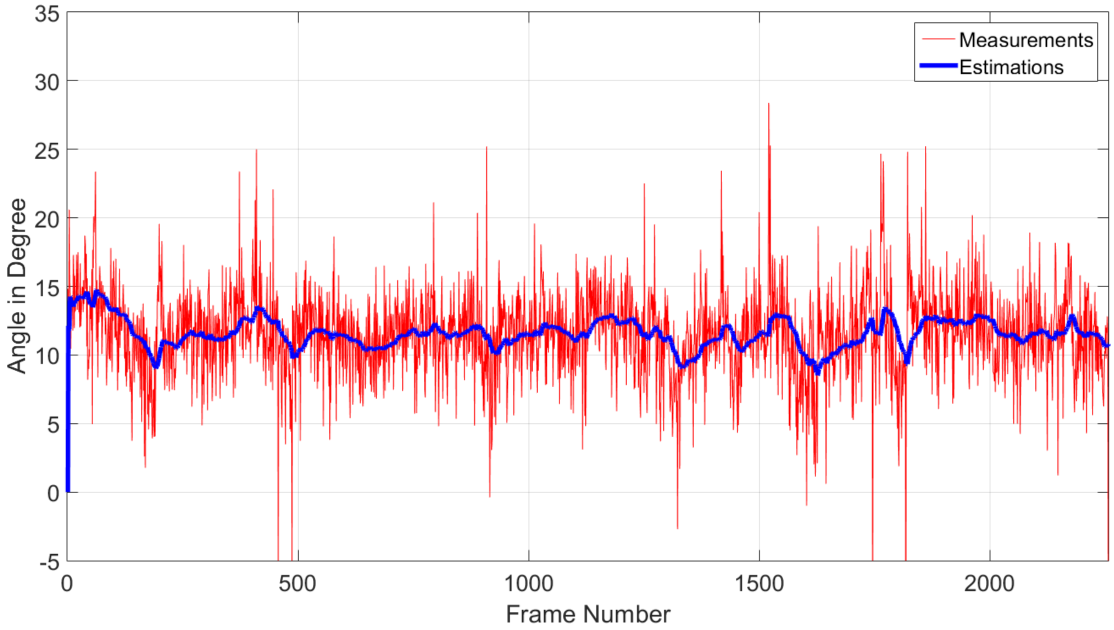


Figure 6.2: *Exp.1* Estimated cone angles with inlet pressure Pi=80 bars

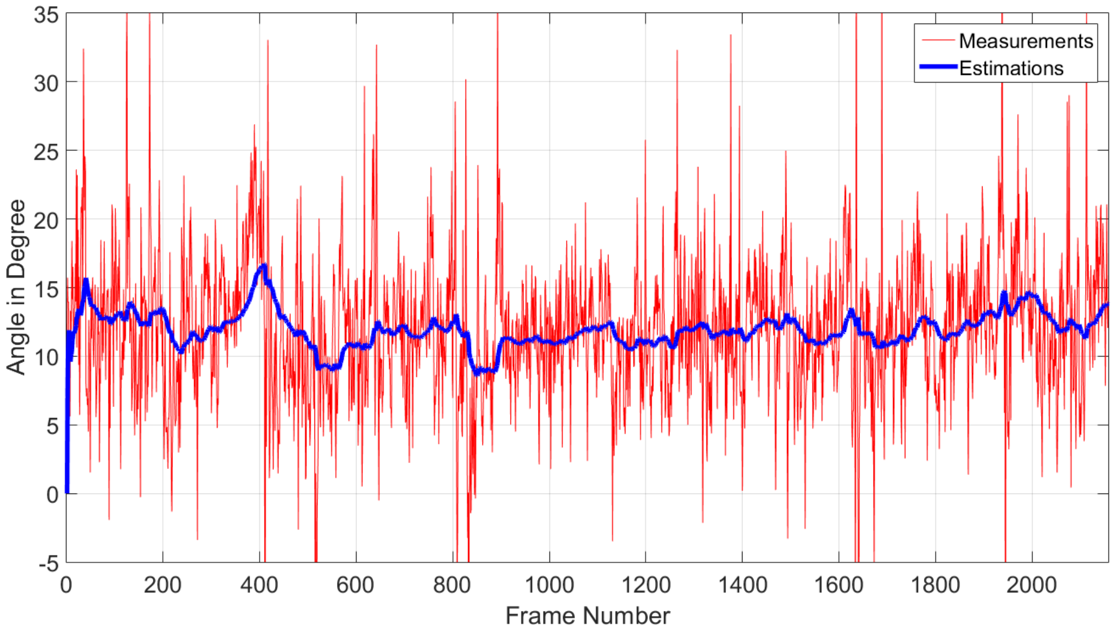


Figure 6.3: *Exp.1* Estimated cone angles with inlet pressure Pi=100 bars

With inlet pressure above 60 bars, Kalman filter results show that estimations are highly smoothed versions of the calculated angles from images (Figure 6.2, 6.3,

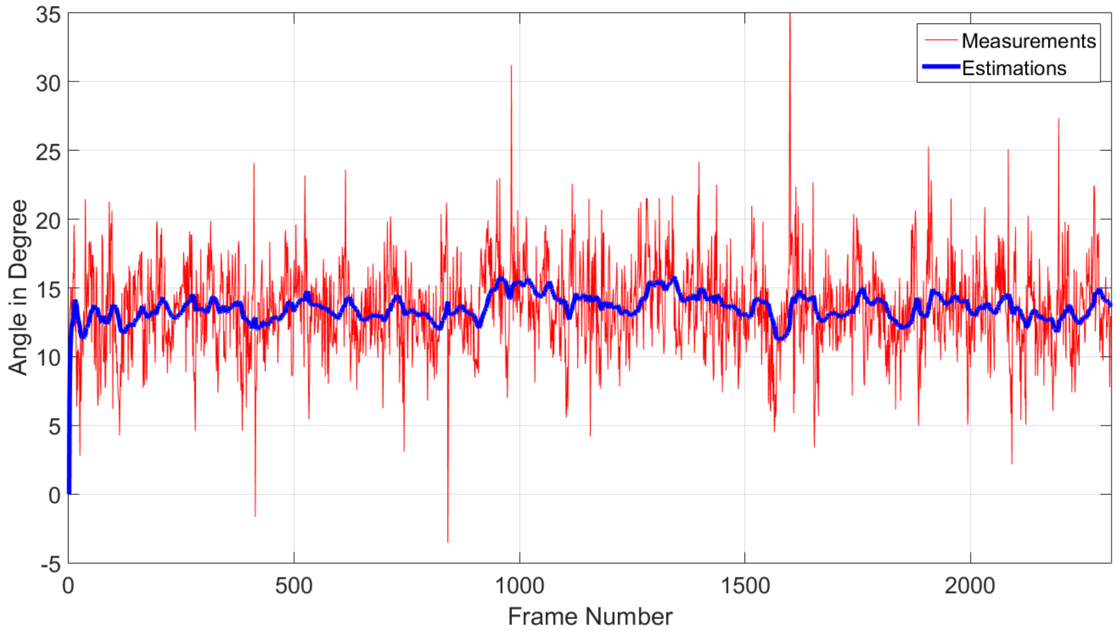


FIGURE 6.4: *Exp.1* Estimated cone angles with inlet pressure Pi=120 bars

6.4). Average of estimations, exhibit the same behaviour as lower inlet pressures. Increasing pressure above 60 bars to 120 bars, estimated angles reached up to 13 degrees.

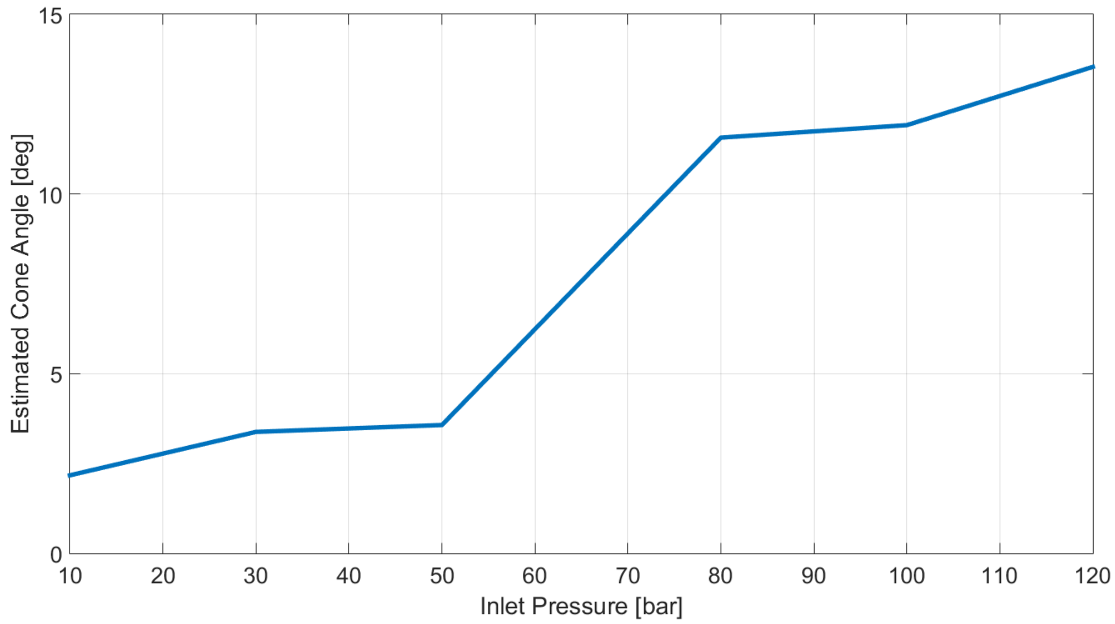


FIGURE 6.5: *Exp.1* Estimated angles through 10 to 120 bar inlet pressures

Finally, all estimated angles from various inlet pressures from 10 to 120 bars are gathered and showed in Figure 6.5. Results show that, cone angle of bubbly flow changes with proportional to inlet pressure from 2 to 14 degrees.

In **Experiment 2**, results of the cone angle estimation by Kalman filter are depicted in Figures 6.6, 6.7, 6.8 where at each pressure level several image frames are captured and processed to get angle measurements.

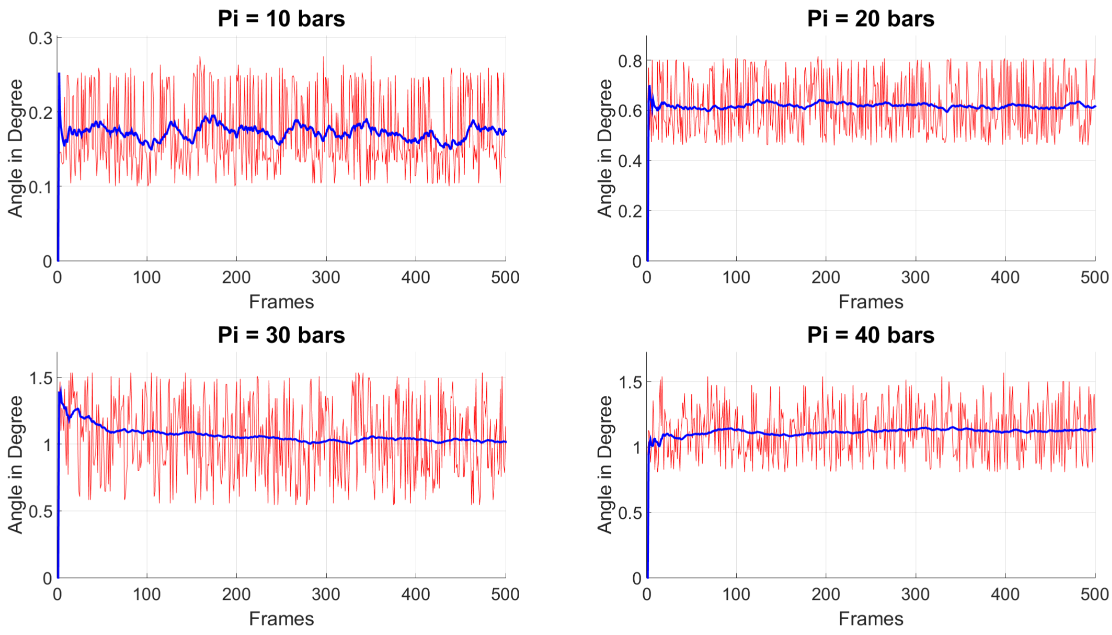


FIGURE 6.6: *Exp.2 Red:* Calculations *Blue:* Estimations (10 - 40 bars)

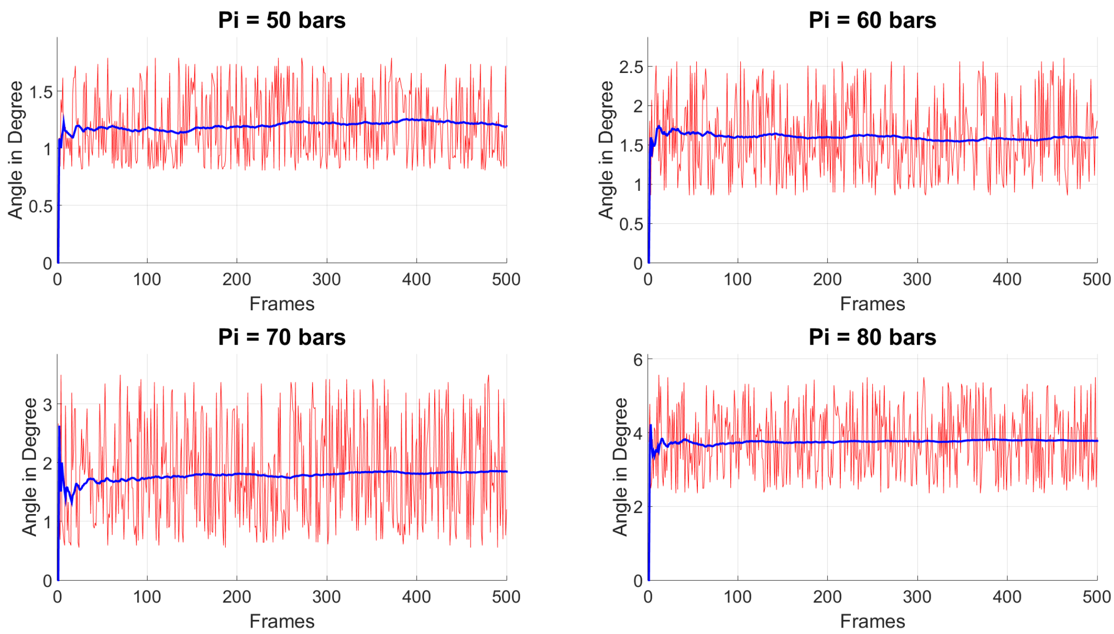


FIGURE 6.7: *Exp.2 Red:* Calculations *Blue:* Estimations (50 - 80 bars)

Note that although angle measurements from individual frames are quite fluctuating (in red), the estimated angles (in blue) by Kalman filter are very smooth due to the nature of the filter which combines predictions from a model that describes

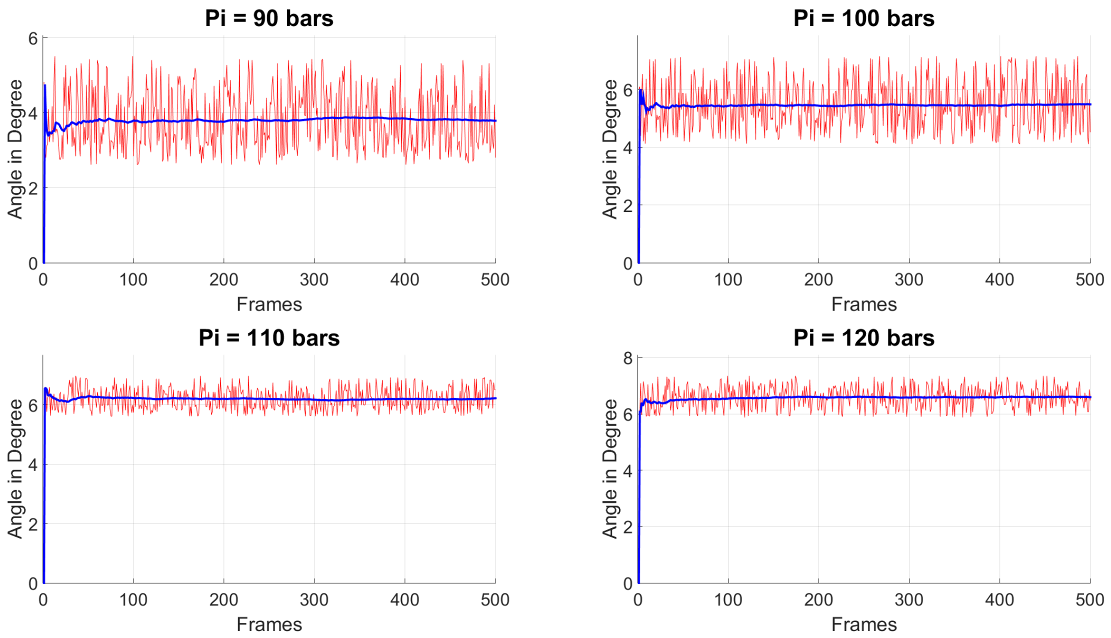


FIGURE 6.8: *Exp.2 Red:* Calculations *Blue:* Estimations (90 - 120 bars)

evolution of the cone angle and angle measurements computed from new frames. As it can be seen from these figures, new measurements are highly noisy. Kalman filter smoothes out these noisy measurements and generates optimal estimates that are much more meaningful. The average of angles estimated by Kalman filter at different pressure levels are then computed and plotted in Figure 6.9. This figure clearly shows that the cone angle gets larger by increasing inlet pressure values.

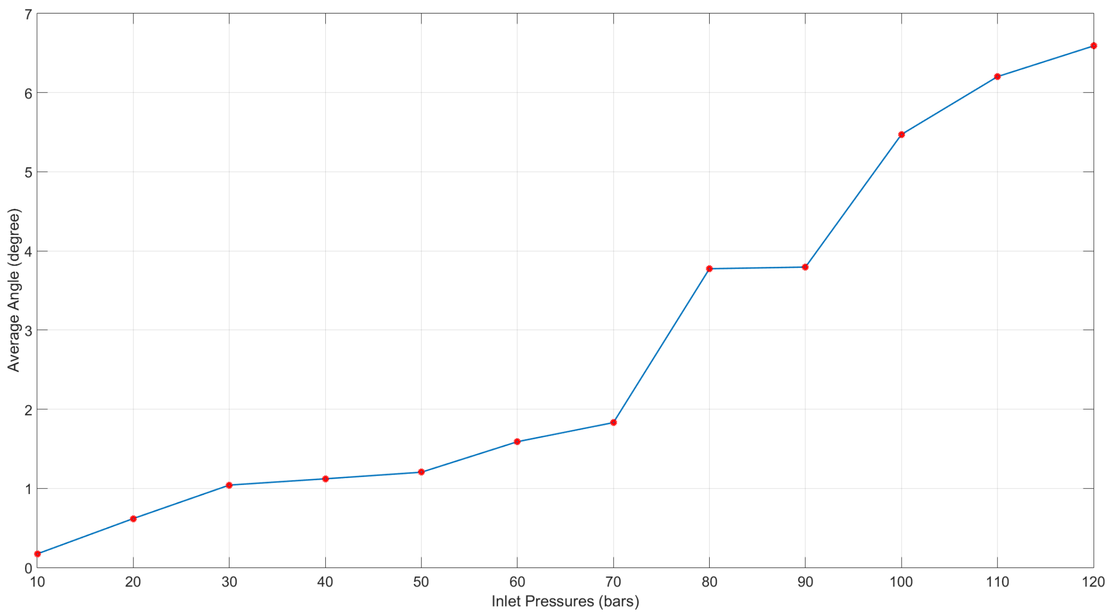


FIGURE 6.9: *Exp.2* Estimated angles through 10 to 120 bar inlet pressures

## 6.2 Scattered Bubbles Modeling

Distribution results of scattered bubbles (Figure 3.24) show that scattered bubble population is increased with the increasing inlet pressure.

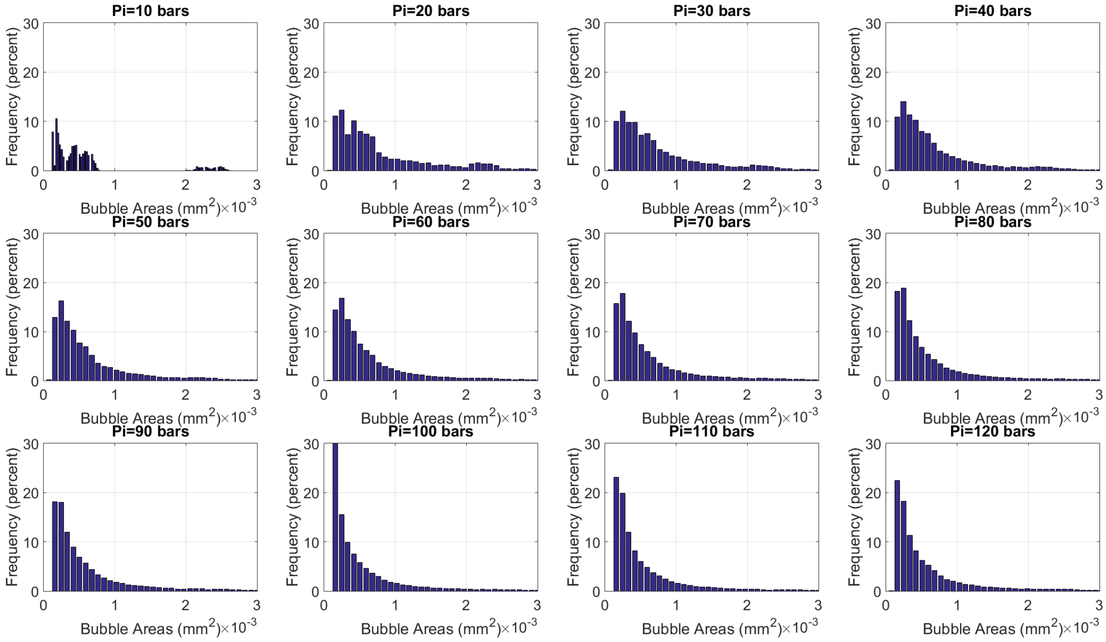


FIGURE 6.10: (a) Unprocessed original image (b) Contrast adjusted image

These distributions form two-peak Gaussian distributions (Figure 6.11). Each peak is investigated separately by a covariance matrix of distributed bubble positions. During experiments with inlet pressures between 10 bars to 120 bars, detected bubble areas vary from 30 $\mu$m to 2 mm (Figure 6.10).

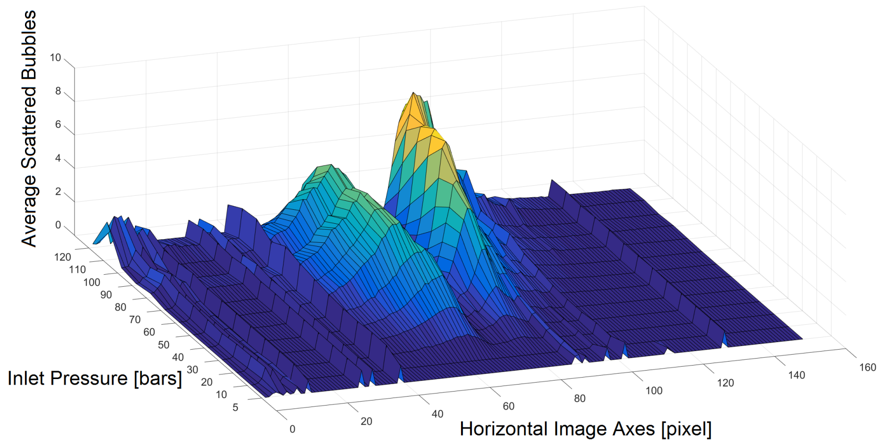


FIGURE 6.11: (a) Unprocessed original image (b) Contrast adjusted image

| Inlet Pressure *(bar)* | Major Semi-Axes **Left** *(mm)* | Major Semi-Axes **Right** *(mm)* | Minor Semi-Axes **Left** *(mm)* | Minor Semi-Axes **Right** *(mm)* |
|---|---|---|---|---|
| 10 | 1.9430 | 1.1114 | 0.3593 | 0.1858 |
| 20 | 1.6254 | 1.1174 | 0.6497 | 0.4076 |
| 30 | 1.4965 | 1.1947 | 0.5549 | 0.4339 |
| 40 | 1.4188 | 1.2654 | 0.4781 | 0.3747 |
| 50 | 1.3949 | 1.3383 | 0.4399 | 0.3616 |
| 60 | 1.3574 | 1.3464 | 0.4031 | 0.2945 |
| 70 | 1.3545 | 1.3610 | 0.4064 | 0.2909 |
| 80 | 1.3470 | 1.3600 | 0.4673 | 0.3243 |
| 90 | 1.3520 | 1.3953 | 0.4385 | 0.3484 |
| 100 | 1.3784 | 1.3633 | 0.4535 | 0.2575 |
| 110 | 1.3223 | 1.3969 | 0.5870 | 0.3168 |
| 120 | 1.3754 | 1.3575 | 0.5558 | 0.2888 |

TABLE 6.1: Major - Minor Axes Properties of Bubble Distributions

Semi-axes lengths of ellipses obtained from covariance matrices (Table 6.1) show that major axes lengths are more determinative than minor axes lengths, since they are along the motion of bubbles. When the left major semi-axes lengths increase, corresponding right ones decrease because of the oscillation of bubbly flow generator.

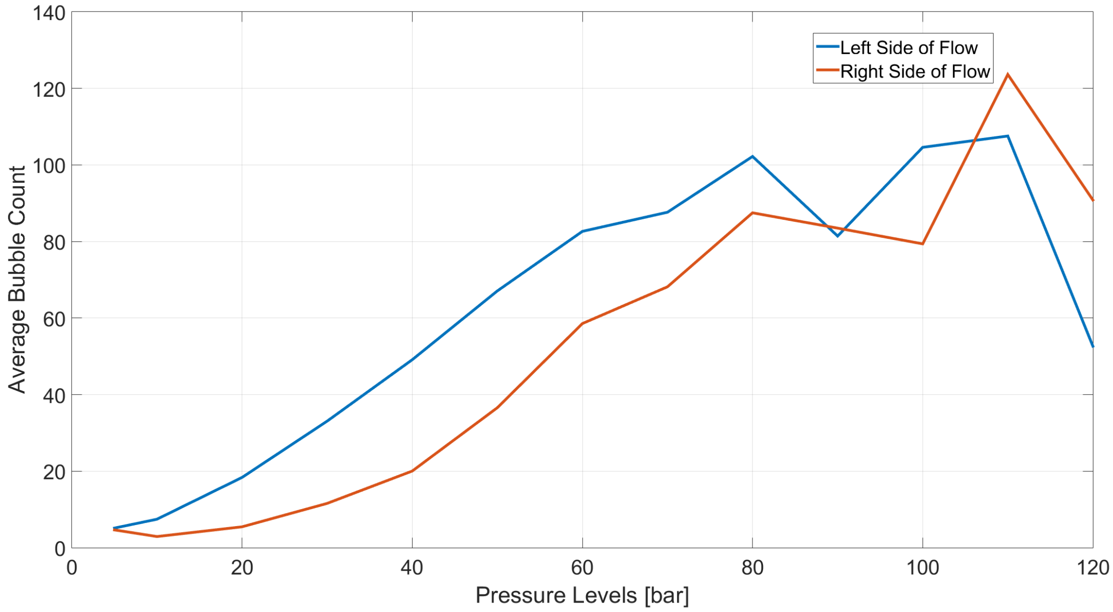


FIGURE 6.12: (a) Unprocessed original image (b) Contrast adjusted image

In general, major axes lengths can be considered as decreasing on the average, which shows that more stationary clusters are generated around main flow. Additionally, after a certain pressure level ($Pi > 50$), major and minor axes lengths do not change dramatically. Scattered bubbles are distributed around main flow in the same way but amount of bubbles are increasing (Fig.6.12).

## 6.3 Visual Tracking of Single, Double and Triple Cavitation Bubbles

Individually distinguished bubble images are obtained in **Experiment 2** as mentioned in Section 3. Bubbles are detected after 11 mm from the orifice of cavitation generator with low inlet pressure less than 10 bars.

Proposed structural and motion characteristics based tracking performs pretty good since minimum Bhattacharyya distances shown in results are around 0.001. Although one pair of bubbles alter its shape dramatically in example 6.3.13, bubbles are still tracked as a group, which shows the validity of mass/volume conservation assumption. In this context, two individually tracked bubbles examples (6.3.13, 6.3.14) demonstrate the same thinness ratio pattern despite circumference and area changes are completely different.

Mass/volume conservation assumption also enables tracker to handle the occasions of merging and splitting of bubbles. Merging examples (6.3.5, 6.3.6 and 6.3.7) show that bubbles lose slow down during the merging period and after that accelerate to reach the former speed level. Slowing down impact is also valid for attached movement without merging. Sticking example (6.3.8) shows that congregation decreases the overall speed but less than merging case.

Differently, splitting examples (6.3.9, 6.3.10 and 6.3.11) demonstrate that bubbles gather pace during the splitting period. Example 6.3.12 shows the impacts of splitting and merging on the speed of bubbles when they occur consecutively.

### 6.3.1 Single Tracking Example - 1

- Single bubble with approximately 496 $\mu$m diameter changes both its orientation and morphology. (Starting frame no: 67)

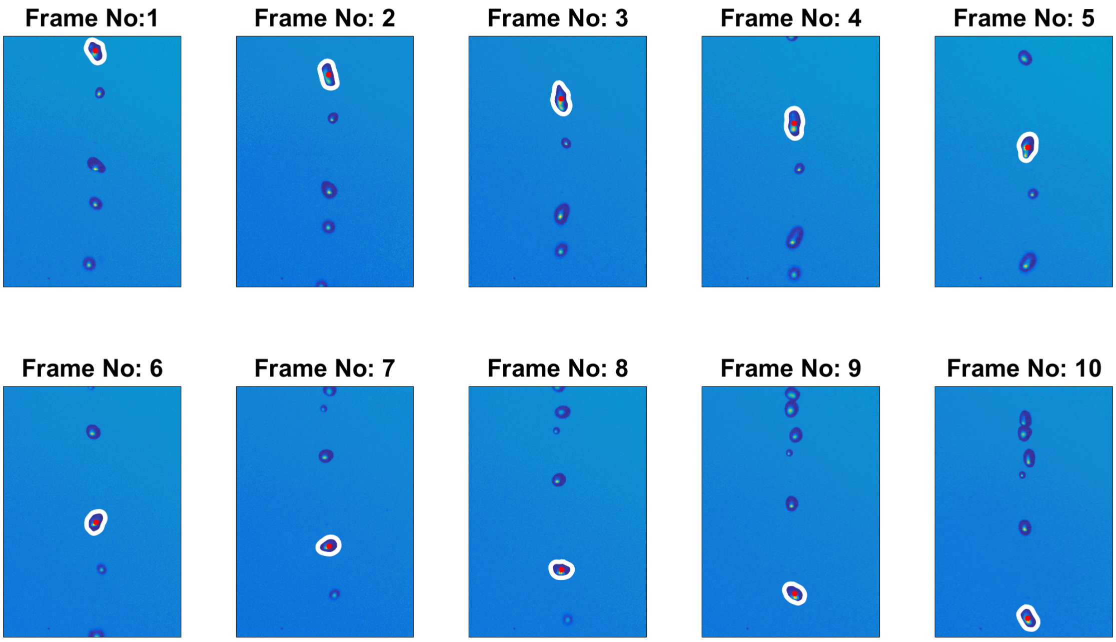


FIGURE 6.13: Bubble Tracking

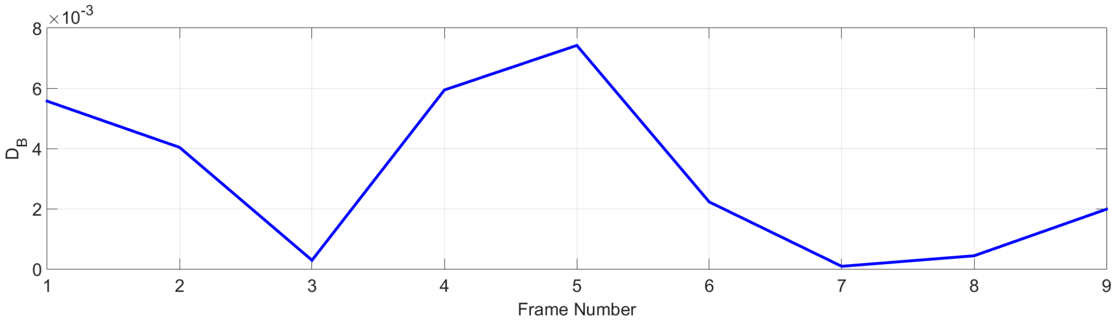


FIGURE 6.14: Minimum Bhattacharyya distances during the motion

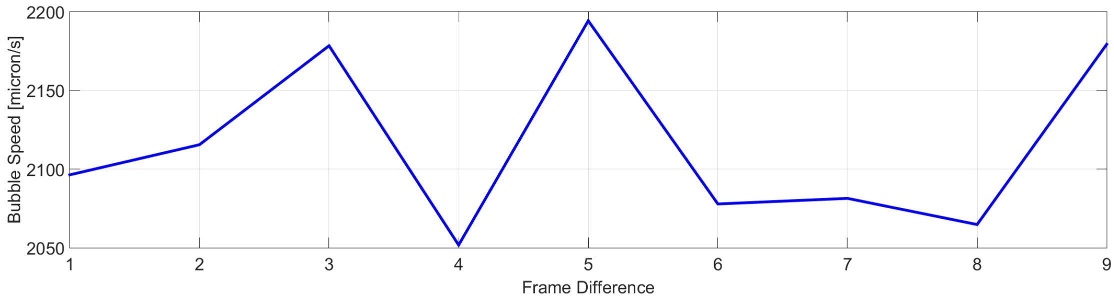


FIGURE 6.15: Speed of tracked bubbles

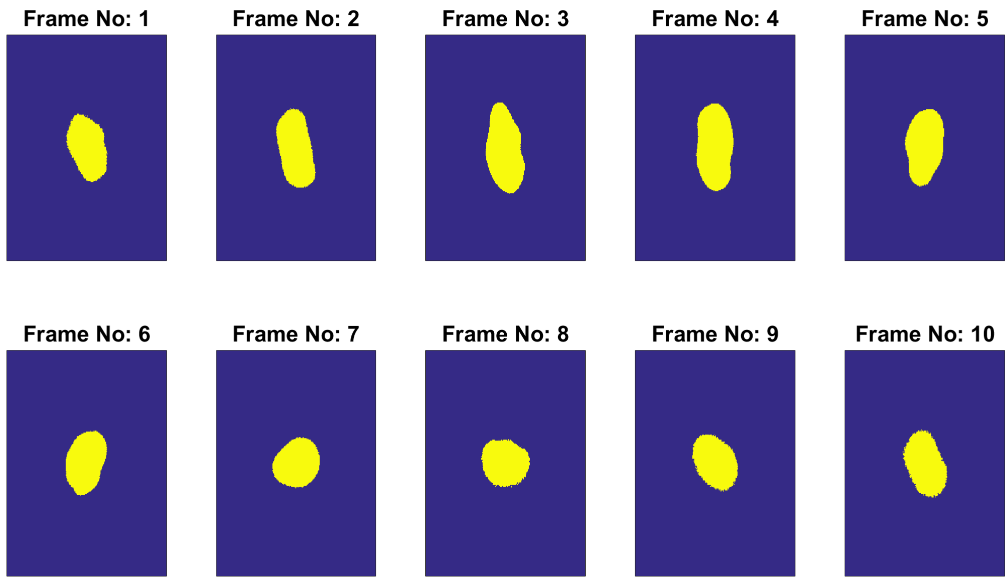


FIGURE 6.16: Silhouettes of tracked bubbles

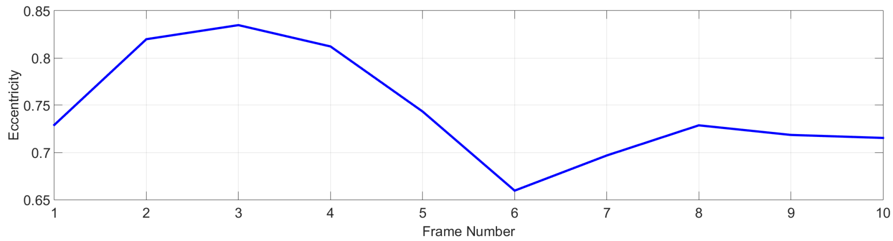


FIGURE 6.17: Eccentricity changes during the motion

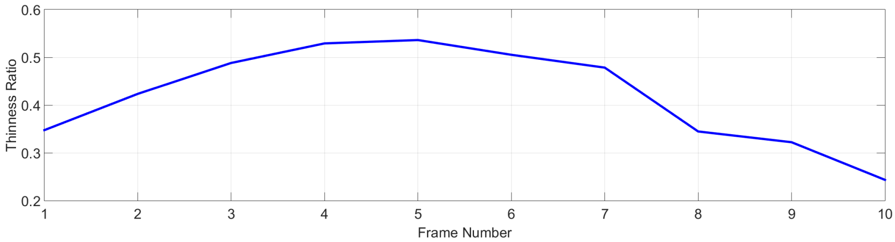


FIGURE 6.18: Thinness ratio changes during the motion

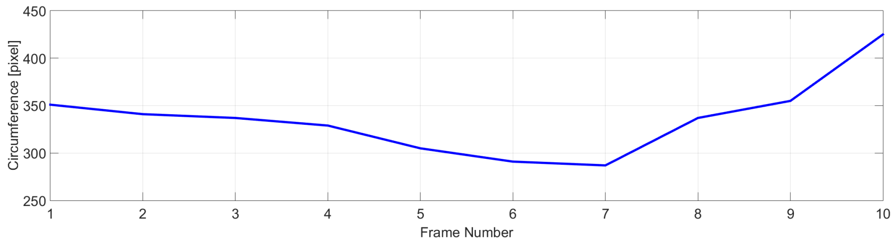


FIGURE 6.19: Circumference changes during the motion

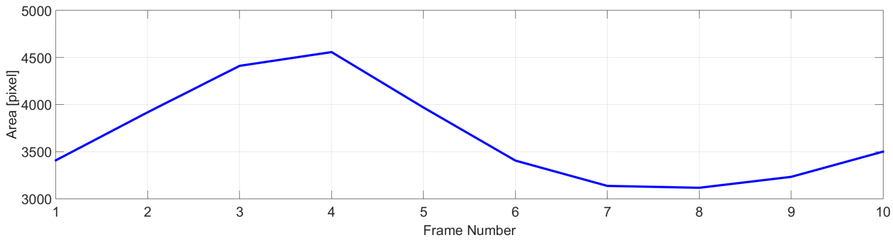


FIGURE 6.20: Area changes during the motion

### 6.3.2 Single Tracking Example - 2

- Single bubble with approximately 397 $\mu$m diameter is just changing its rotation and elliptic shape is conserved. (Starting frame no: 35)

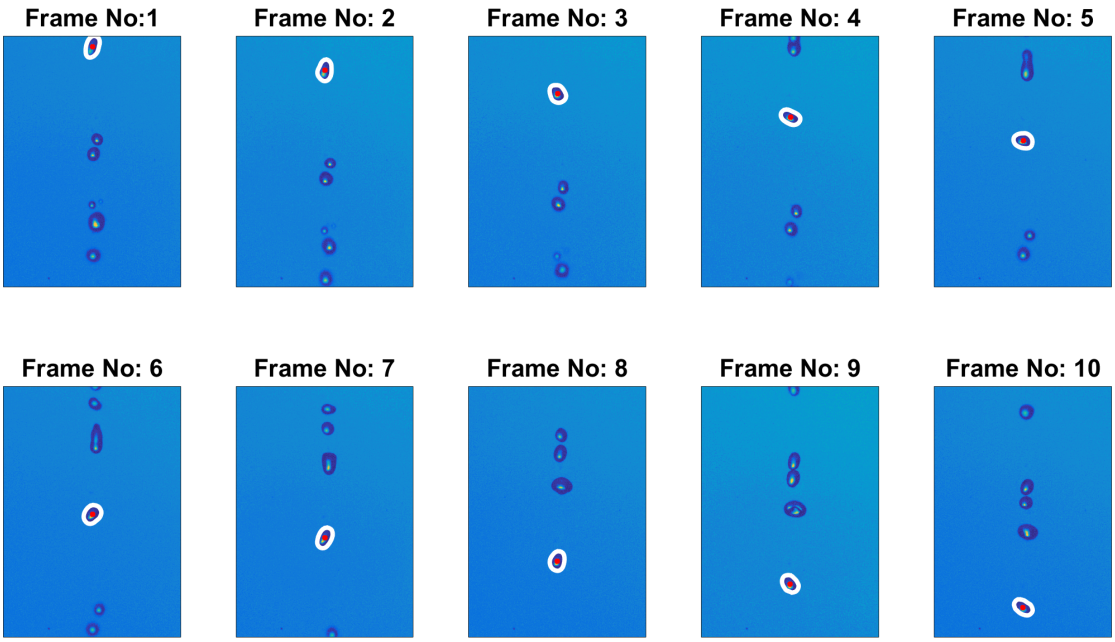


FIGURE 6.21: Bubble Tracking

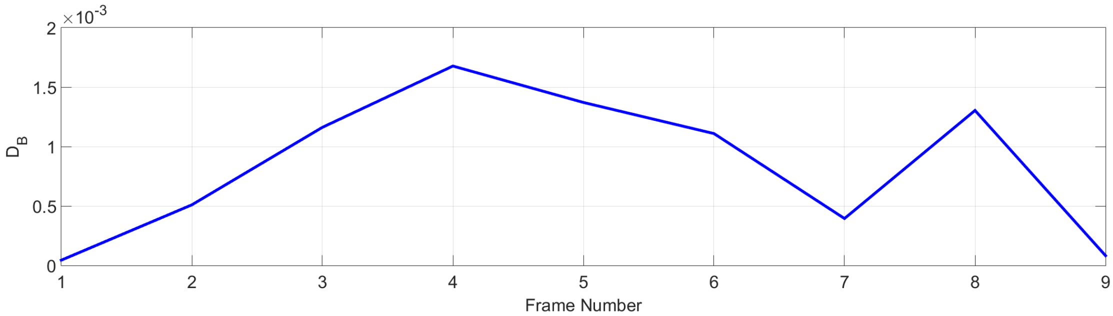


FIGURE 6.22: Minimum Bhattacharyya distances during the motion

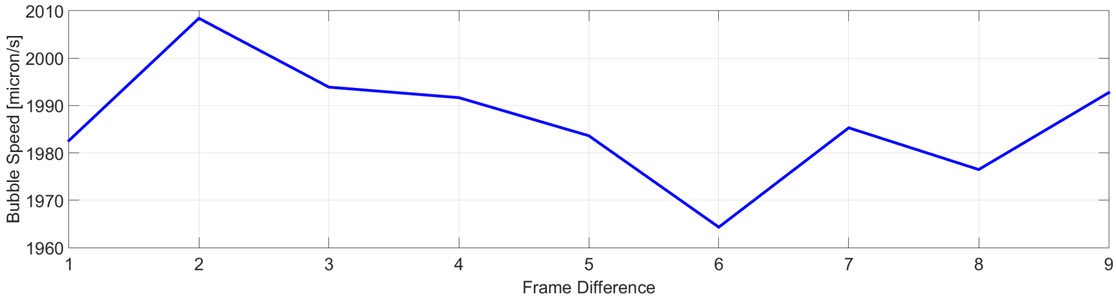


FIGURE 6.23: Speed of tracked bubbles

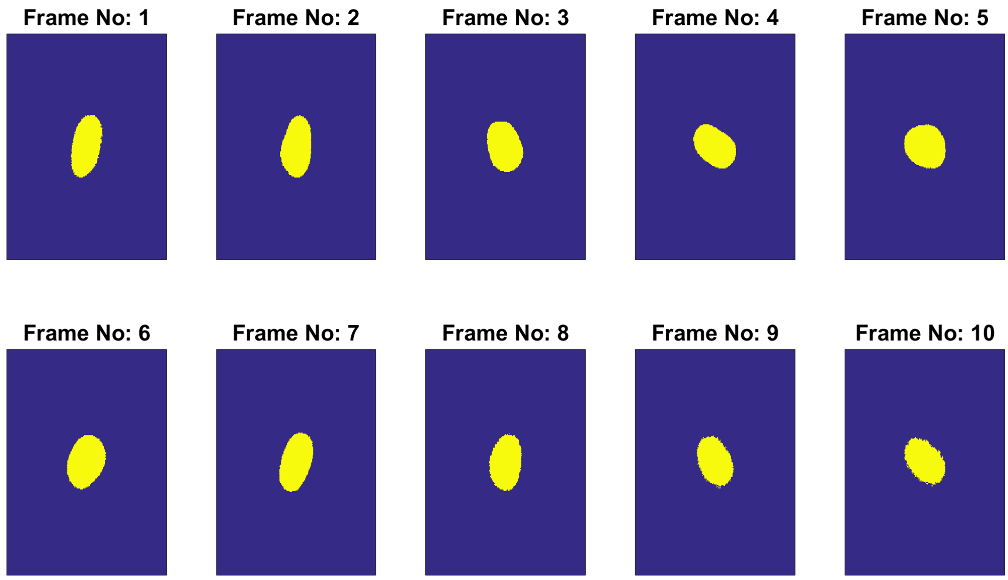


FIGURE 6.24: Silhouettes of tracked bubbles

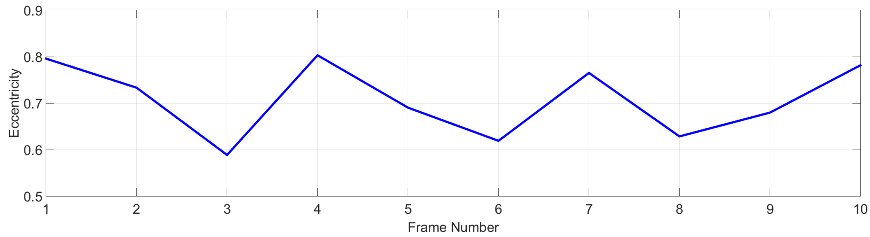


FIGURE 6.25: Eccentricity changes during the motion

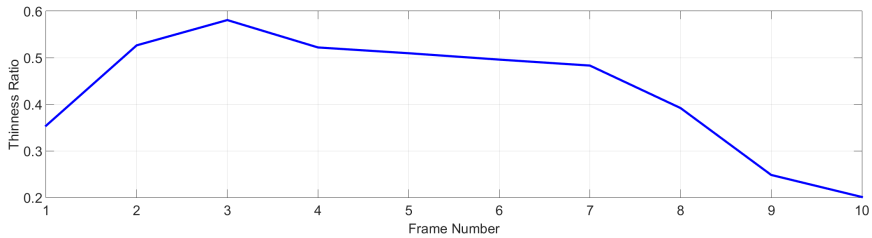


FIGURE 6.26: Thinness ratio changes during the motion

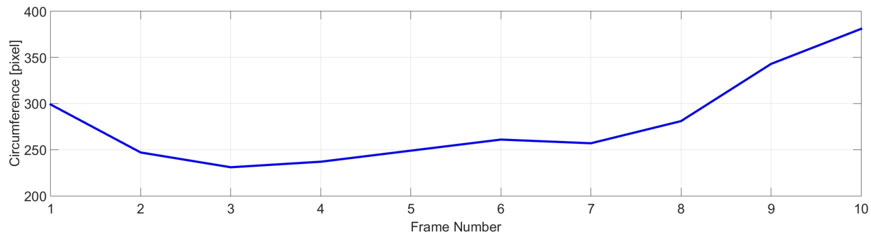


FIGURE 6.27: Circumference changes during the motion

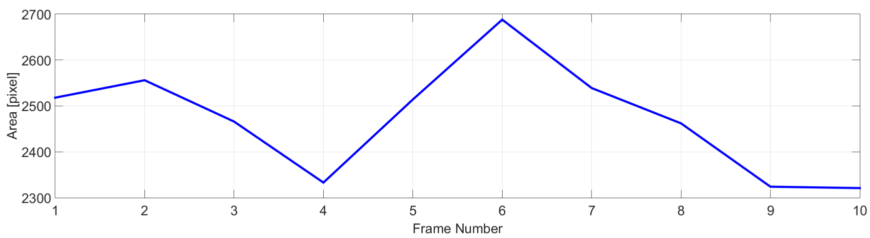


FIGURE 6.28: Area changes during the motion

### 6.3.3 Single Tracking Example - 3

- Single bubble with approximately 351 $\mu$m diameter does not change the orientation much but the shape is changed dramatically during the flow. (Starting frame no: 39)

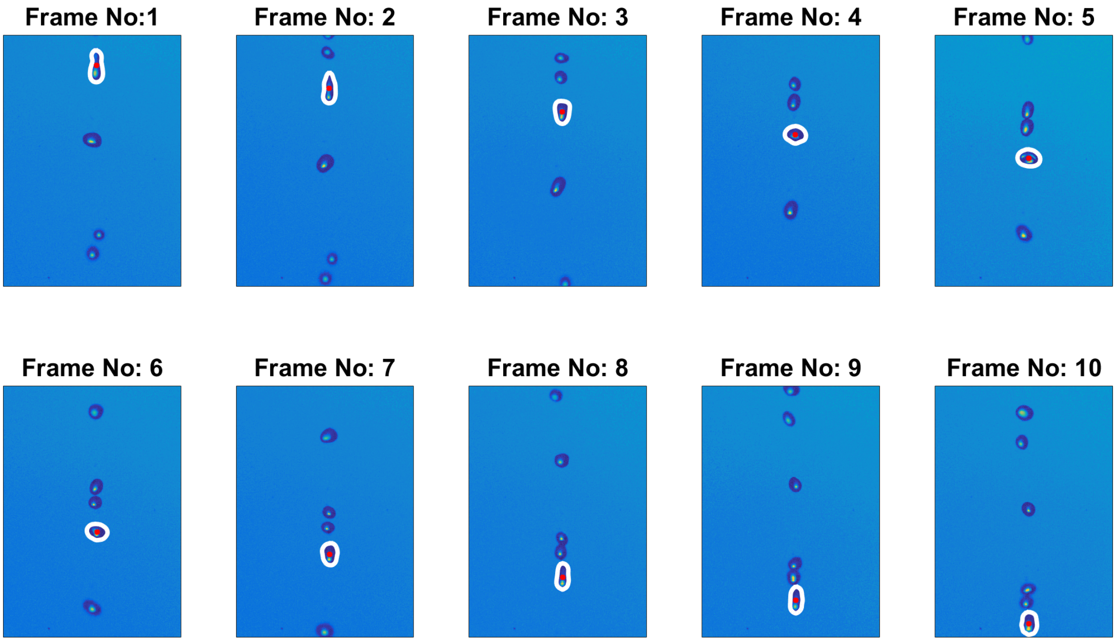


FIGURE 6.29: Bubble Tracking

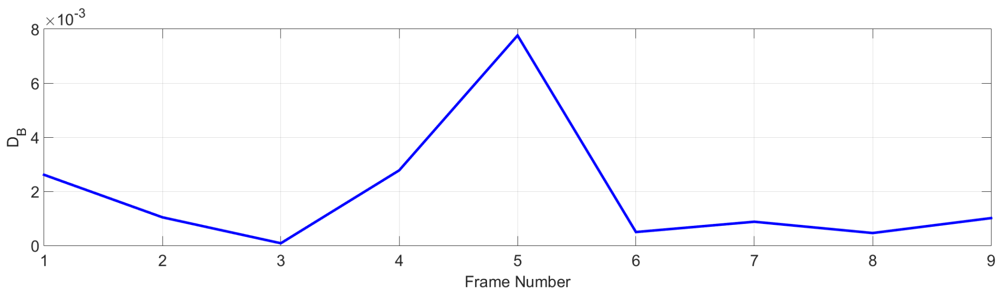


FIGURE 6.30: Minimum Bhattacharyya distances during the motion

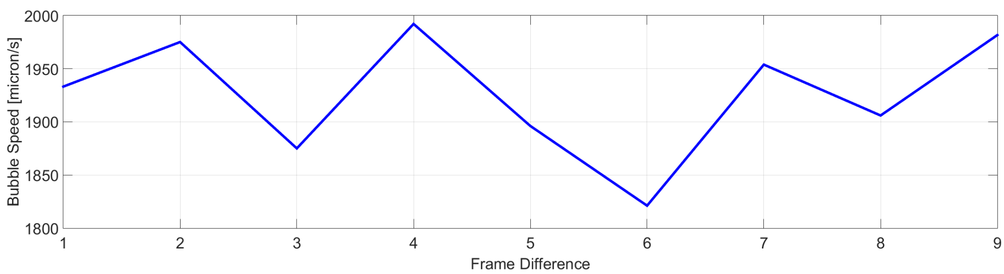


FIGURE 6.31: Speed of tracked bubbles

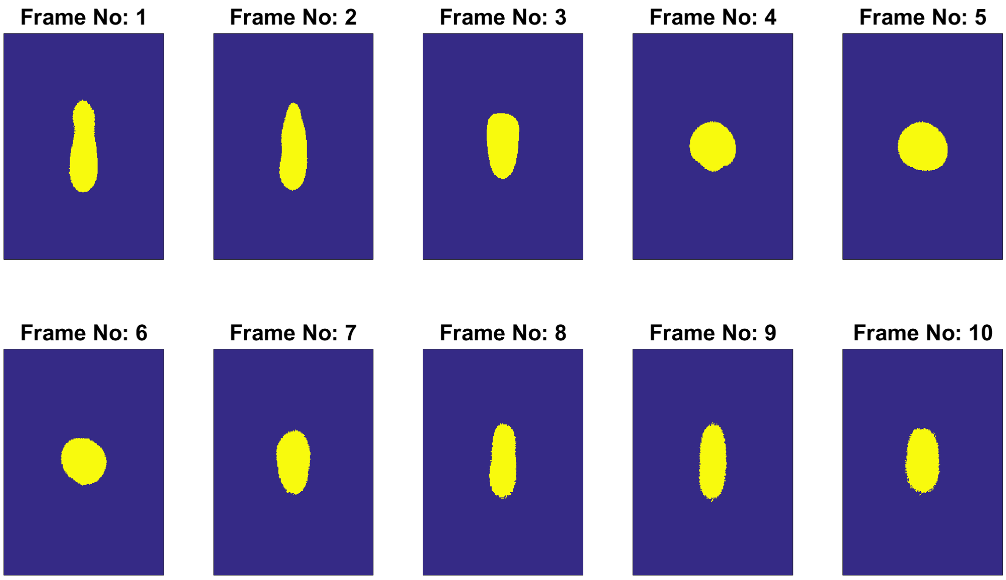


FIGURE 6.32: Silhouettes of tracked bubbles

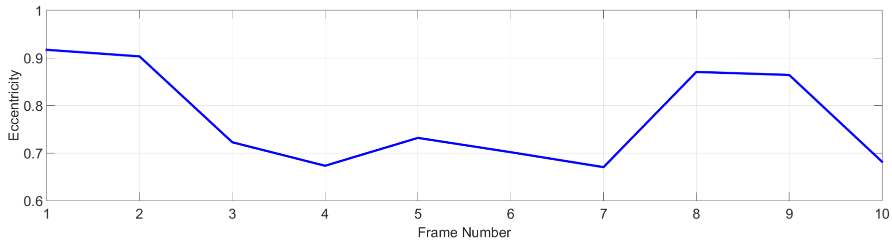


FIGURE 6.33: Eccentricity changes during the motion

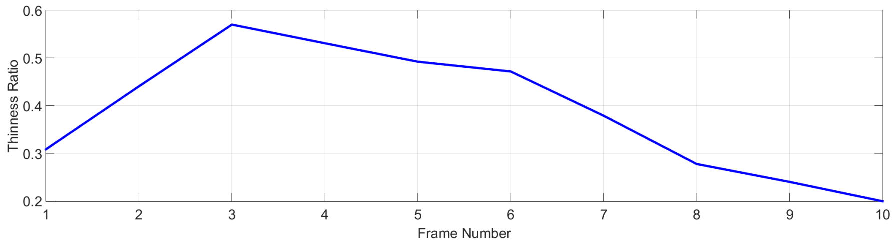


FIGURE 6.34: Thinness ratio changes during the motion

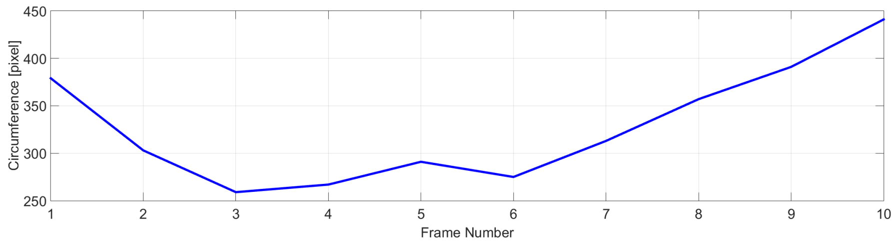


FIGURE 6.35: Circumference changes during the motion

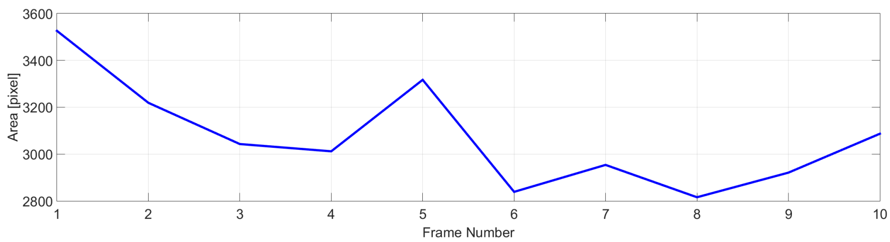


FIGURE 6.36: Area changes during the motion

### 6.3.4 Single Tracking Example - 4

- Single bubble with approximately 496 $\mu$m diameter moves through the flow smoothly and don't alter its shape very much. (Starting frame no: 250)

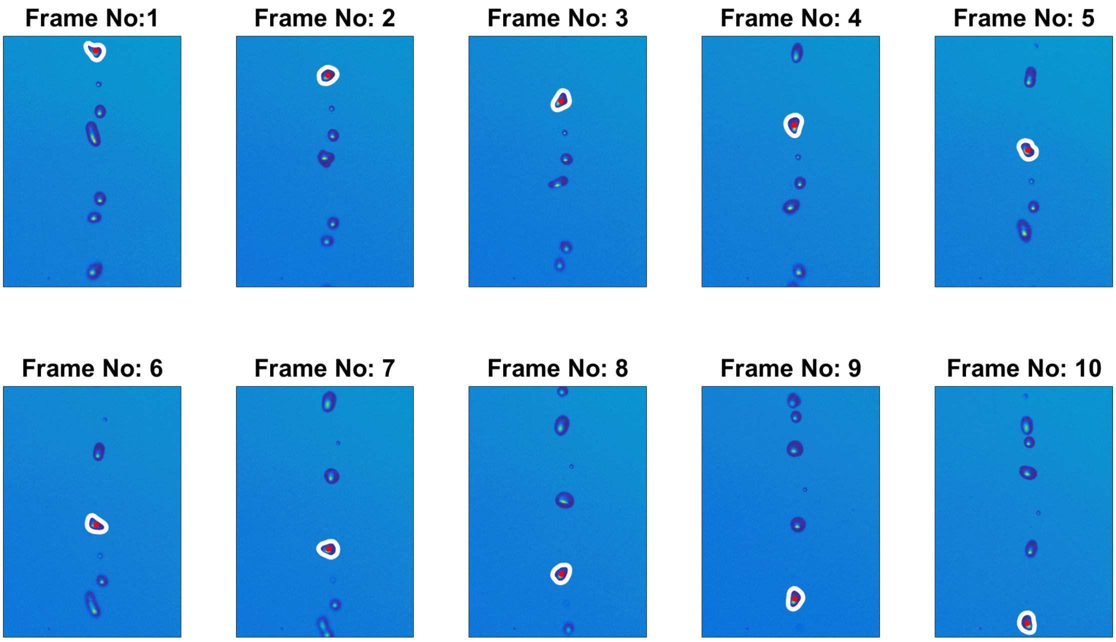


FIGURE 6.37: Bubble Tracking

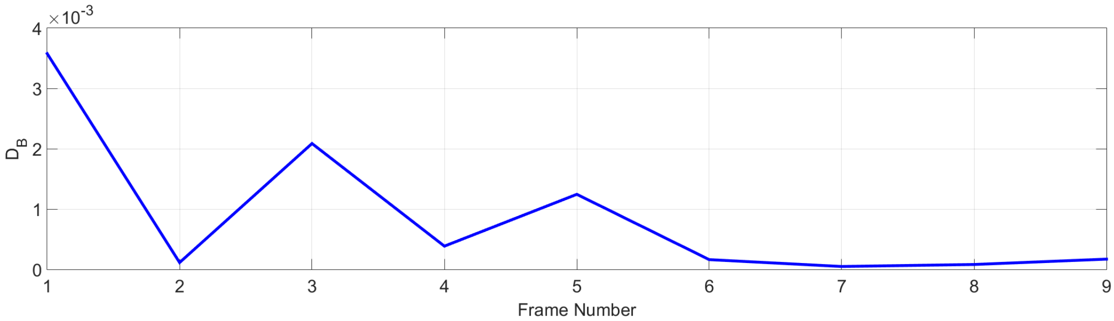


FIGURE 6.38: Minimum Bhattacharyya distances during the motion

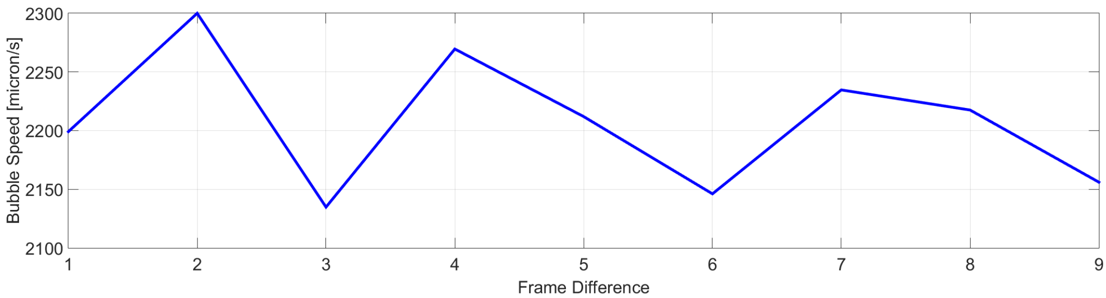


FIGURE 6.39: Speed of tracked bubbles

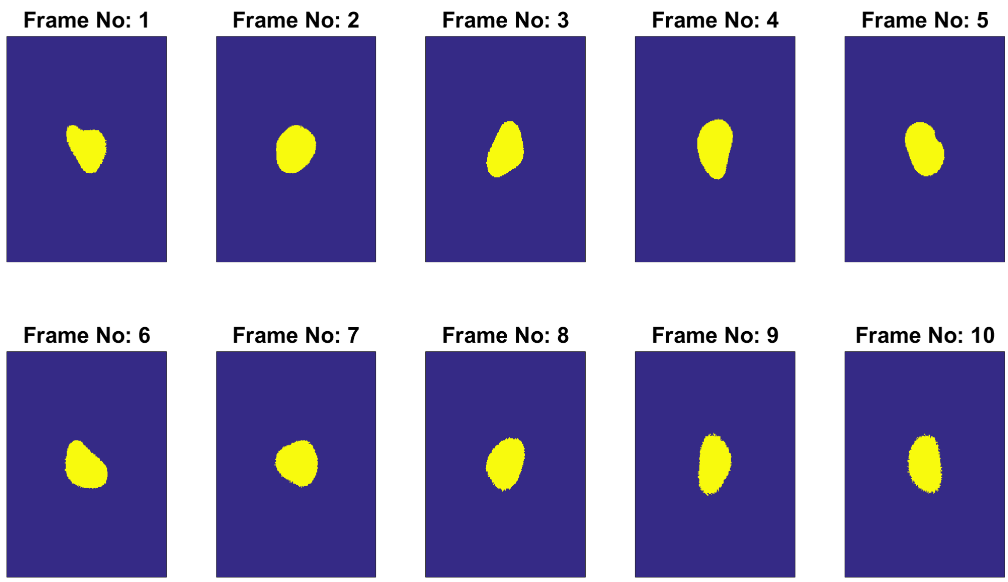


FIGURE 6.40: Silhouettes of tracked bubbles

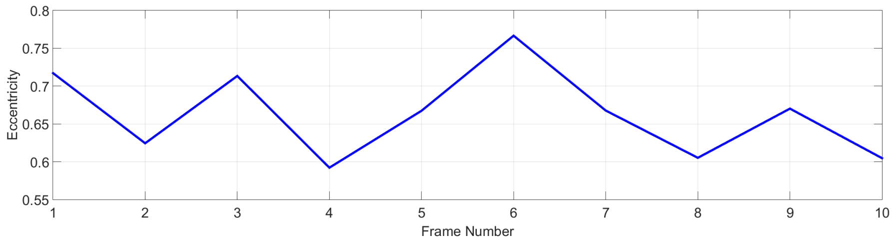


FIGURE 6.41: Eccentricity changes during the motion

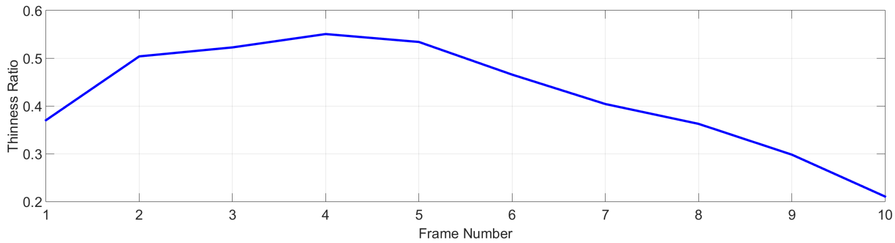


FIGURE 6.42: Thinness ratio changes during the motion

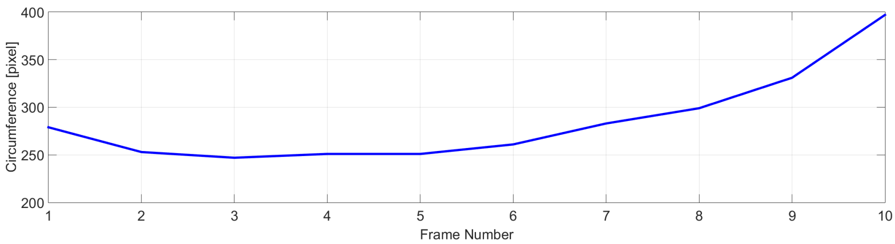


FIGURE 6.43: Circumference changes during the motion

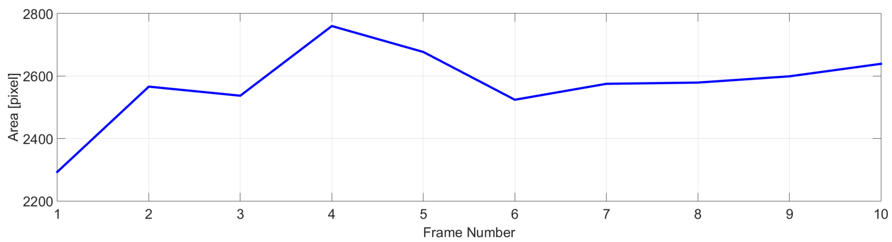


FIGURE 6.44: Area changes during the motion

### 6.3.5 Merging Example - 1

- Two individual bubbles with approximately 465 $\mu$m and 175 $\mu$m diameter merge to form a single bubble. (Starting frame no: 14)

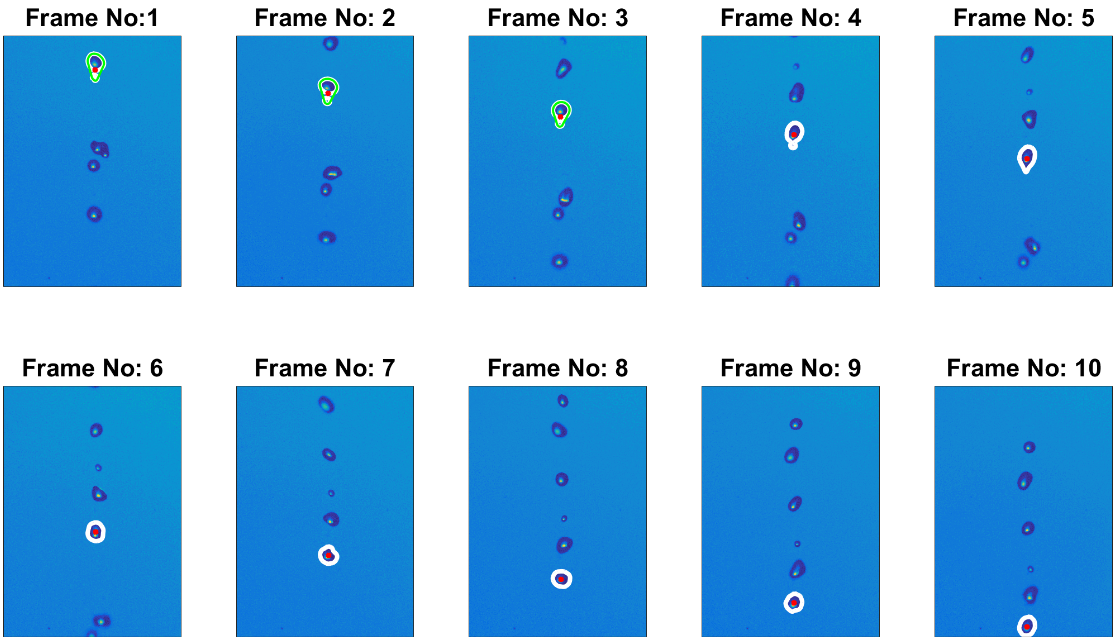


FIGURE 6.45: Bubble Tracking

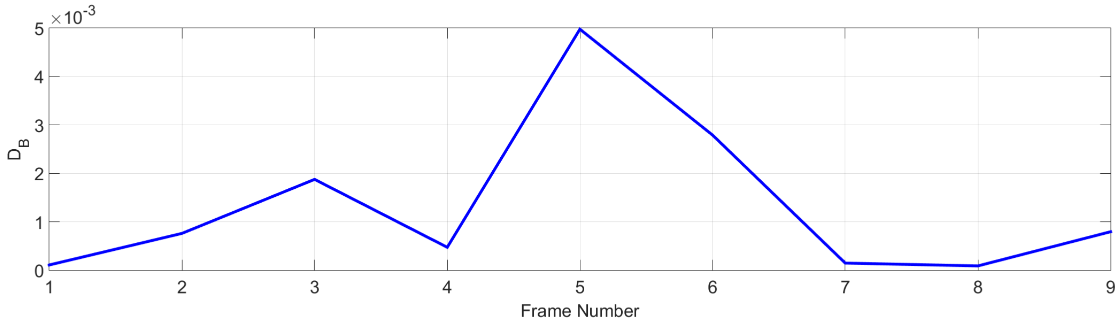


FIGURE 6.46: Minimum Bhattacharyya distances during the motion

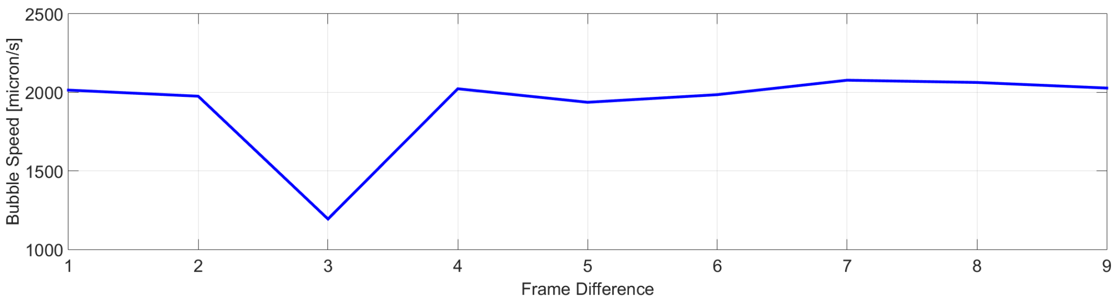


FIGURE 6.47: Speed of tracked bubbles

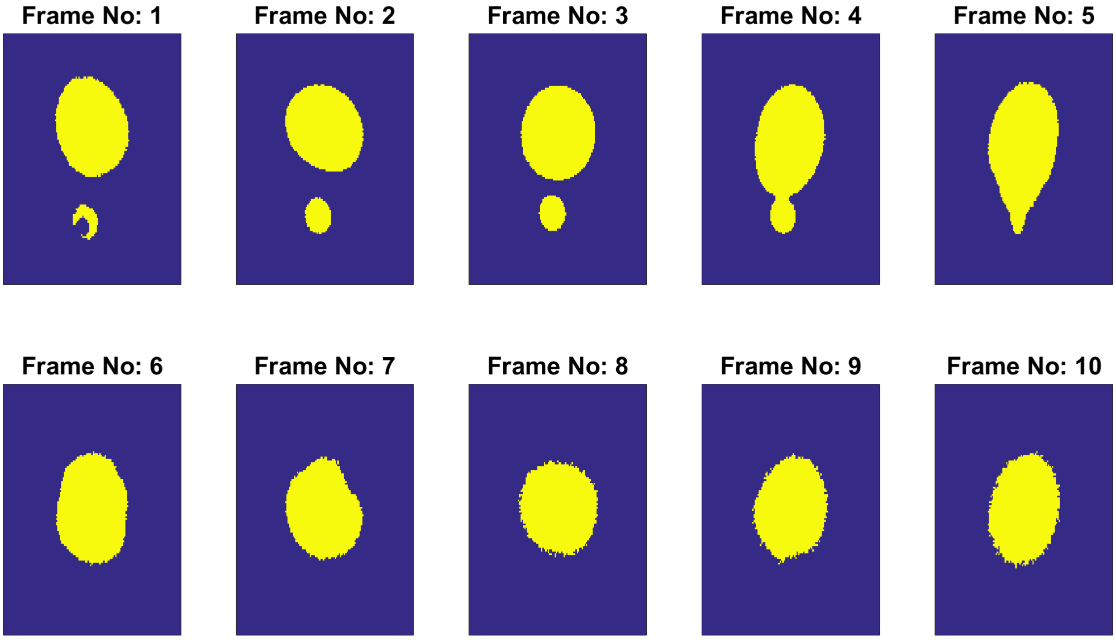


FIGURE 6.48: Silhouettes of tracked bubbles

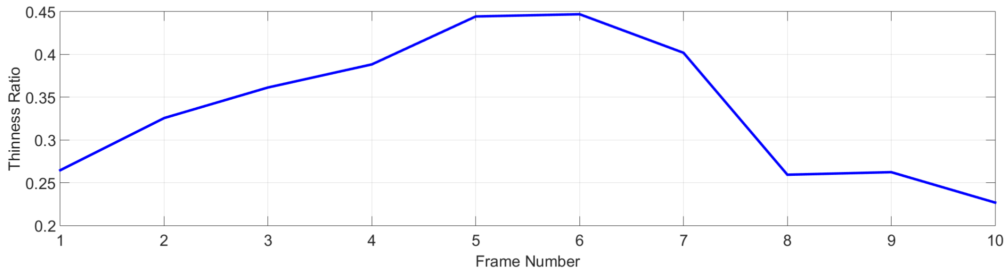


FIGURE 6.49: Thinness ratio changes during the motion

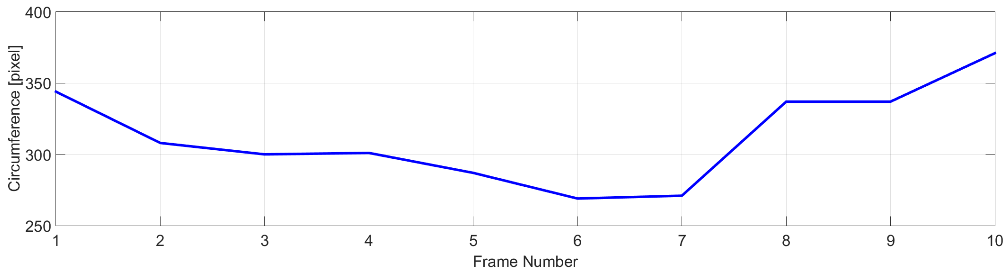


FIGURE 6.50: Circumference changes during the motion

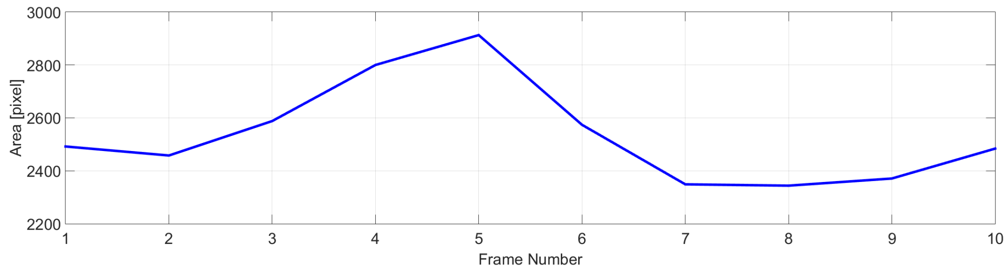


FIGURE 6.51: Area changes during the motion

### 6.3.6 Merging Example - 2

- Two individual bubbles with approximately 457 $\mu$m and 343 $\mu$m diameter merge to form a single bubble. (Starting frame no: 437)

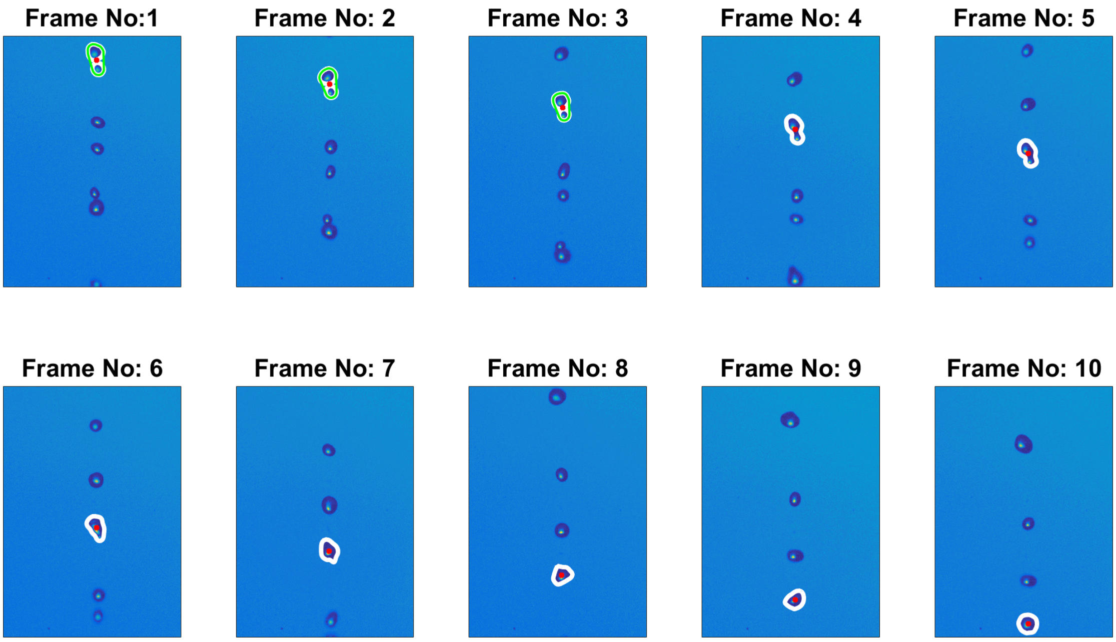


FIGURE 6.52: Bubble Tracking

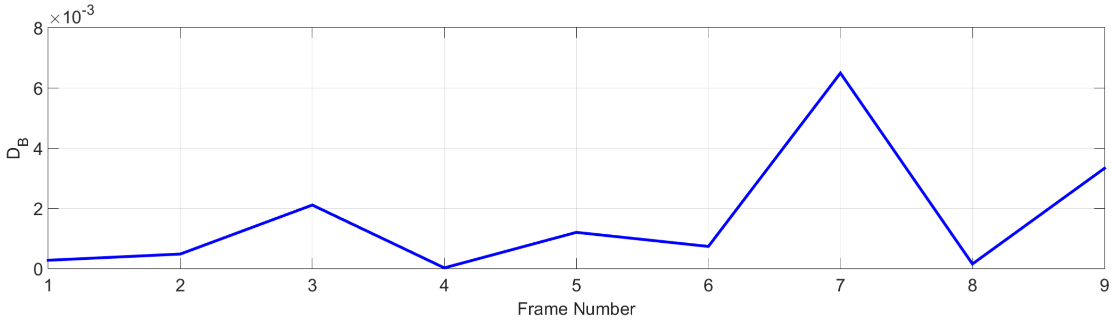


FIGURE 6.53: Minimum Bhattacharyya distances during the motion

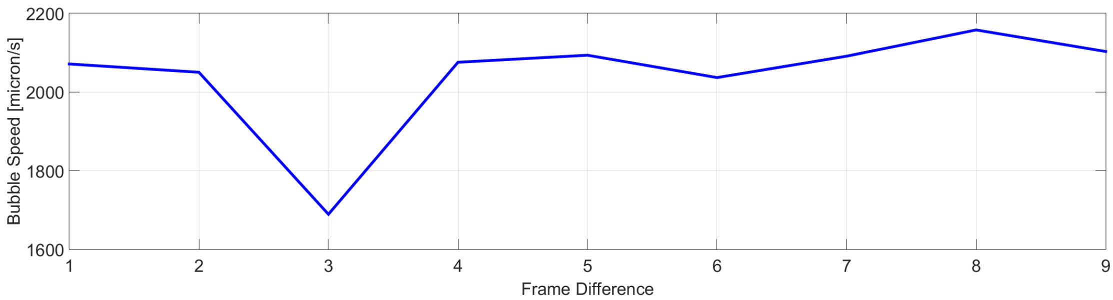


FIGURE 6.54: Speed of tracked bubbles

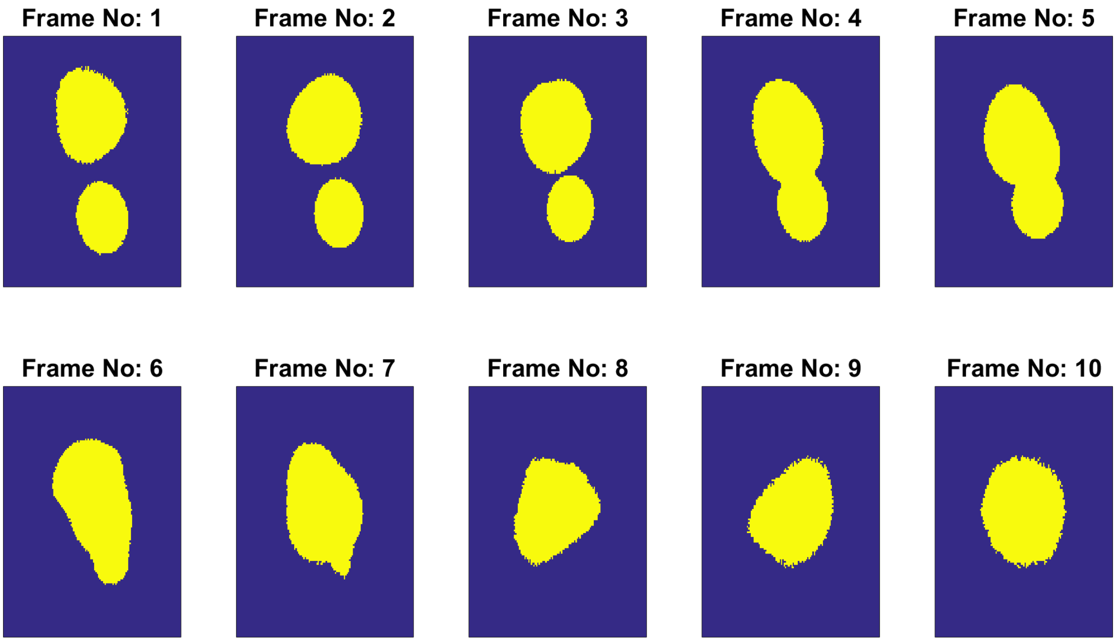


FIGURE 6.55: Silhouettes of tracked bubbles

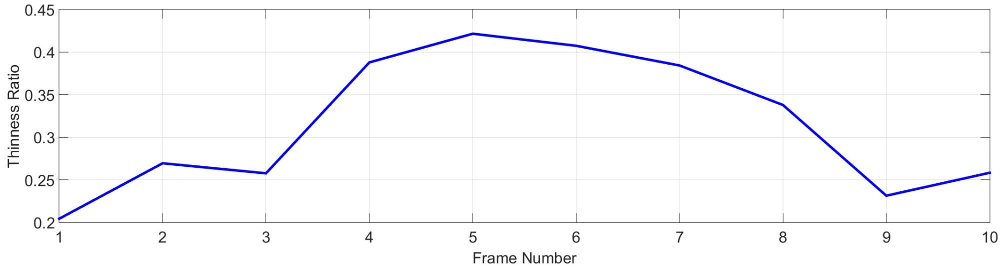


FIGURE 6.56: Thinness ratio changes during the motion

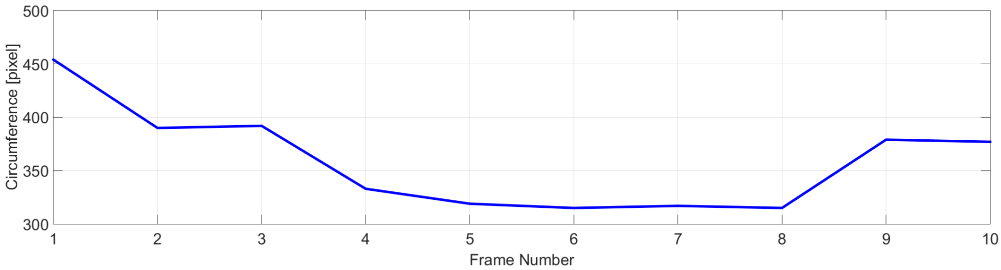


FIGURE 6.57: Circumference changes during the motion

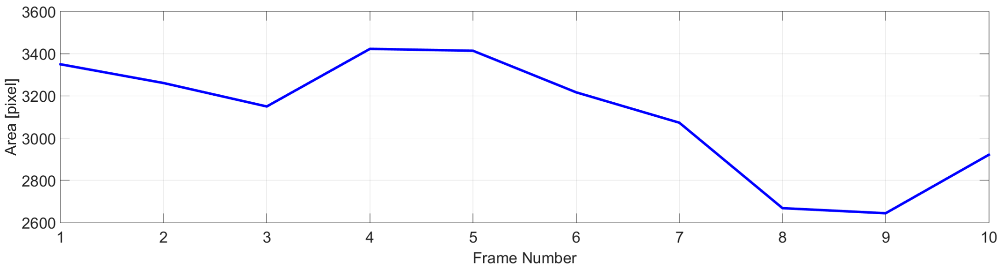


FIGURE 6.58: Area changes during the motion

### 6.3.7 Merging Example - 3

- Three individual bubbles with approximately 389 $\mu$m, 427 $\mu$m and 412 $\mu$m diameter merge to form a single bubble. (Starting frame no: 457)

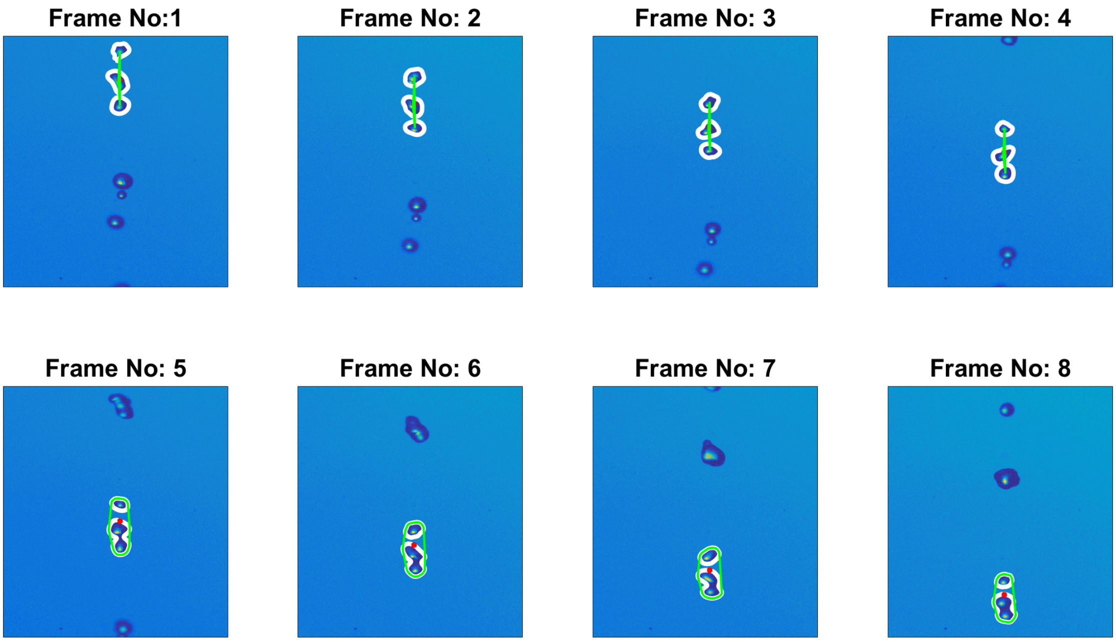


FIGURE 6.59: Bubble Tracking

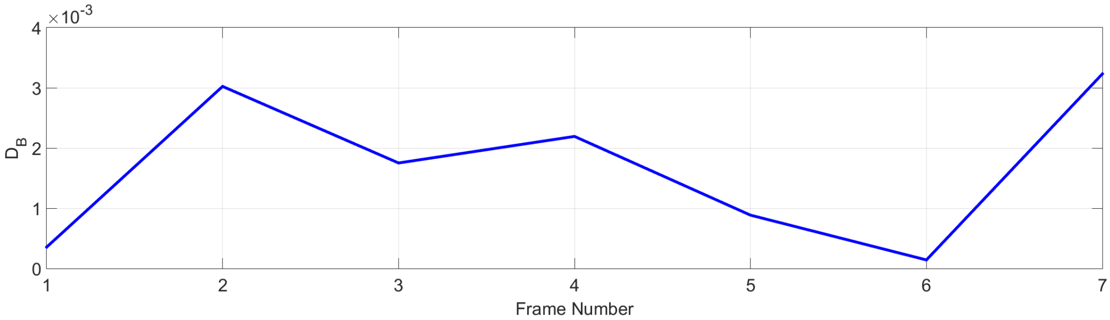


FIGURE 6.60: Minimum Bhattacharyya distances during the motion

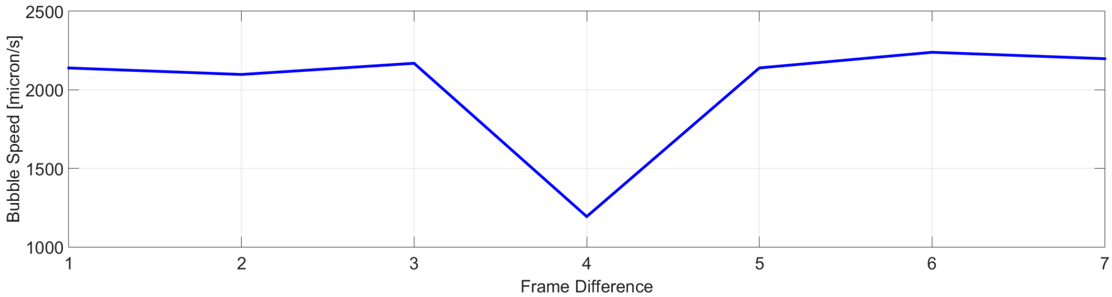


FIGURE 6.61: Speed of tracked bubbles

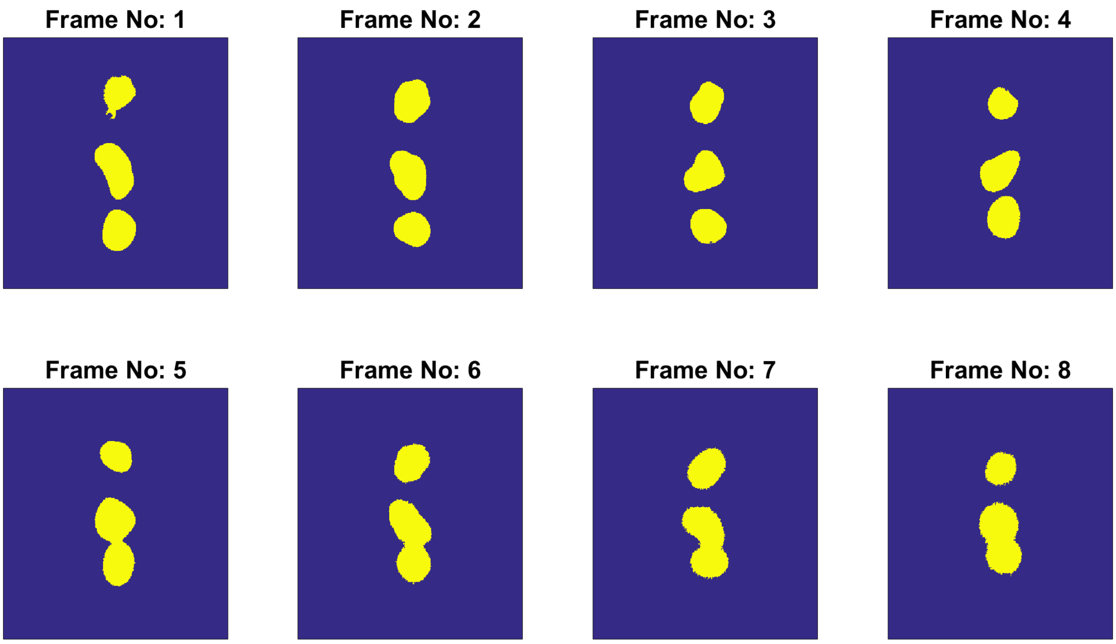


FIGURE 6.62: Silhouettes of tracked bubbles

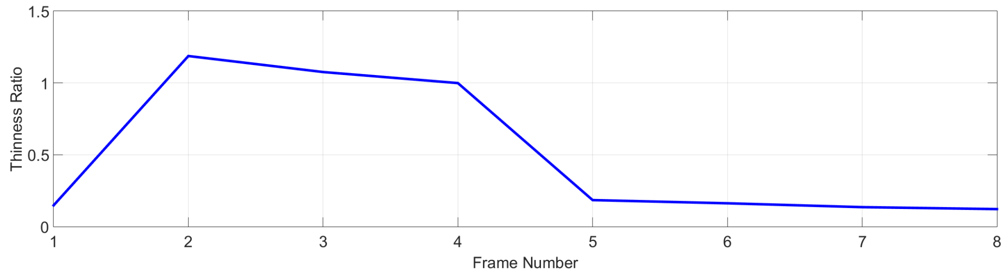


FIGURE 6.63: Thinness ratio changes during the motion

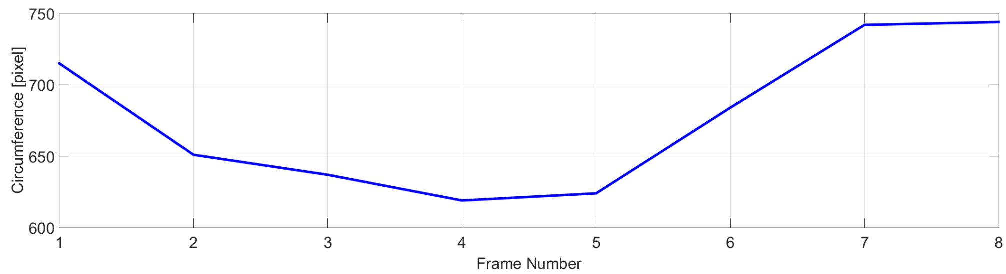


FIGURE 6.64: Circumference changes during the motion

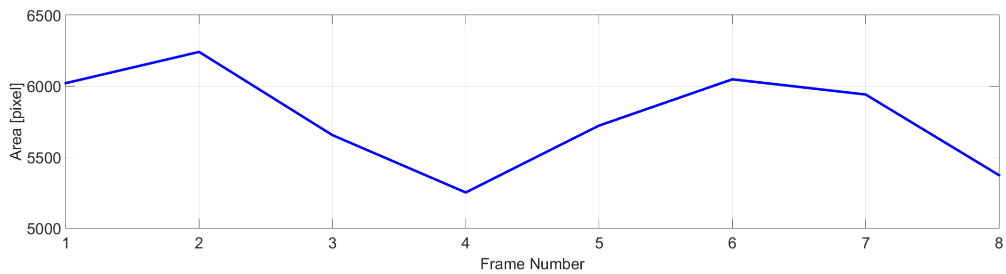


FIGURE 6.65: Area changes during the motion

### 6.3.8 Sticking Example

- Two individual bubbles with approximately 412 $\mu$m and 358 $\mu$m diameter stick and move together without merging. (Starting frame no: 55)

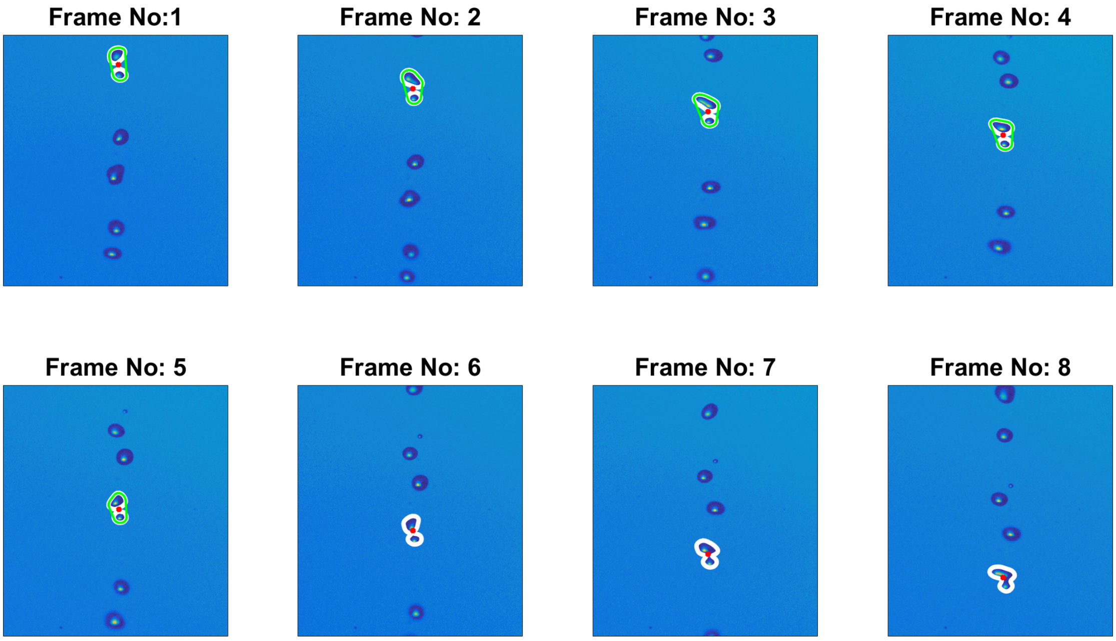


FIGURE 6.66: Bubble Tracking

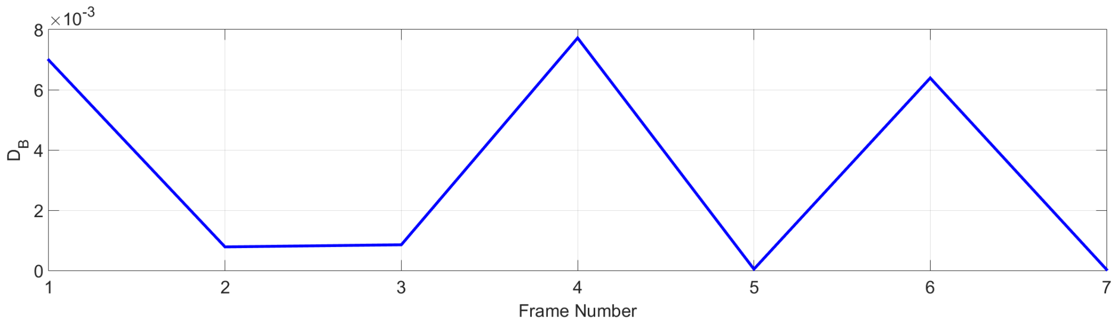


FIGURE 6.67: Minimum Bhattacharyya distances during the motion

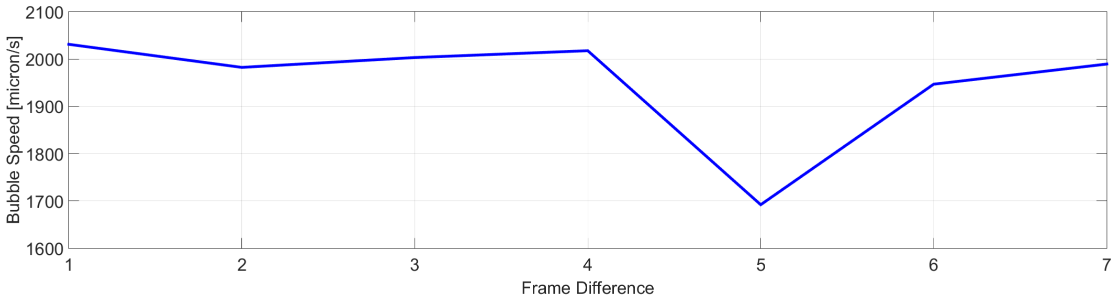


FIGURE 6.68: Speed of tracked bubbles

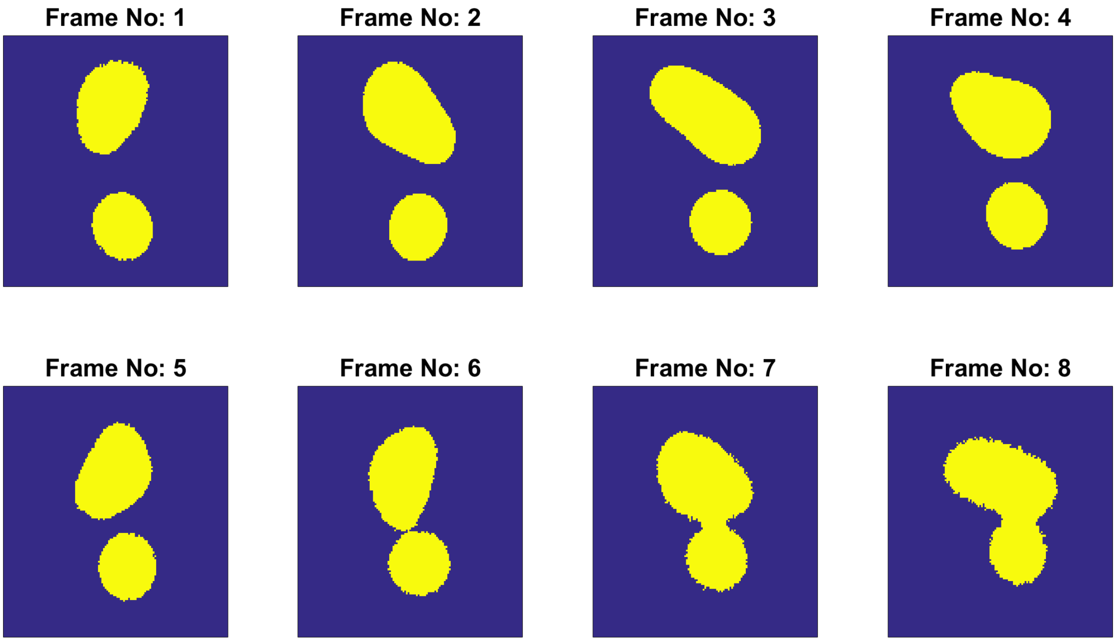


FIGURE 6.69: Silhouettes of tracked bubbles

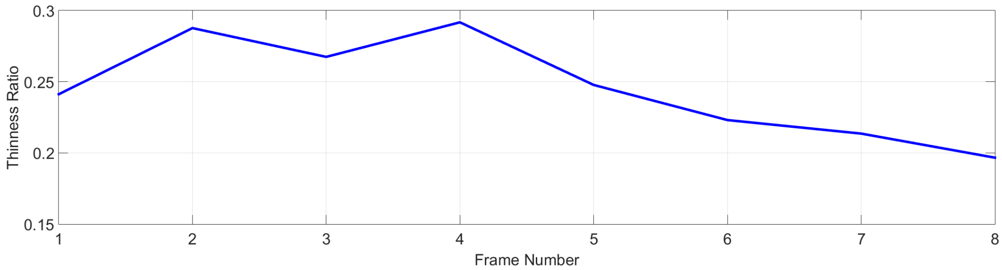


FIGURE 6.70: Thinness ratio changes during the motion

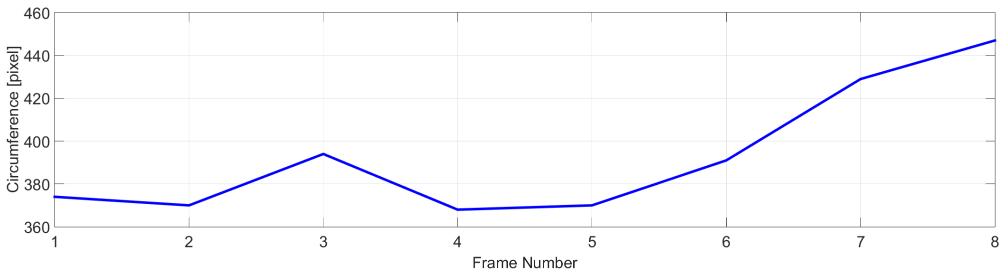


FIGURE 6.71: Circumference changes during the motion

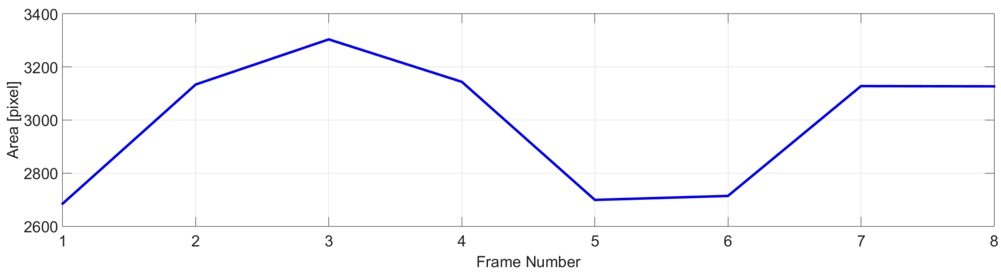


FIGURE 6.72: Area changes during the motion

### 6.3.9 Splitting Example - 1

- Single bubble with approximately 614 $\mu$m diameter splits into two bubbles with diameters of 328 $\mu$m and 419 $\mu$m (Starting frame no: 31)

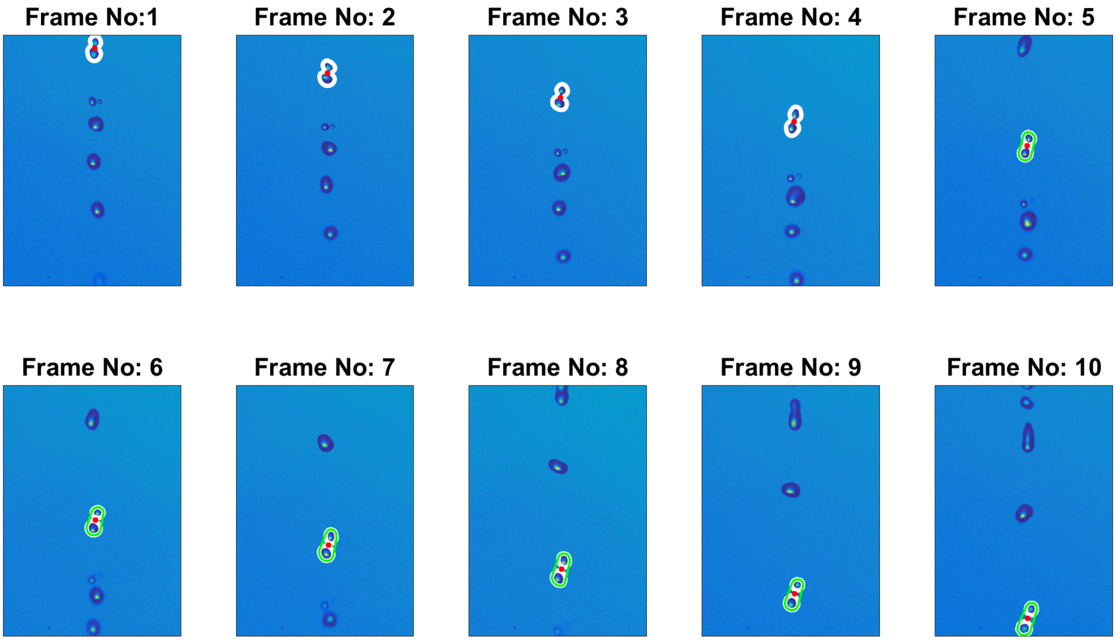


FIGURE 6.73: Bubble Tracking

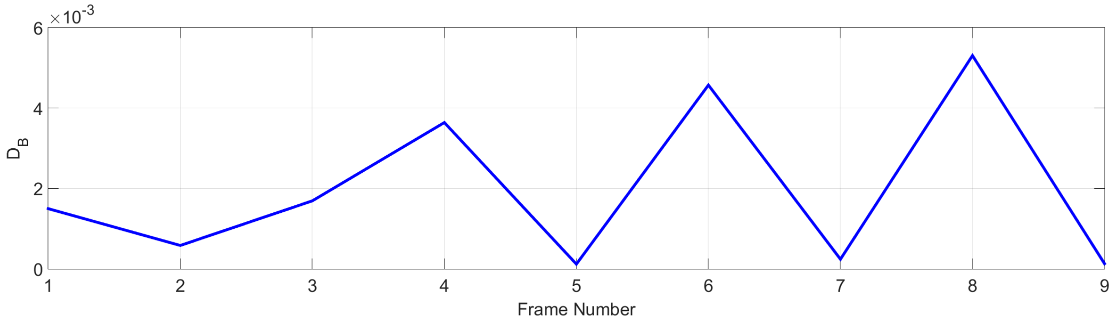


FIGURE 6.74: Minimum Bhattacharyya distances during the motion

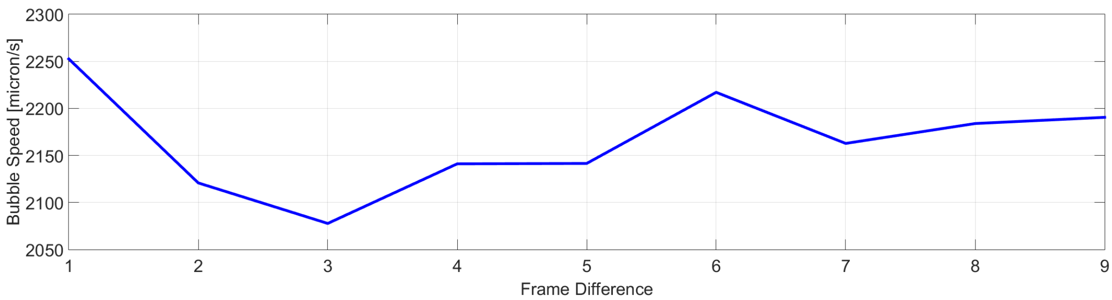


FIGURE 6.75: Speed of tracked bubbles

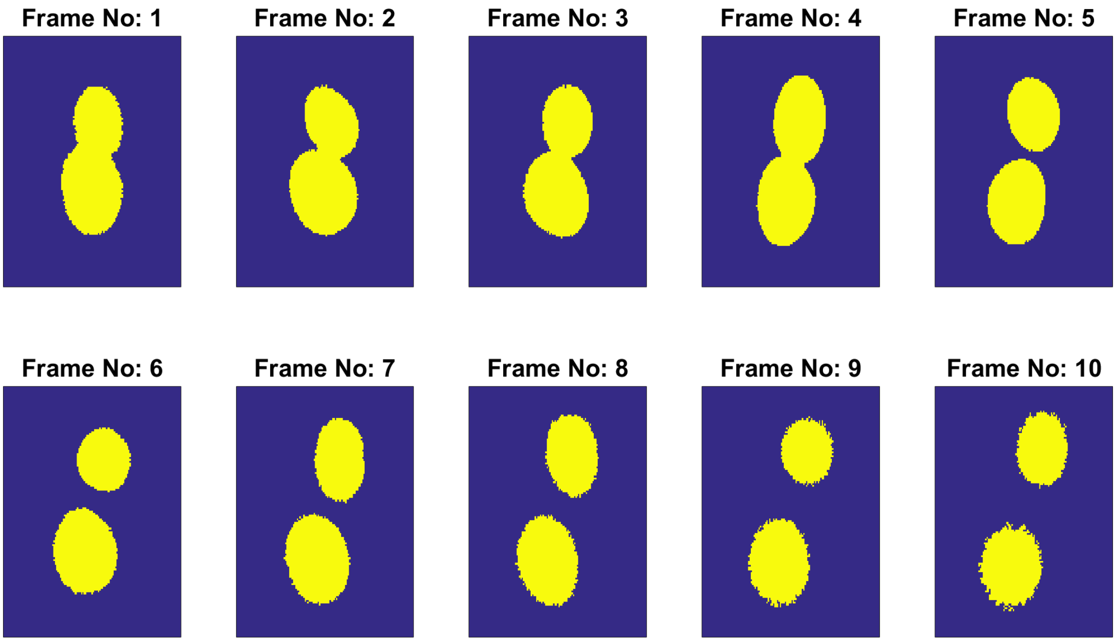


FIGURE 6.76: Silhouettes of tracked bubbles

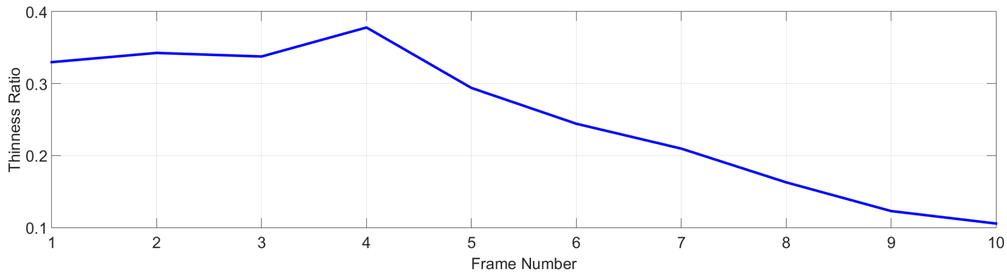


FIGURE 6.77: Thinness ratio changes during the motion

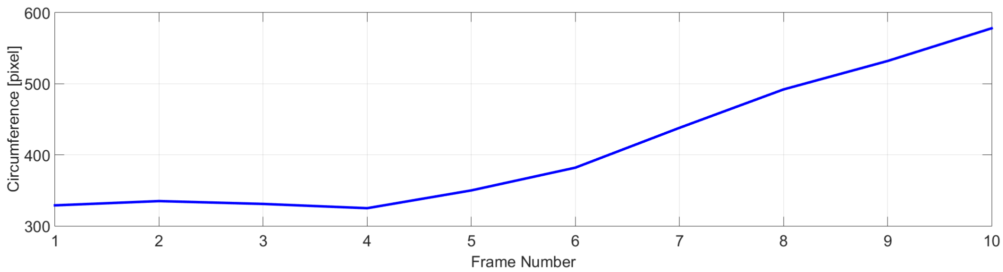


FIGURE 6.78: Circumference changes during the motion

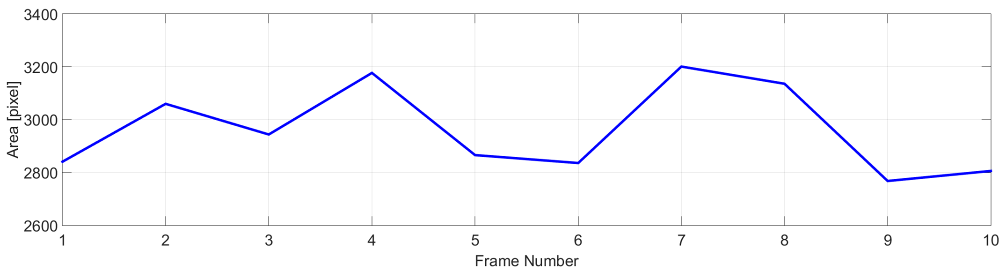


FIGURE 6.79: Area changes during the motion

### 6.3.10 Splitting Example - 2

- Single bubble with approximately 602 $\mu$m diameter splits into two bubbles with diameters of 450 $\mu$m and 358 $\mu$m (Starting frame no: 218)

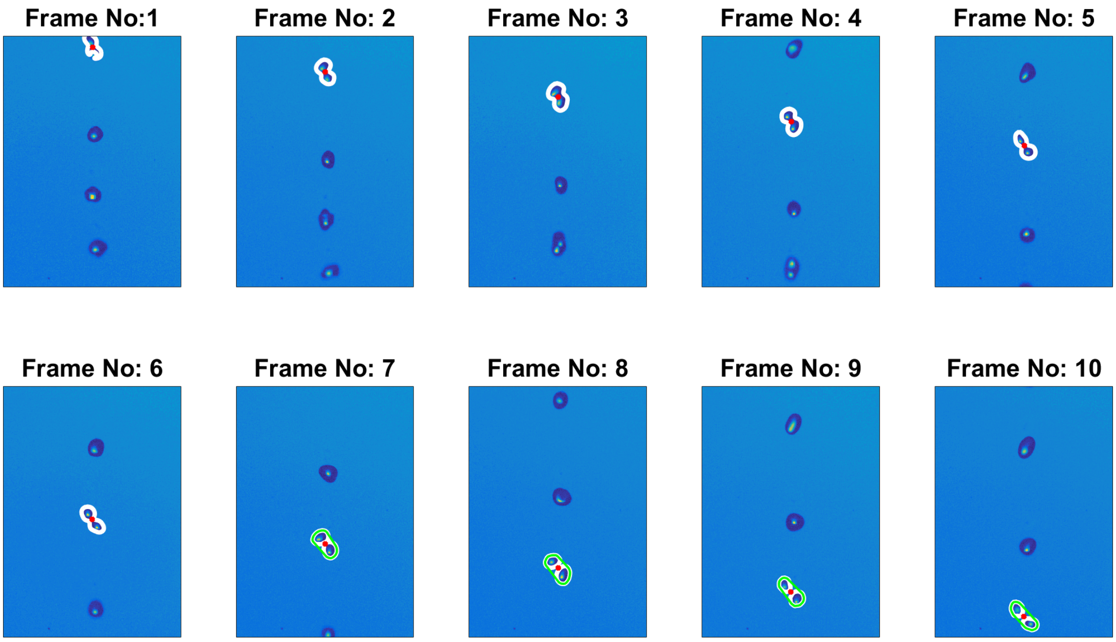


FIGURE 6.80: Bubble Tracking

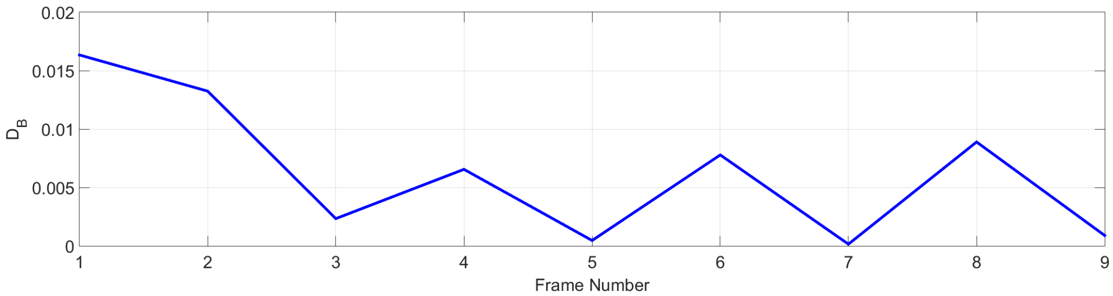


FIGURE 6.81: Minimum Bhattacharyya distances during the motion

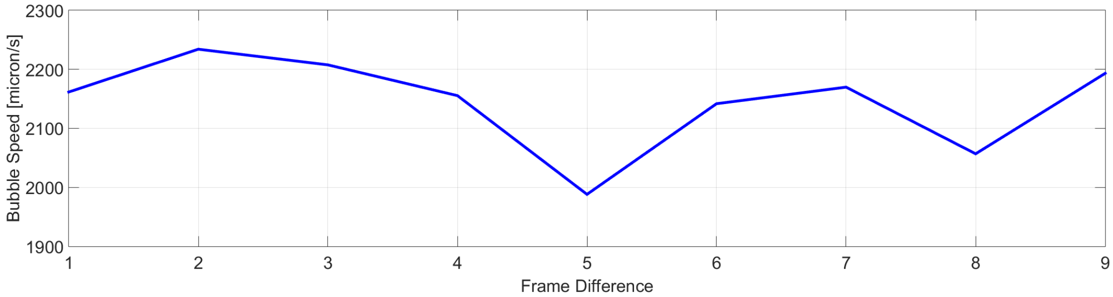


FIGURE 6.82: Speed of tracked bubbles

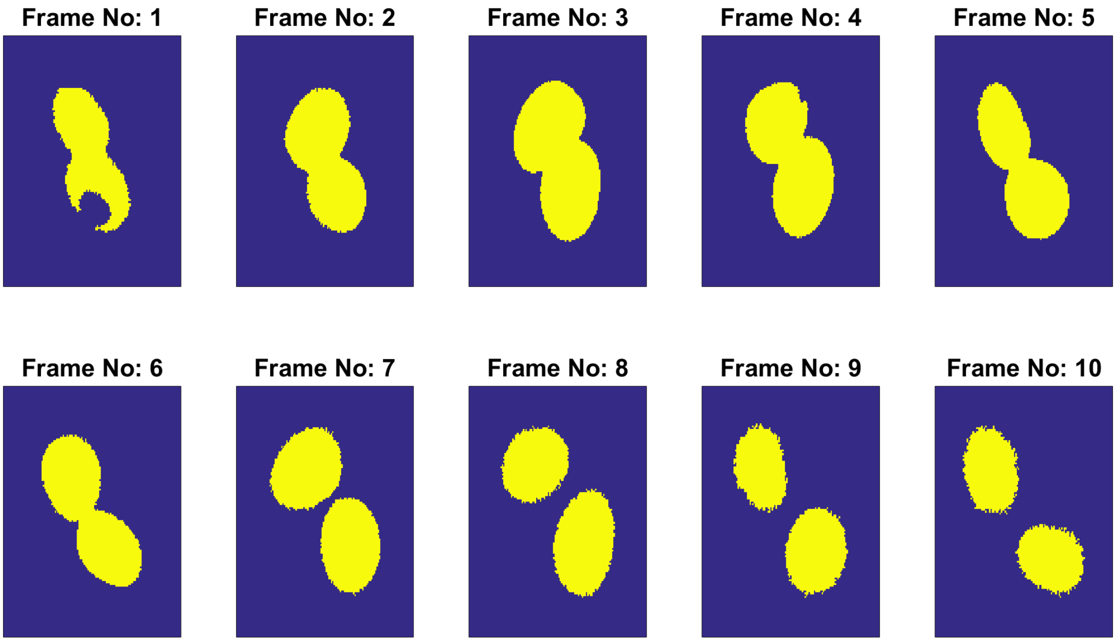


FIGURE 6.83: Silhouettes of tracked bubbles

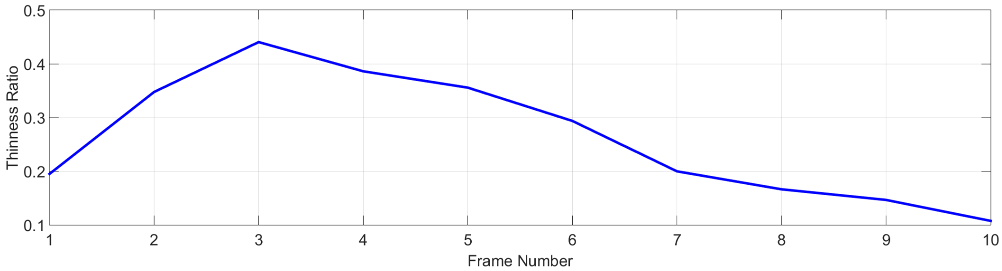


FIGURE 6.84: Thinness ratio changes during the motion

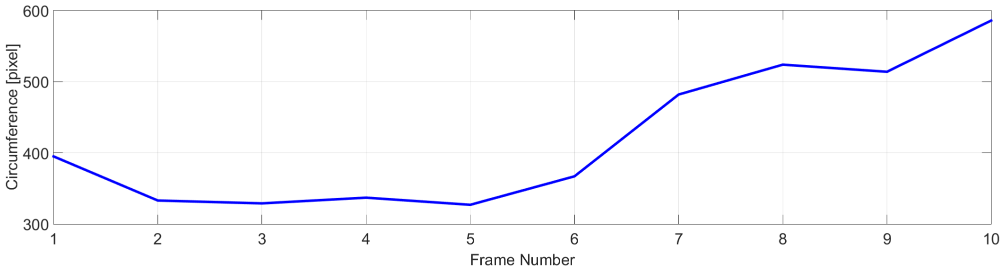


FIGURE 6.85: Circumference changes during the motion

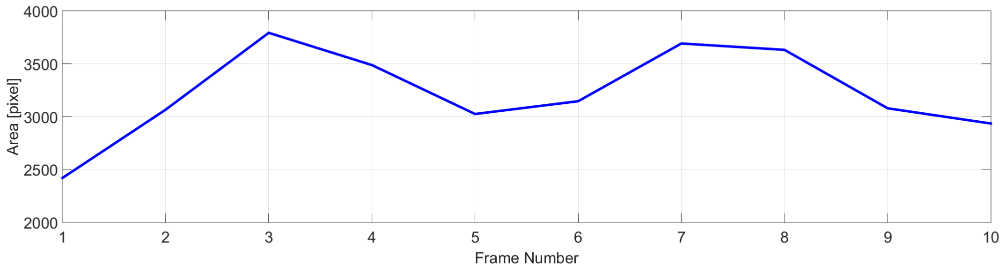


FIGURE 6.86: Area changes during the motion

### 6.3.11 Splitting Example - 3

- Double bubble structure splits into three bubbles with diameters of 269 $\mu$m, 463 $\mu$m and 358 $\mu$m (Starting frame no: 388)

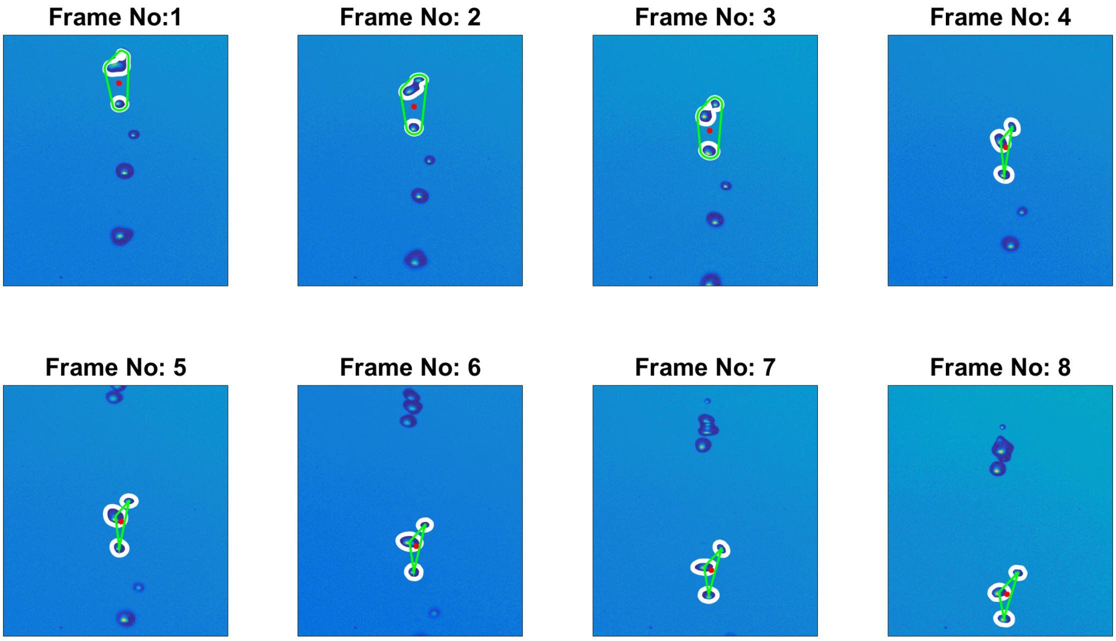


FIGURE 6.87: Bubble Tracking

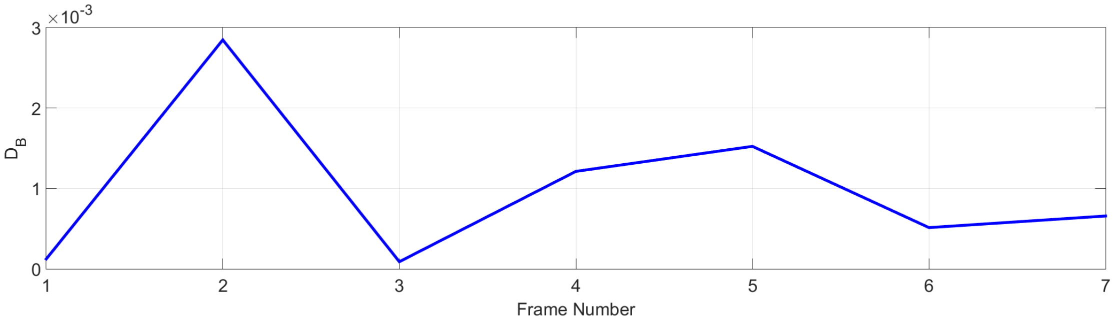


FIGURE 6.88: Minimum Bhattacharyya distances during the motion

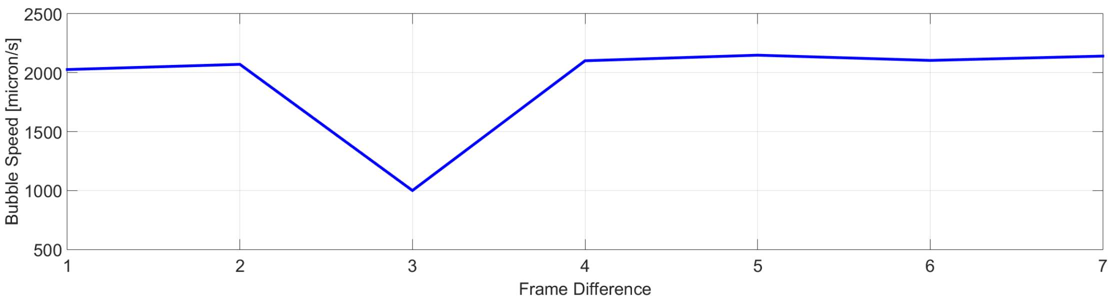


FIGURE 6.89: Speed of tracked bubbles

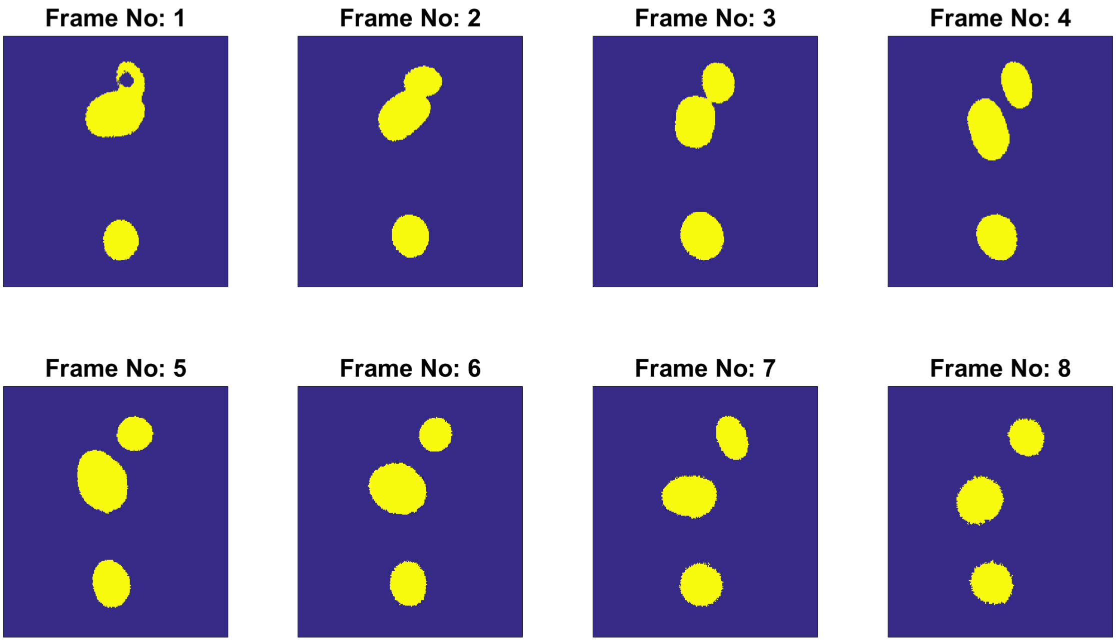


FIGURE 6.90: Silhouettes of tracked bubbles

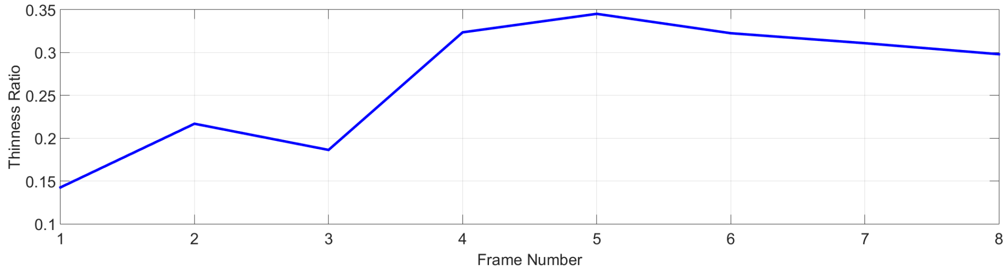


FIGURE 6.91: Thinness ratio changes during the motion

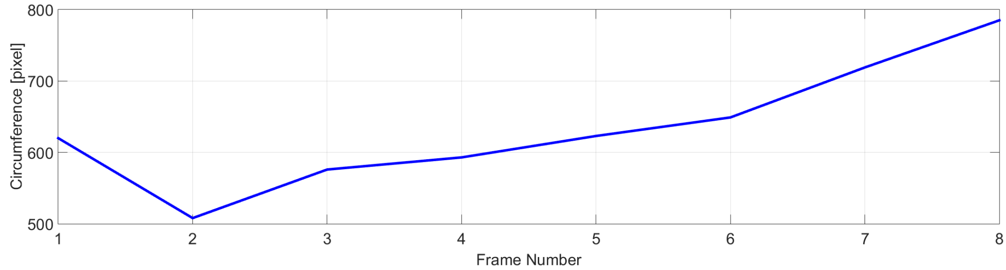


FIGURE 6.92: Circumference changes during the motion

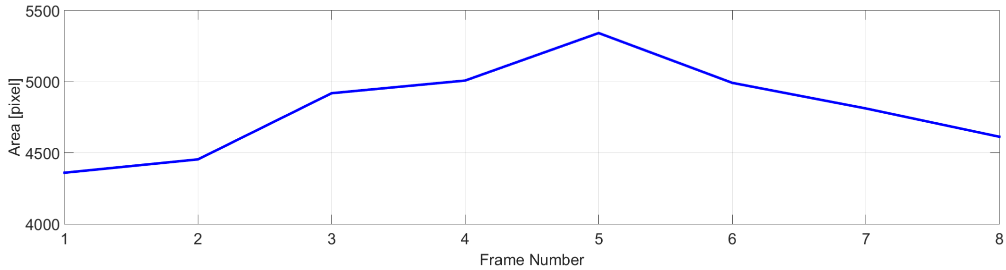


FIGURE 6.93: Area changes during the motion

### 6.3.12 Consecutive Merging and Splitting Example

- Two single bubbles with approximately 356 $\mu$m and 366 $\mu$m diameters merge and splits consecutively. (Starting frame no: 41)

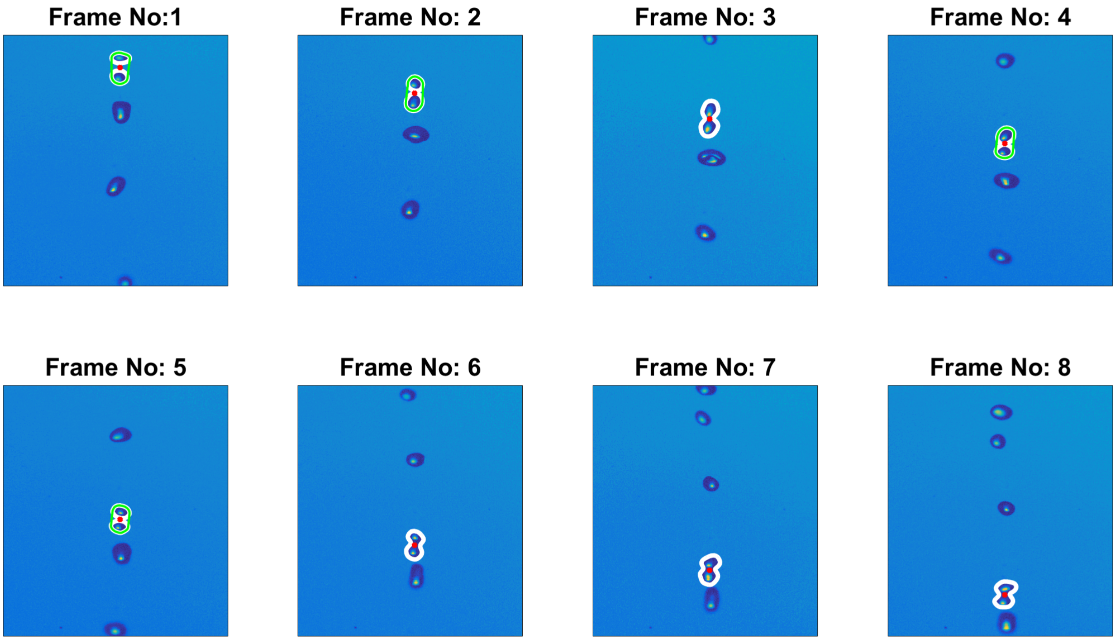


FIGURE 6.94: Bubble Tracking

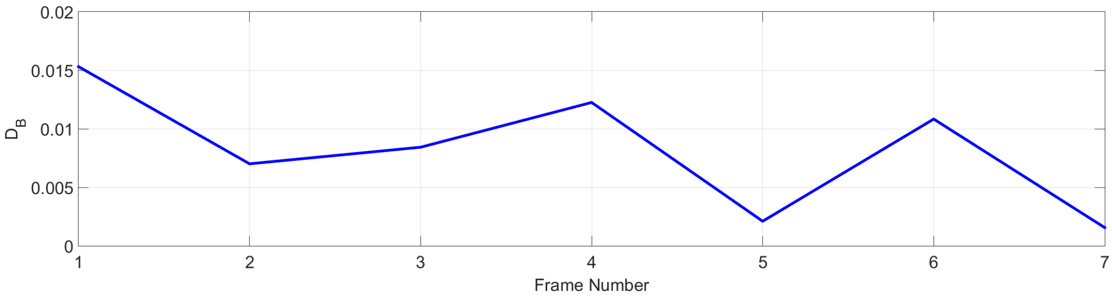


FIGURE 6.95: Minimum Bhattacharyya distances during the motion

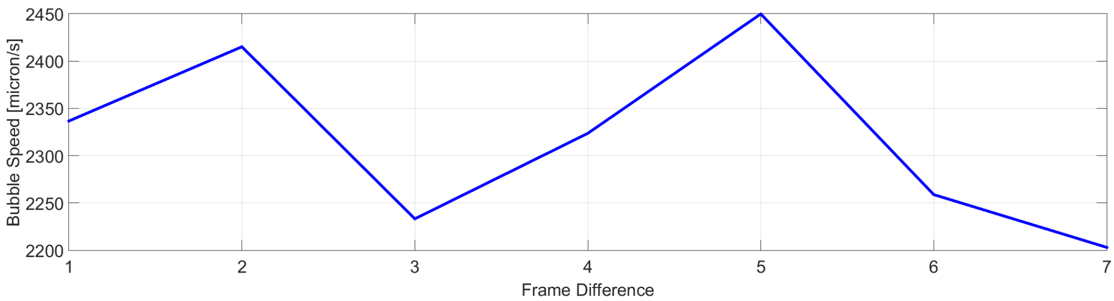


FIGURE 6.96: Speed of tracked bubbles

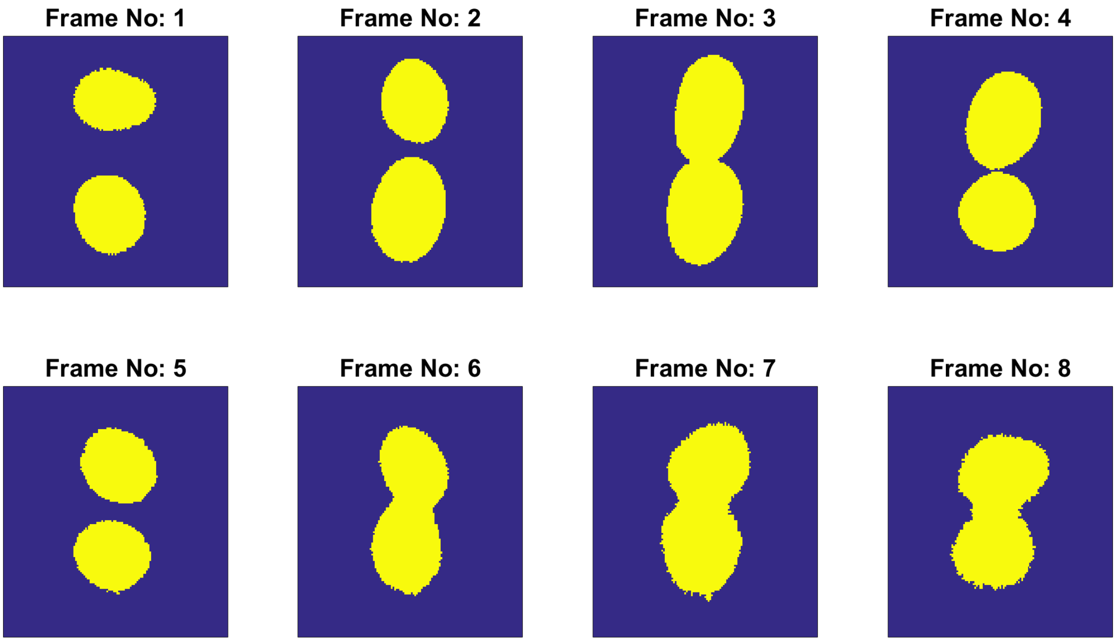


FIGURE 6.97: Silhouettes of tracked bubbles

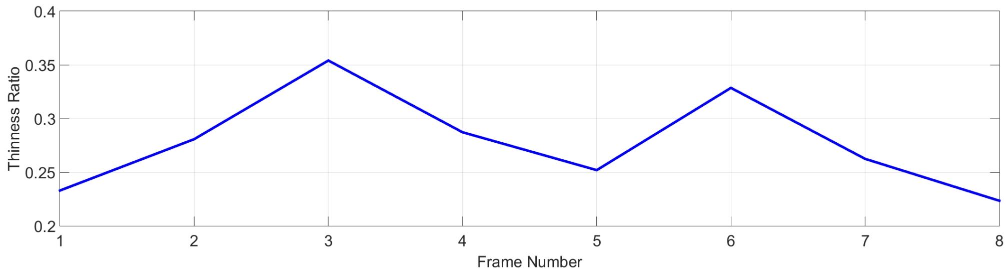


FIGURE 6.98: Thinness ratio changes during the motion

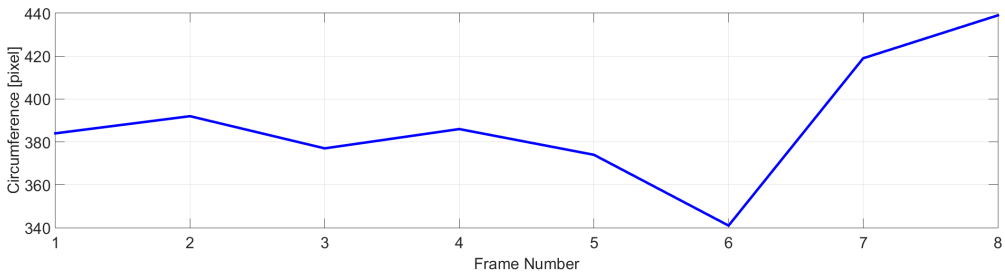


FIGURE 6.99: Circumference changes during the motion

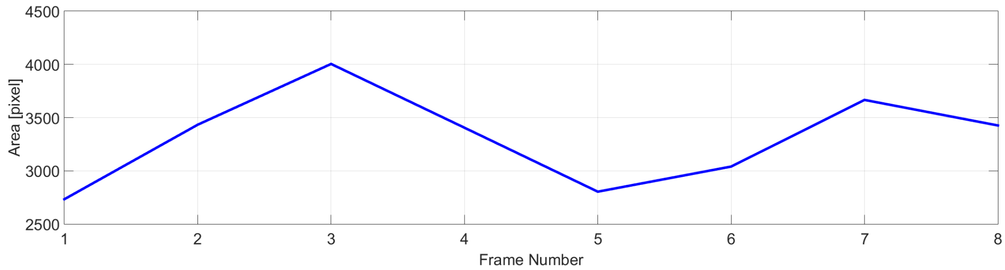


FIGURE 6.100: Area changes during the motion

### 6.3.13 Individual Bubble Tracking Example - 1

- During double bubble tracking one of the bubbles alters its shape dramatically. (Starting frame no: 75)

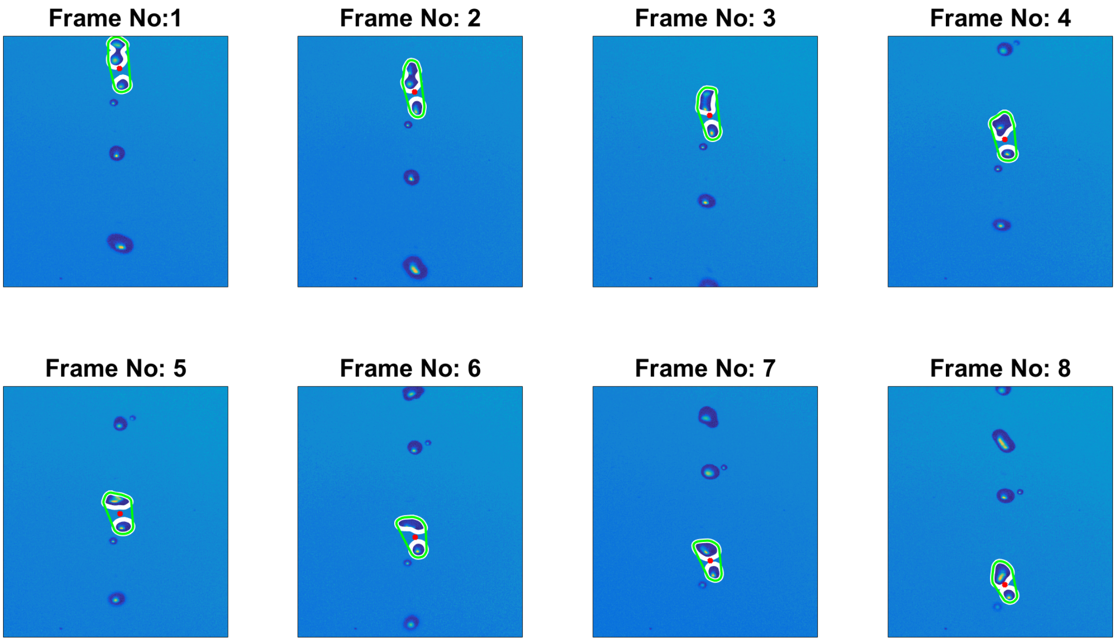


FIGURE 6.101: Bubble Tracking

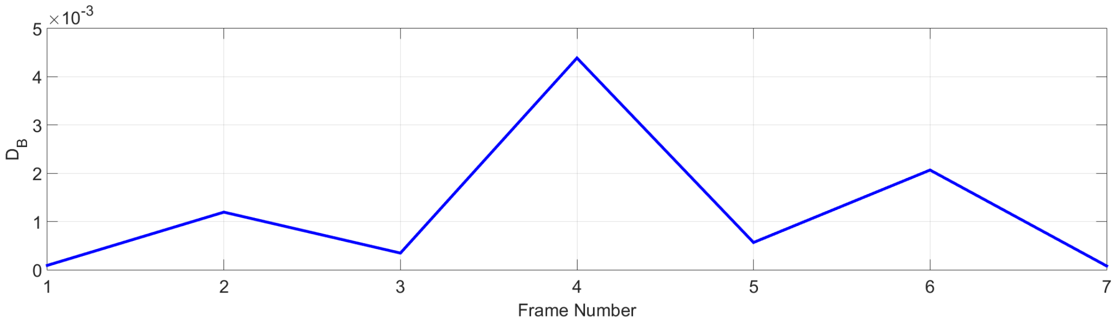


FIGURE 6.102: Minimum Bhattacharyya distances during the motion

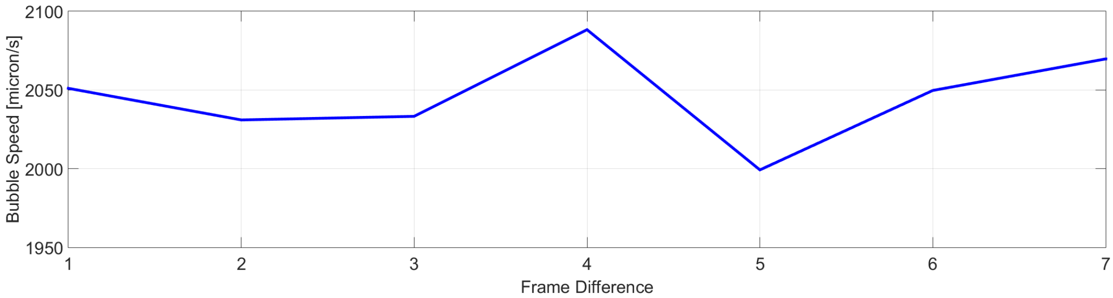


FIGURE 6.103: Speed of tracked bubbles

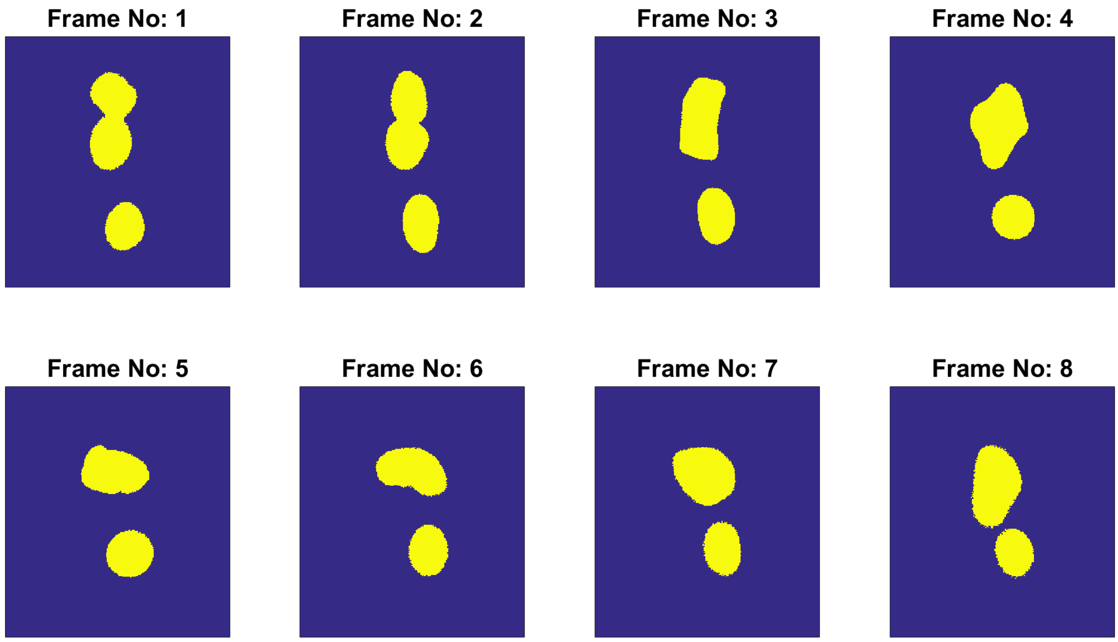


FIGURE 6.104: Silhouettes of tracked bubbles

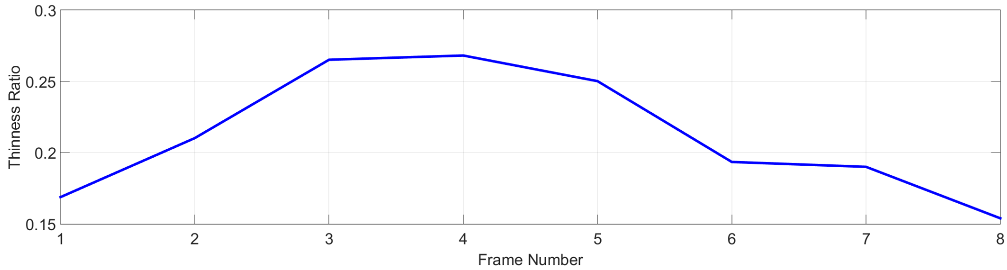


FIGURE 6.105: Thinness ratio changes during the motion

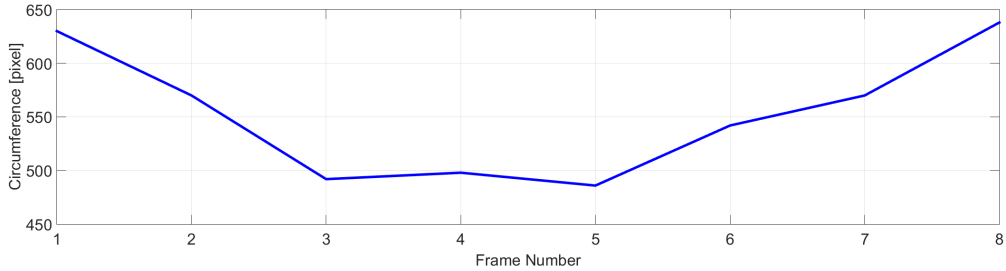


FIGURE 6.106: Circumference changes during the motion

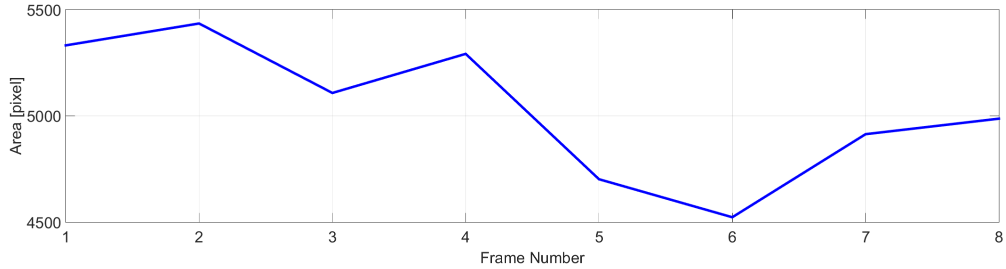


FIGURE 6.107: Area changes during the motion

### 6.3.14 Individual Bubble Tracking Example - 2

- Two bubbles with approximately 300 $\mu$m and 387 $\mu$m diameters are tracked. (Starting frame no: 155)

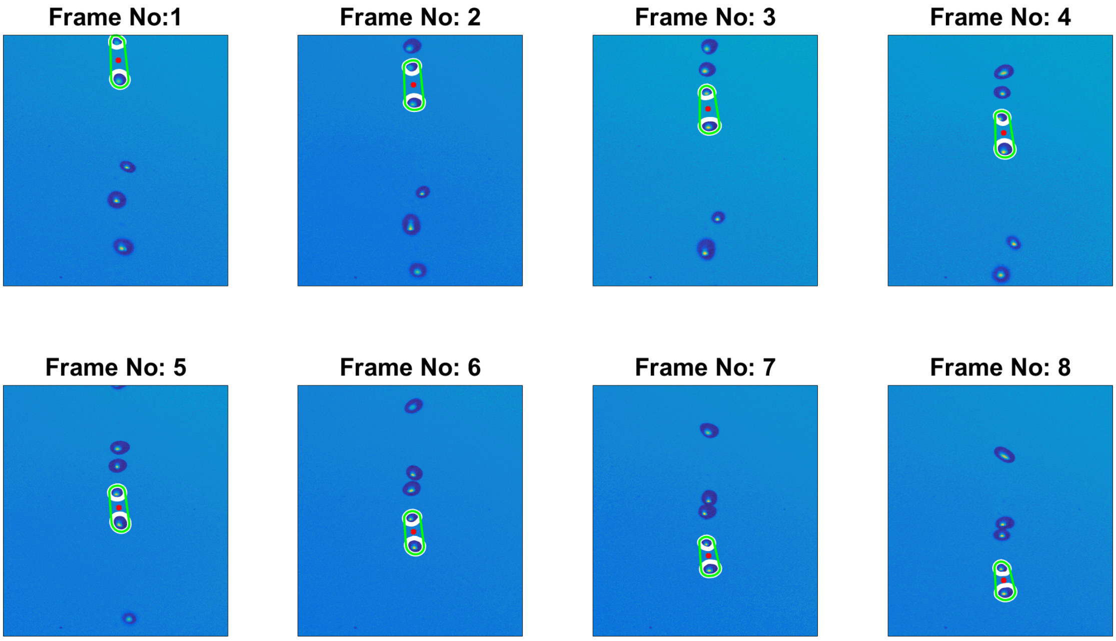


FIGURE 6.108: Bubble Tracking

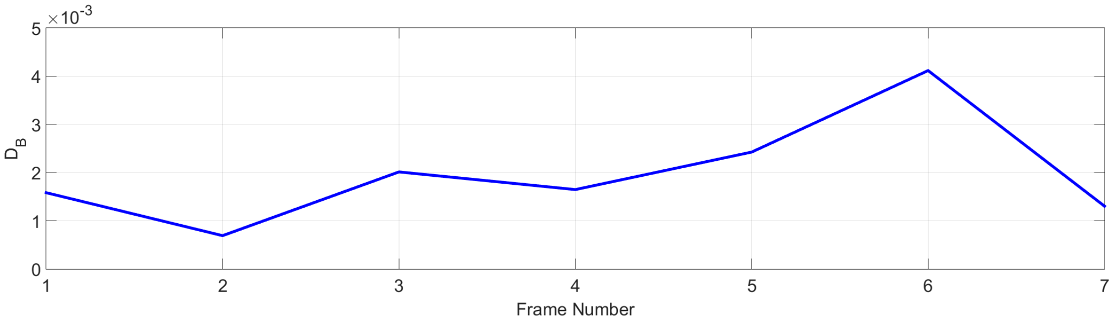


FIGURE 6.109: Minimum Bhattacharyya distances during the motion

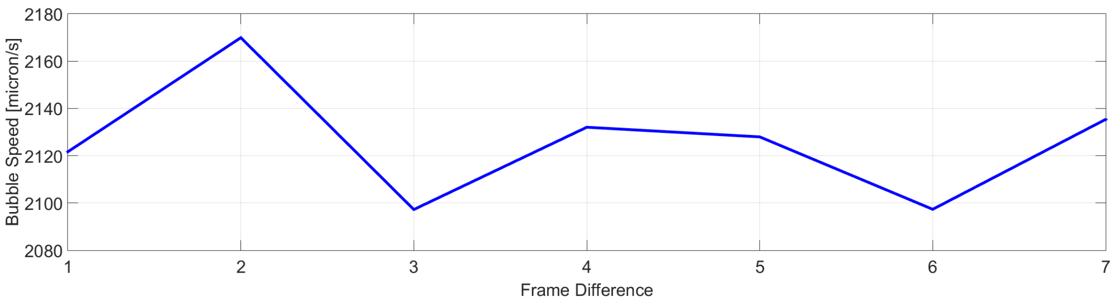


FIGURE 6.110: Speed of tracked bubbles

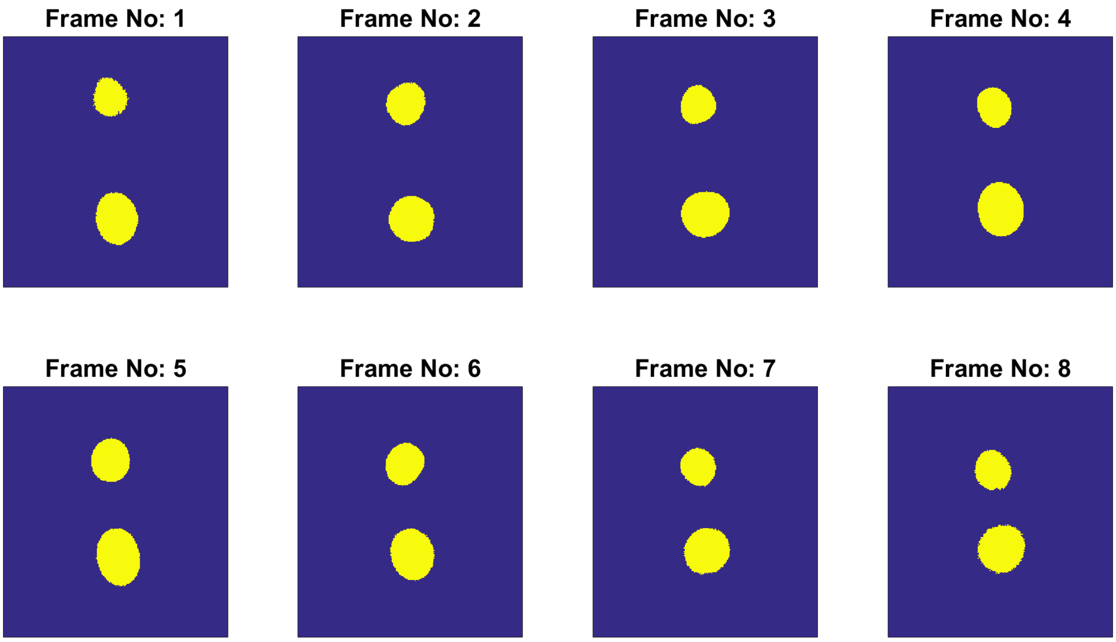


FIGURE 6.111: Silhouettes of tracked bubbles

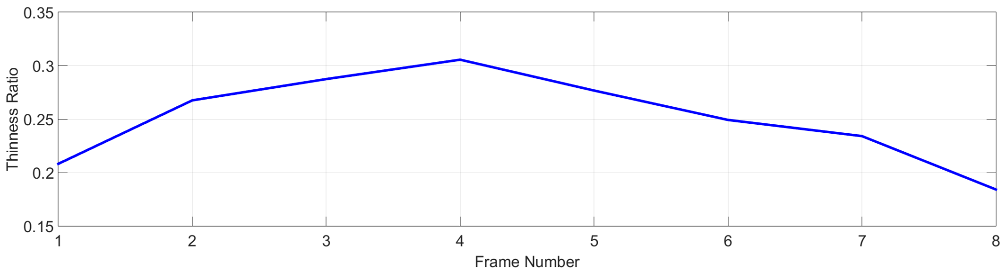


FIGURE 6.112: Thinness ratio changes during the motion

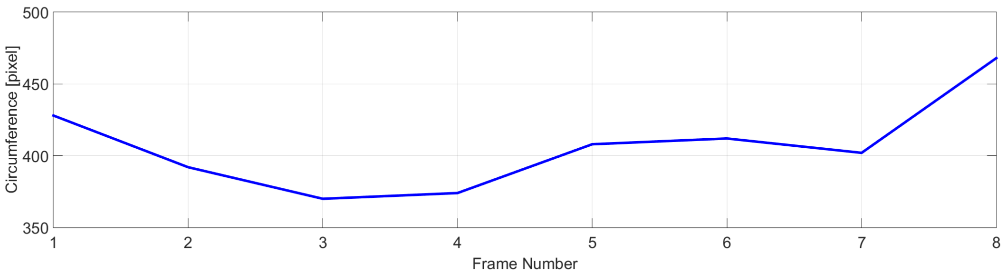


FIGURE 6.113: Circumference changes during the motion

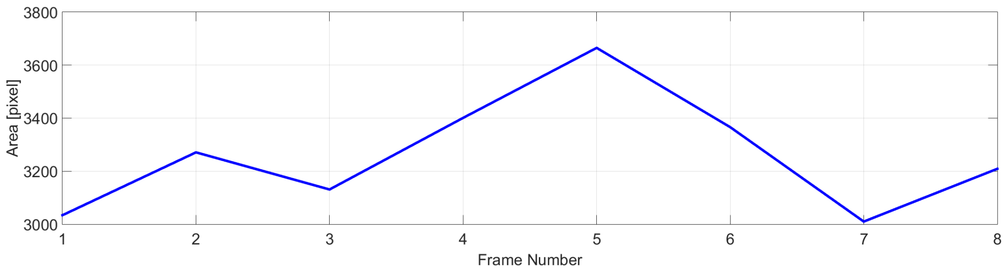


FIGURE 6.114: Area changes during the motion

### 6.3.15 Individual Bubble Tracking Example - 3

- Three bubbles with approximately 375 $\mu$m, 311 $\mu$m and 280 $\mu$m diameters are tracked after splitting. (Starting frame no: 550)

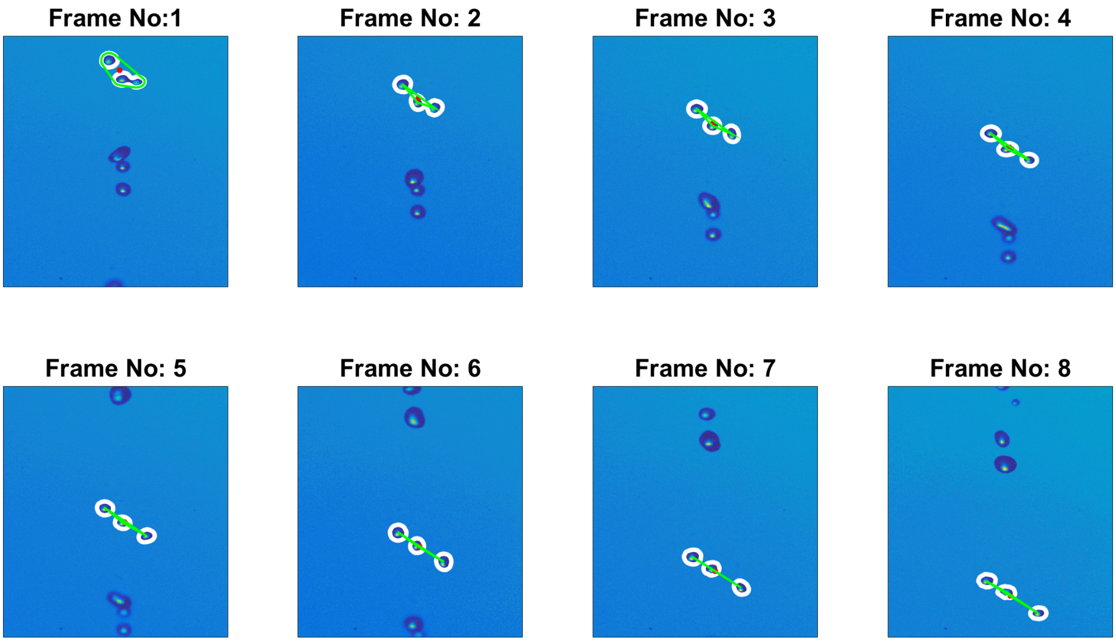


FIGURE 6.115: Bubble Tracking

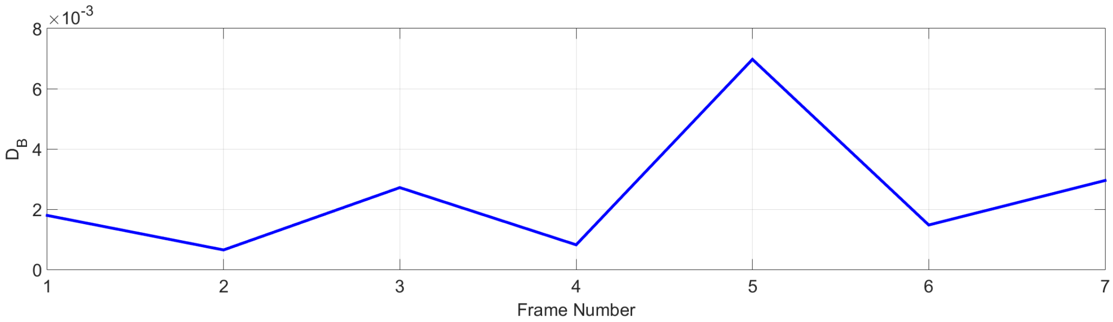


FIGURE 6.116: Minimum Bhattacharyya distances during the motion

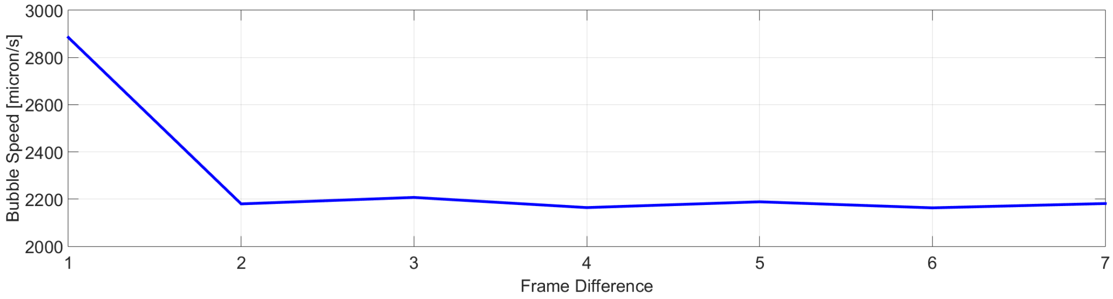


FIGURE 6.117: Speed of tracked bubbles

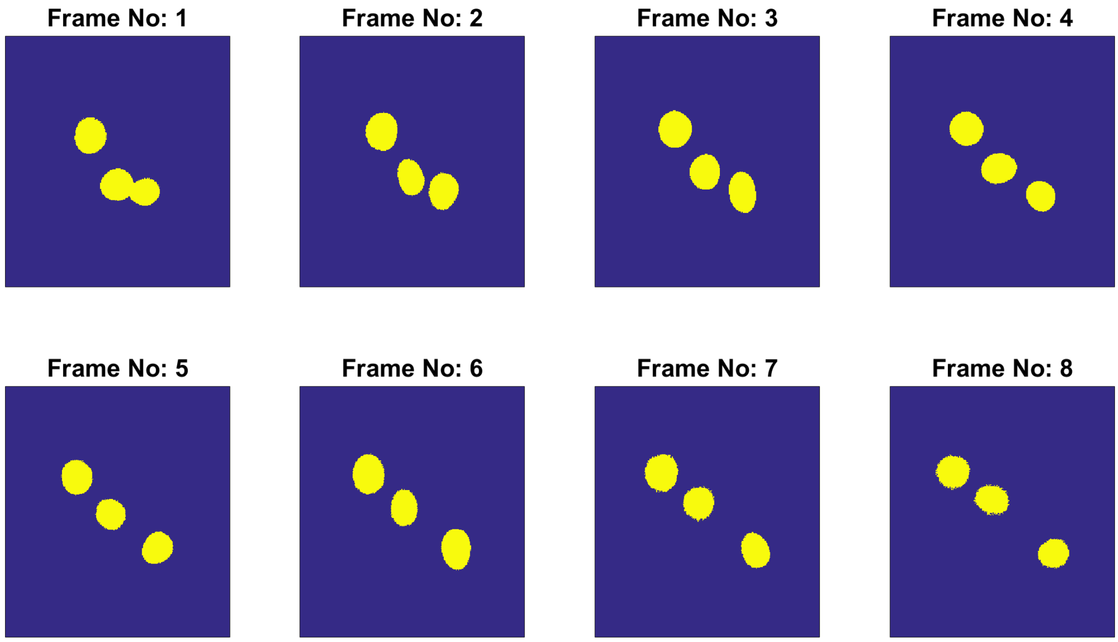


FIGURE 6.118: Silhouettes of tracked bubbles

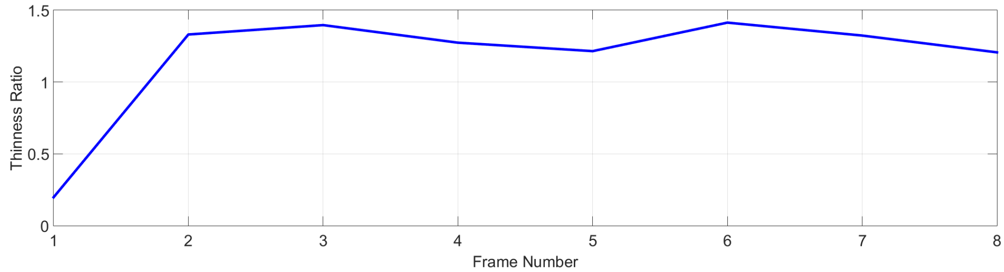


FIGURE 6.119: Thinness ratio changes during the motion

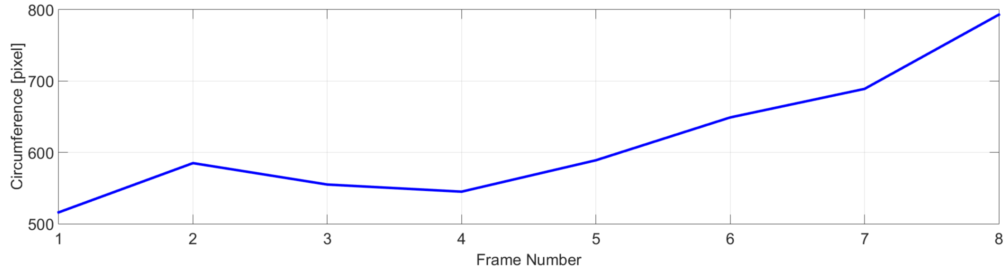


FIGURE 6.120: Circumference changes during the motion

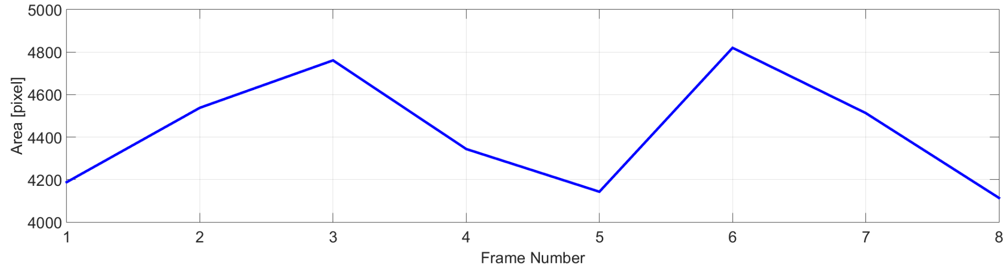


FIGURE 6.121: Area changes during the motion

### 6.3.16 Triple, Double and Single Tracking Example

- Three bubbles with approximately 364 $\mu$m, 470 $\mu$m and 397 $\mu$m diameters merge and split consecutively. (Starting frame no: 112)

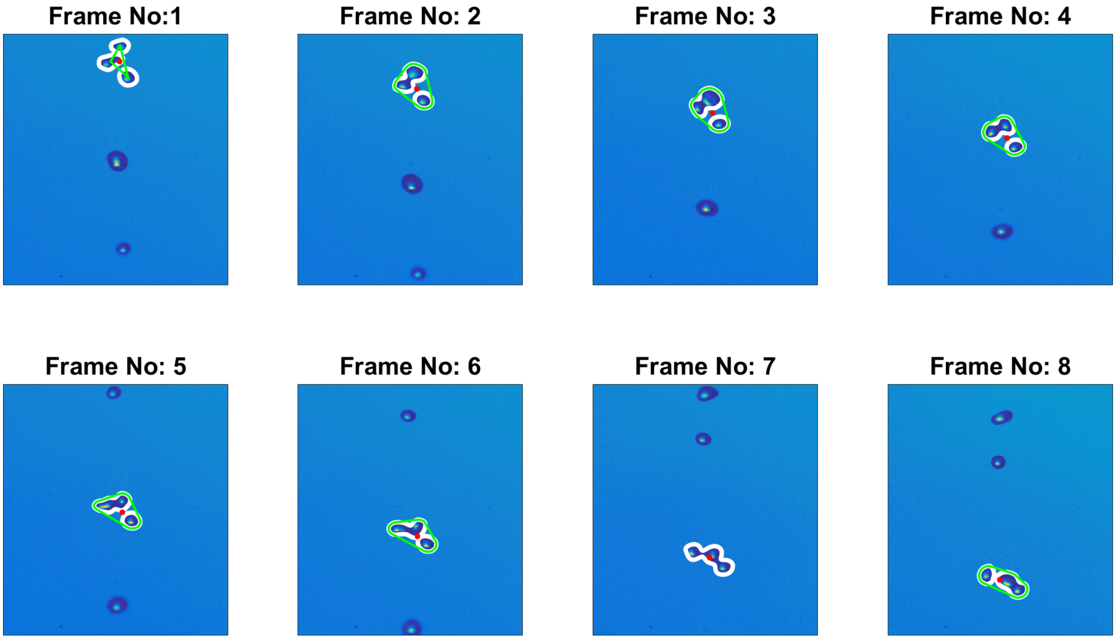


FIGURE 6.122: Bubble Tracking

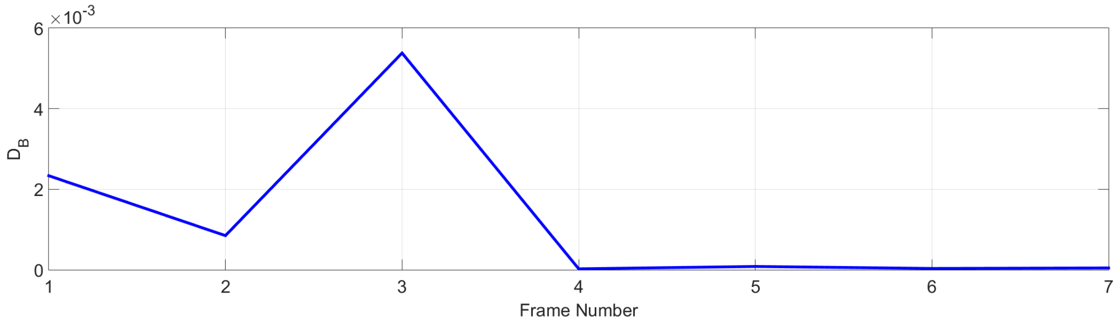


FIGURE 6.123: Minimum Bhattacharyya distances during the motion

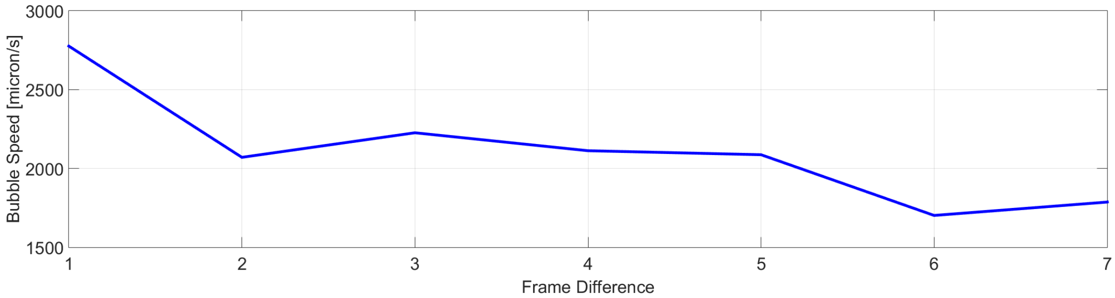


FIGURE 6.124: Speed of tracked bubbles

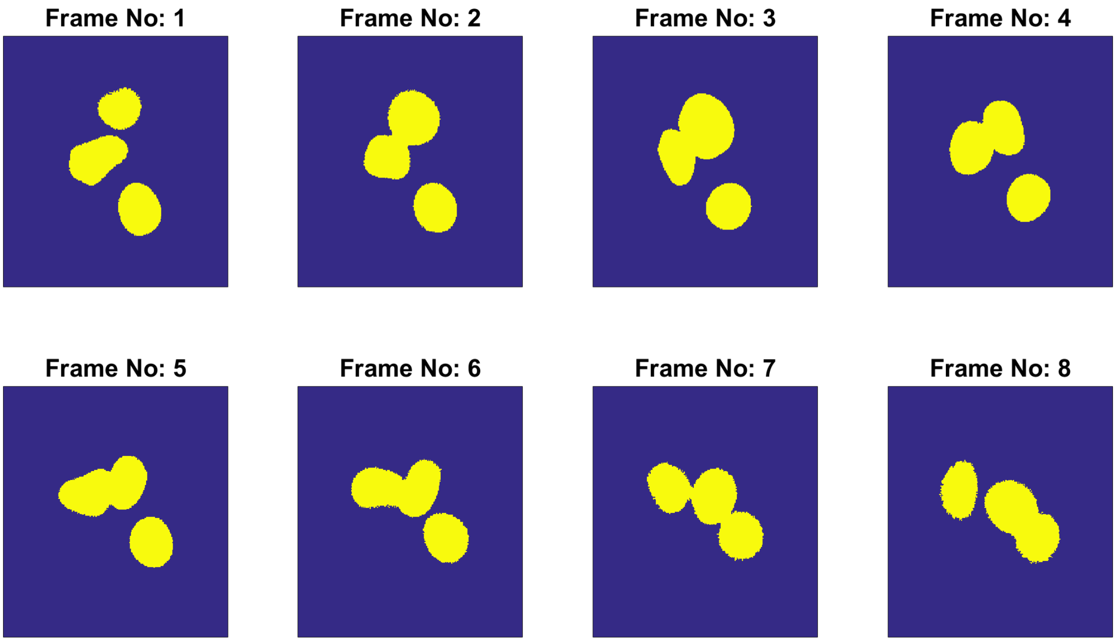


FIGURE 6.125: Silhouettes of tracked bubbles

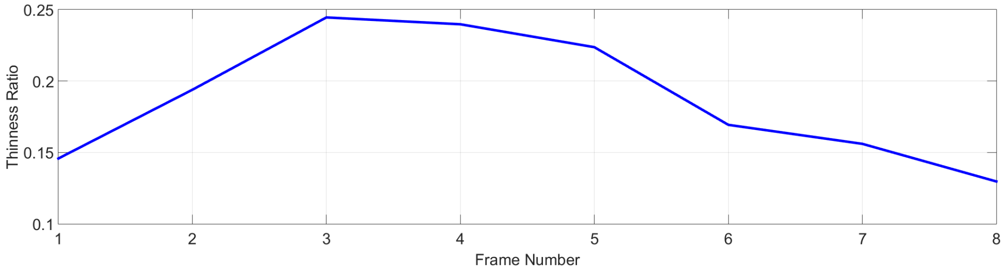


FIGURE 6.126: Thinness ratio changes during the motion

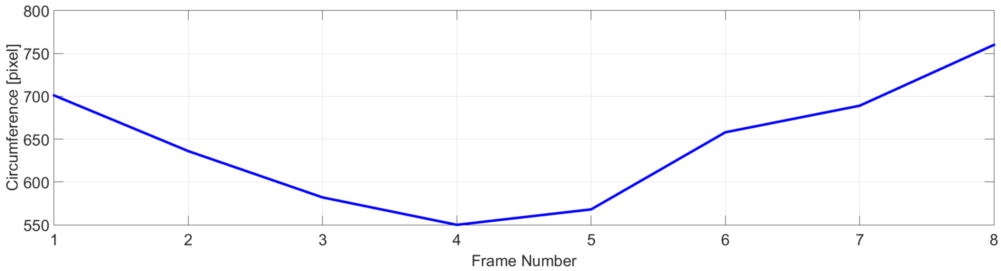


FIGURE 6.127: Circumference changes during the motion

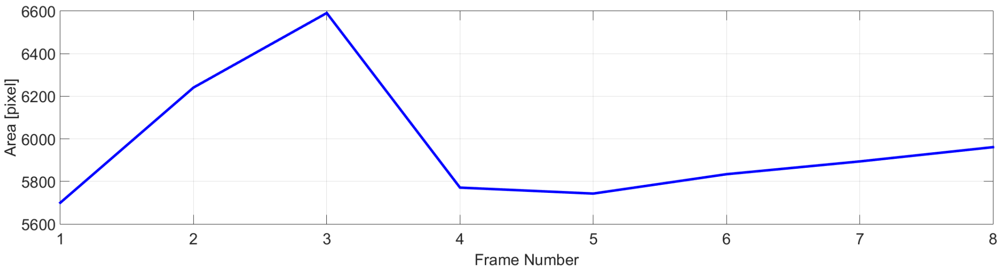


FIGURE 6.128: Area changes during the motion

## 6.4 EFD Modeling

EFD models of single bubble tracked in Section 6.3.1 are shown in Figure 6.129. Figures 6.130 and 6.131 show that first and third harmonics are dominant accord-

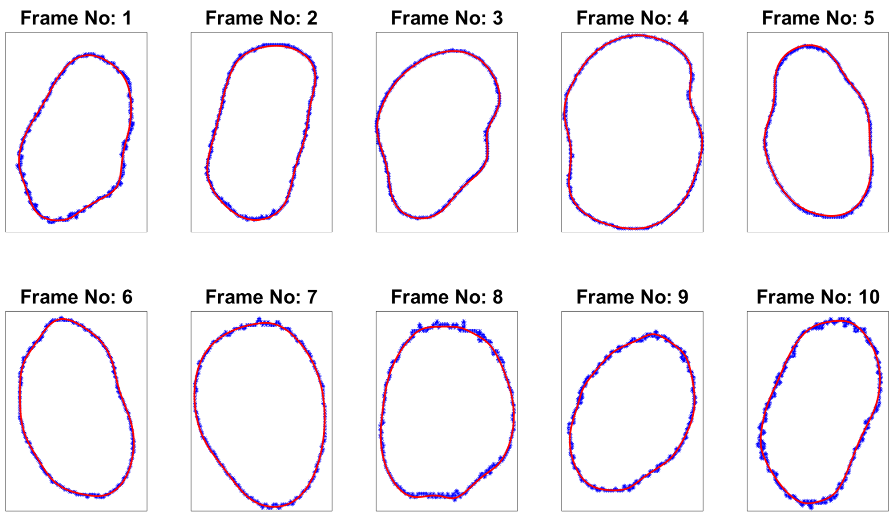


FIGURE 6.129: EFD models of tracked bubbles

ing to $a$ and $b$ features. Major axis ($a$) is dominant over minor axis ($b$) since bubble changes its elliptic shapes during the motion.

| | $a_1$ | $a_2$ | $a_3$ | $a_4$ | $a_5$ | $a_6$ | $a_7$ | $a_8$ |
|---|---|---|---|---|---|---|---|---|
| F:1 | 37.5415 | 2.1880 | 2.1746 | 1.3417 | 0.5896 | 0.7467 | 0.4417 | 0.2996 |
| F:2 | 43.4364 | 1.3961 | 3.7060 | 0.7575 | 0.5020 | 0.4461 | 0.3449 | 0.1423 |
| F:3 | 46.9455 | 2.0456 | 3.5691 | 1.0682 | 0.8757 | 0.8697 | 0.4917 | 0.2375 |
| F:4 | 46.0731 | 0.5705 | 3.5297 | 0.3183 | 1.1405 | 0.3948 | 0.4609 | 0.1845 |
| F:5 | 41.5536 | 1.9976 | 2.3520 | 0.5995 | 0.9182 | 0.4080 | 0.2445 | 0.2386 |
| F:6 | 36.9090 | 1.2068 | 1.2539 | 0.7365 | 0.3897 | 0.4261 | 0.3012 | 0.2697 |
| F:7 | 35.7855 | 1.3956 | 1.7285 | 0.5048 | 0.3505 | 0.0726 | 0.1691 | 0.1147 |
| F:8 | 35.0930 | 1.7129 | 2.3927 | 1.1929 | 0.3432 | 0.6975 | 0.3295 | 0.4147 |
| F:9 | 36.3615 | 1.4138 | 1.7456 | 0.9861 | 0.6379 | 0.4757 | 0.1856 | 0.4869 |
| F:10 | 38.3321 | 2.9243 | 2.4248 | 0.9923 | 0.3024 | 0.9142 | 0.4797 | 0.2330 |

TABLE 6.2: Major axis ($a$) changes of harmonics throughout the tracked frames

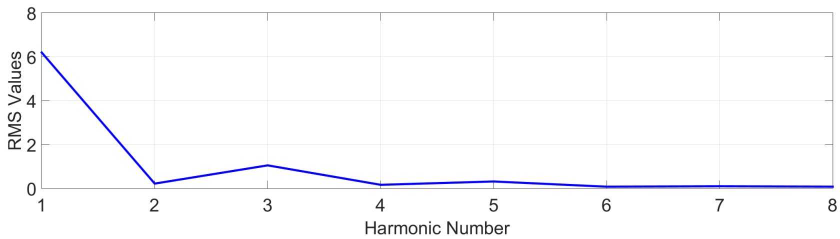


FIGURE 6.130: RMS Values of Covariance Columns for ‘a’

| | $b_1$ | $b_2$ | $b_3$ | $b_4$ | $b_5$ | $b_6$ | $b_7$ | $b_8$ |
|---|---|---|---|---|---|---|---|---|
| F:1 | 28.5617 | 0.3414 | 1.3194 | 0.1600 | 0.2224 | 0.3069 | 0.2382 | 0.0504 |
| F:2 | 28.3603 | 0.3412 | 1.3155 | 0.1797 | 0.1997 | 0.0729 | 0.0703 | 0.0362 |
| F:3 | 29.4485 | 0.6137 | 1.8000 | 0.1478 | 0.4507 | 0.1921 | 0.2727 | 0.1149 |
| F:4 | 30.9607 | 0.0118 | 2.2325 | 0.1972 | 0.0006 | 0.0645 | 0.0890 | 0.0922 |
| F:5 | 30.2453 | 0.2910 | 0.8816 | 0.3581 | 0.1163 | 0.1252 | 0.1409 | 0.1063 |
| F:6 | 29.3057 | 0.5863 | 0.7386 | 0.5276 | 0.1347 | 0.1788 | 0.0171 | 0.0967 |
| F:7 | 27.7846 | 0.6696 | 1.0029 | 0.3910 | 0.0056 | 0.0067 | 0.0578 | 0.0639 |
| F:8 | 27.7527 | 0.5107 | 2.0570 | 0.2622 | 0.1762 | 0.2071 | 0.2561 | 0.1100 |
| F:9 | 27.9491 | 1.0050 | 1.1010 | 0.8779 | 0.0051 | 0.0557 | 0.0206 | 0.1882 |
| F:10 | 28.9105 | 0.2825 | 0.0592 | 0.0761 | 0.1471 | 0.1407 | 0.1675 | 0.0611 |

TABLE 6.3: Minor axis ($b$) changes of harmonics throughout the tracked frames

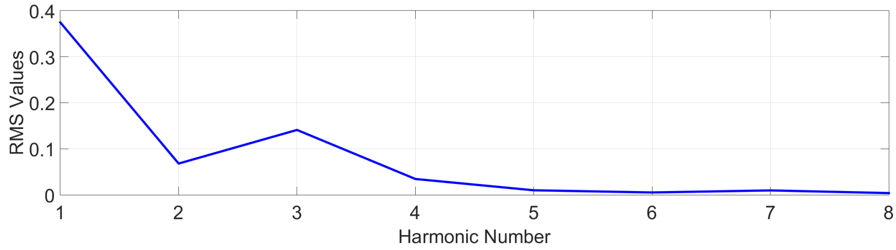


FIGURE 6.131: RMS Values of Covariance Columns for ‘b’

| | $\theta_1$ | $\theta_2$ | $\theta_3$ | $\theta_4$ | $\theta_5$ | $\theta_6$ | $\theta_7$ | $\theta_8$ |
|---|---|---|---|---|---|---|---|---|
| F:1 | 0.9701 | -1.8252 | 1.5274 | 2.6317 | 2.4001 | 2.6553 | -2.9672 | -2.5900 |
| F:2 | 1.2987 | -3.1011 | 2.8720 | -2.6541 | -2.0487 | -3.0374 | 2.7283 | -2.7340 |
| F:3 | 1.3541 | 2.8327 | -2.0603 | -2.6776 | 2.3358 | 2.8177 | 2.9551 | 3.1352 |
| F:4 | 1.5171 | 2.8679 | -2.7675 | -2.2491 | 3.1033 | -3.0054 | -2.9015 | 3.0637 |
| F:5 | 1.7983 | 2.9118 | 2.1818 | 1.8293 | -3.0850 | -2.9752 | -2.2215 | 3.1135 |
| F:6 | 2.1836 | -2.6844 | -2.8771 | 2.9603 | 3.0835 | 1.3488 | -1.9396 | 2.8040 |
| F:7 | 2.8665 | 1.9119 | 3.0171 | -2.8334 | -1.7984 | -2.4033 | 1.4590 | -3.1023 |
| F:8 | -3.0208 | -2.6414 | 1.4655 | 2.7454 | 1.6556 | 1.3214 | 0.9936 | -2.9833 |
| F:9 | -2.5512 | 2.0839 | 1.6886 | -2.4331 | -3.0265 | -1.9417 | 1.9757 | 3.0427 |
| F:10 | 0.9618 | -1.7803 | 2.5368 | 2.4034 | 2.9013 | 1.7319 | 1.6955 | -2.4811 |

TABLE 6.4: Angle in radian ($\theta$) changes of harmonics throughout the tracked frames

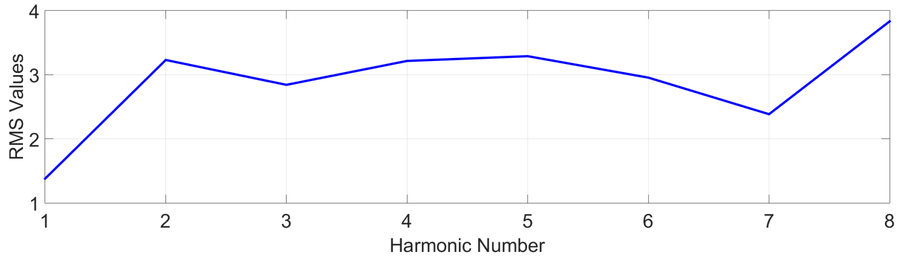


FIGURE 6.132: RMS Values of Covariance Columns for ‘$\theta$’

EFD models of single bubble tracked in Section 6.3.2 are shown in Figure 6.133. Figures 6.134 and 6.135 show that first four harmonics are dominant according to $a$ and $b$ features. Major axis ($a$) and minor axis ($b$) are equally dominant since the bubble is just rotating and not much changing its elliptic shape during the motion.

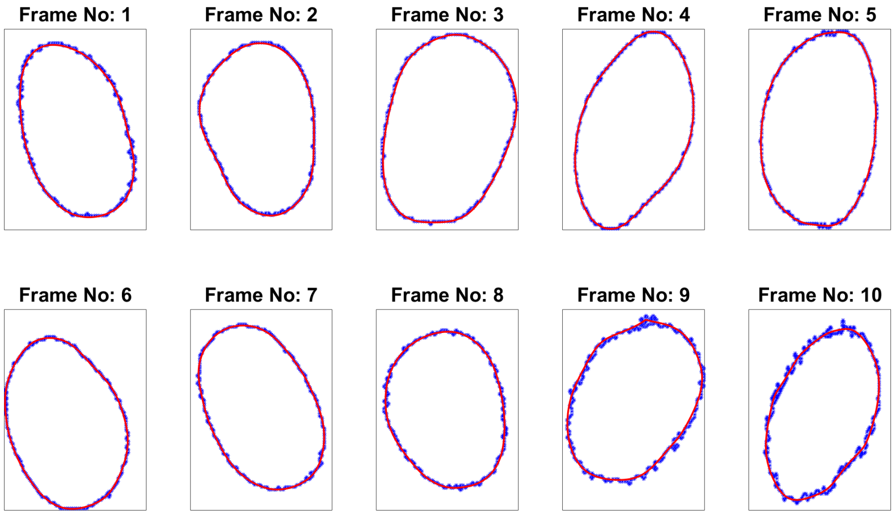


FIGURE 6.133: EFD models of tracked bubbles

| | $a_1$ | $a_2$ | $a_3$ | $a_4$ | $a_5$ | $a_6$ | $a_7$ | $a_8$ |
|---|---|---|---|---|---|---|---|---|
| F:1 | 33.8526 | 0.9609 | 2.3345 | 0.3976 | 0.5393 | 0.2438 | 0.1598 | 0.0836 |
| F:2 | 33.0038 | 1.4321 | 1.6408 | 0.6150 | 0.2815 | 0.1950 | 0.0844 | 0.0470 |
| F:3 | 30.2865 | 0.6445 | 1.2103 | 0.4120 | 0.3086 | 0.2103 | 0.0606 | 0.1044 |
| F:4 | 32.6546 | 0.6189 | 2.2035 | 0.2953 | 0.2531 | 0.0637 | 0.1417 | 0.0837 |
| F:5 | 31.5778 | 0.9410 | 1.6185 | 0.2193 | 0.3644 | 0.1180 | 0.0859 | 0.2413 |
| F:6 | 32.5290 | 0.5329 | 0.8067 | 0.5974 | 0.2084 | 0.1340 | 0.2288 | 0.1385 |
| F:7 | 33.5760 | 0.7897 | 1.5708 | 0.5180 | 0.1133 | 0.1829 | 0.0849 | 0.1422 |
| F:8 | 30.9898 | 0.9159 | 1.0427 | 0.4545 | 0.2481 | 0.2290 | 0.2631 | 0.2092 |
| F:9 | 29.9482 | 2.2563 | 1.7067 | 1.6412 | 0.6507 | 0.5136 | 0.4097 | 0.2946 |
| F:10 | 31.0532 | 2.6633 | 2.3165 | 1.1554 | 0.4405 | 0.5226 | 0.2508 | 0.3844 |

TABLE 6.5: Major axis ($a$) changes of harmonics throughout the tracked frames

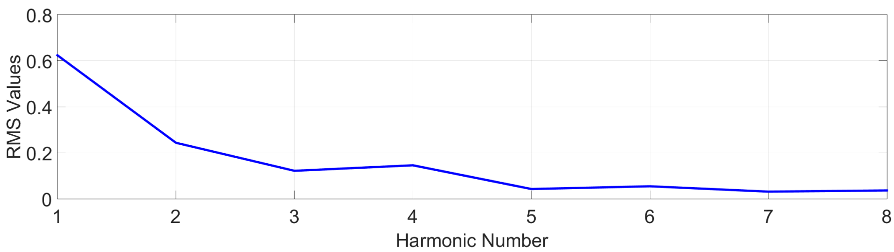


FIGURE 6.134: RMS Values of Covariance Columns for ‘a’

| | $b_1$ | $b_2$ | $b_3$ | $b_4$ | $b_5$ | $b_6$ | $b_7$ | $b_8$ |
|---|---|---|---|---|---|---|---|---|
| F:1 | 23.2721 | 0.5431 | 1.6258 | 0.1433 | 0.2734 | 0.0890 | 0.0384 | 0.0098 |
| F:2 | 24.5008 | 0.3248 | 1.0611 | 0.1799 | 0.2220 | 0.0650 | 0.0535 | 0.0150 |
| F:3 | 25.8599 | 0.3690 | 0.3379 | 0.0073 | 0.1636 | 0.0894 | 0.0045 | 0.0407 |
| F:4 | 22.4055 | 0.1806 | 1.7126 | 0.1467 | 0.0309 | 0.0255 | 0.0482 | 0.0617 |
| F:5 | 25.1667 | 0.6276 | 1.1887 | 0.1420 | 0.1710 | 0.0336 | 0.0245 | 0.1202 |
| F:6 | 26.2798 | 0.1588 | 0.2434 | 0.1006 | 0.0462 | 0.0128 | 0.0131 | 0.0113 |
| F:7 | 23.8678 | 0.2533 | 1.2747 | 0.2434 | 0.0302 | 0.0770 | 0.0232 | 0.0223 |
| F:8 | 25.2412 | 0.7062 | 0.5102 | 0.2857 | 0.2188 | 0.0459 | 0.1559 | 0.1658 |
| F:9 | 24.2780 | 1.4997 | 1.2178 | 0.5265 | 0.0277 | 0.0034 | 0.0702 | 0.0832 |
| F:10 | 22.9713 | 2.3984 | 1.4676 | 1.0569 | 0.2784 | 0.0186 | 0.0448 | 0.1641 |

TABLE 6.6: Minor axis ($b$) changes of harmonics throughout the tracked frames

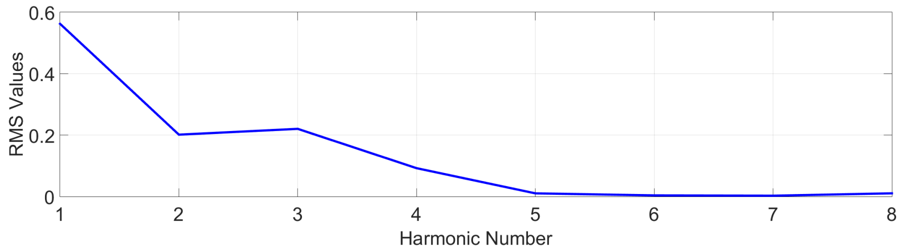


FIGURE 6.135: RMS Values of Covariance Columns for ‘b’

| | $\theta_1$ | $\theta_2$ | $\theta_3$ | $\theta_4$ | $\theta_5$ | $\theta_6$ | $\theta_7$ | $\theta_8$ |
|---|---|---|---|---|---|---|---|---|
| F:1 | 1.9880 | -2.2864 | 3.0946 | 1.5903 | 1.6516 | 1.8567 | 2.2158 | -2.9903 |
| F:2 | 1.7647 | -2.8258 | -2.2045 | 3.0563 | 2.4623 | -2.5798 | -2.6376 | -2.2125 |
| F:3 | -2.3247 | 2.9613 | -3.0414 | -3.0096 | 2.1042 | 1.5201 | -2.2279 | 2.2507 |
| F:4 | -2.7564 | -2.9402 | 2.2061 | 3.0746 | -2.1662 | -2.4891 | -3.0101 | 1.0925 |
| F:5 | -2.9762 | 1.7203 | 0.9862 | 1.8023 | -2.4075 | 2.3115 | 1.9967 | -2.4381 |
| F:6 | 2.4299 | -2.3466 | -1.9703 | -2.0661 | -3.1089 | -2.3555 | -2.2642 | -2.5355 |
| F:7 | 2.0927 | 1.7779 | -2.9428 | -2.0614 | -2.4530 | -2.0230 | 1.7262 | -2.4657 |
| F:8 | 1.8963 | 3.0917 | 1.2690 | -2.3859 | -2.7461 | -2.9633 | 1.8003 | 2.7220 |
| F:9 | 0.8983 | 3.0817 | 2.3170 | -2.9022 | -3.0352 | 2.3415 | -2.4028 | -2.3922 |
| F:10 | -2.6740 | 2.9638 | 1.5619 | 3.1196 | 2.0394 | -2.6102 | -2.8059 | -2.4913 |

TABLE 6.7: Angle in radian ($\theta$) changes of harmonics throughout the tracked frames

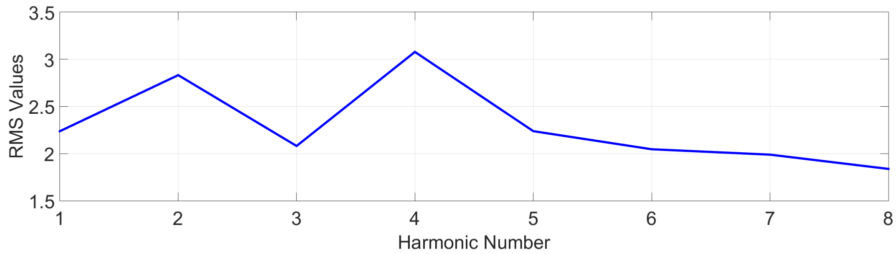


FIGURE 6.136: RMS Values of Covariance Columns for ‘$\theta$’

EFD models of single bubble tracked in Section 6.3.3 are shown in Figure 6.137. Figures 6.138 and 6.139 show that first three harmonics are dominant according to $a$ and $b$ features. Major axis ($a$) is dominant over minor axis ($b$) since bubble changes its elliptic shapes very much during the motion.

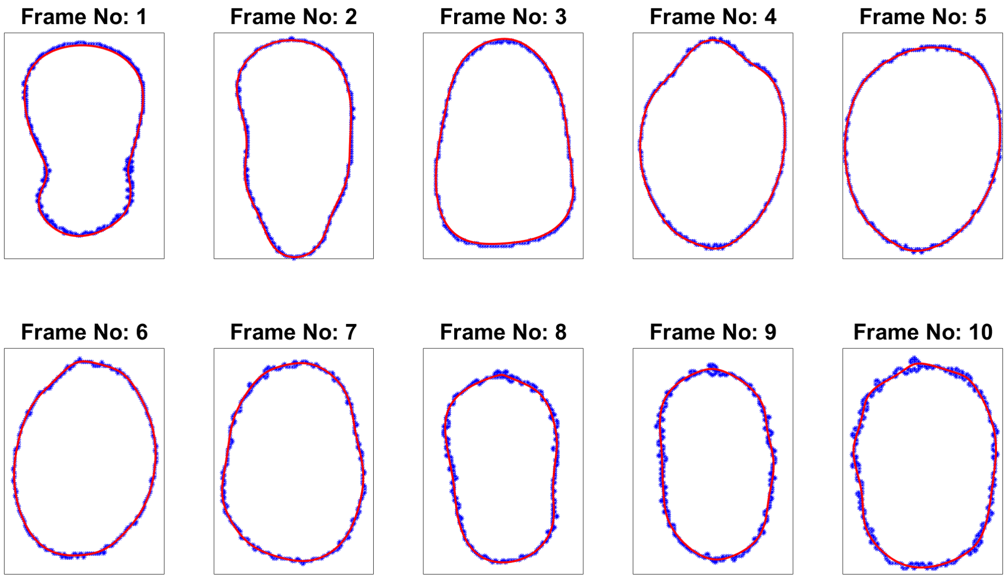


FIGURE 6.137: EFD models of tracked bubbles

| | $a_1$ | $a_2$ | $a_3$ | $a_4$ | $a_5$ | $a_6$ | $a_7$ | $a_8$ |
|---|---|---|---|---|---|---|---|---|
| F:1 | 46.3908 | 3.9728 | 5.7094 | 0.9396 | 0.6278 | 0.5886 | 0.2210 | 0.1908 |
| F:2 | 44.1529 | 2.7603 | 3.3126 | 0.5979 | 0.7522 | 0.5728 | 0.3343 | 0.1857 |
| F:3 | 35.8103 | 2.0737 | 2.2322 | 0.8282 | 0.3273 | 0.2395 | 0.1731 | 0.0783 |
| F:4 | 34.3179 | 0.3009 | 1.9680 | 0.3638 | 0.6593 | 0.3177 | 0.0692 | 0.1461 |
| F:5 | 37.4422 | 0.6215 | 1.7810 | 0.3742 | 0.2292 | 0.0805 | 0.1729 | 0.1103 |
| F:6 | 34.0517 | 0.5102 | 1.6335 | 0.2408 | 0.1914 | 0.1872 | 0.2410 | 0.1169 |
| F:7 | 34.7023 | 1.7639 | 1.3487 | 0.4138 | 0.2649 | 0.4112 | 0.2005 | 0.2302 |
| F:8 | 39.4472 | 2.3941 | 2.1901 | 2.1532 | 0.5147 | 0.5993 | 0.3230 | 0.2544 |
| F:9 | 39.8831 | 2.1997 | 2.4779 | 0.6383 | 0.5512 | 0.3391 | 0.5954 | 0.3016 |
| F:10 | 35.9077 | 2.6640 | 1.4549 | 1.2128 | 0.2742 | 0.2708 | 0.5277 | 0.5011 |

TABLE 6.8: Major axis ($a$) changes of harmonics throughout the tracked frames

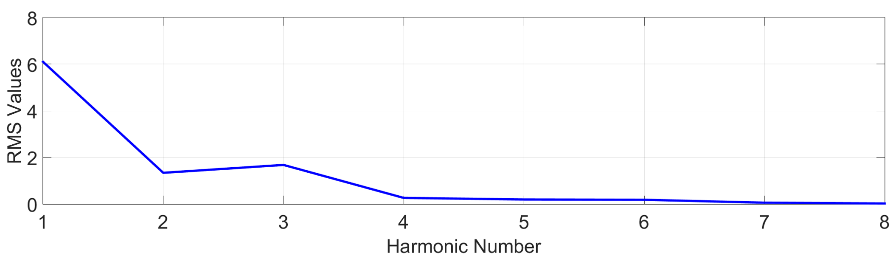


FIGURE 6.138: RMS Values of Covariance Columns for 'a'

| | $b_1$ | $b_2$ | $b_3$ | $b_4$ | $b_5$ | $b_6$ | $b_7$ | $b_8$ |
|---|---|---|---|---|---|---|---|---|
| F:1 | 22.3338 | 2.3399 | 3.7416 | 0.4091 | 0.1799 | 0.3841 | 0.0611 | 0.0690 |
| F:2 | 22.5255 | 0.0773 | 2.8299 | 0.4266 | 0.2348 | 0.3708 | 0.0774 | 0.0852 |
| F:3 | 26.9159 | 0.6529 | 0.8574 | 0.3328 | 0.2630 | 0.0801 | 0.1391 | 0.0420 |
| F:4 | 27.7925 | 0.1753 | 0.7477 | 0.2192 | 0.1383 | 0.2311 | 0.0343 | 0.0887 |
| F:5 | 28.0116 | 0.3134 | 1.3034 | 0.2442 | 0.1015 | 0.0232 | 0.0544 | 0.0108 |
| F:6 | 26.4030 | 0.0826 | 0.9637 | 0.0962 | 0.0736 | 0.0656 | 0.0587 | 0.0875 |
| F:7 | 27.0416 | 0.0311 | 0.4106 | 0.0061 | 0.1467 | 0.1270 | 0.0793 | 0.0812 |
| F:8 | 22.1015 | 0.8724 | 1.6949 | 0.8863 | 0.0787 | 0.2186 | 0.0189 | 0.0497 |
| F:9 | 22.8166 | 1.3505 | 1.8382 | 0.0706 | 0.0958 | 0.2329 | 0.1012 | 0.2160 |
| F:10 | 27.1928 | 1.3363 | 0.1982 | 0.3608 | 0.1999 | 0.0785 | 0.2919 | 0.0606 |

TABLE 6.9: Minor axis ($b$) changes of harmonics throughout the tracked frames

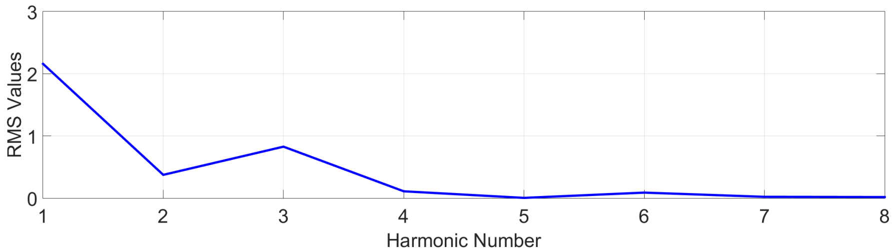


FIGURE 6.139: RMS Values of Covariance Columns for 'b'

| | $\theta_1$ | $\theta_2$ | $\theta_3$ | $\theta_4$ | $\theta_5$ | $\theta_6$ | $\theta_7$ | $\theta_8$ |
|---|---|---|---|---|---|---|---|---|
| F:1 | 1.5892 | 2.1612 | -2.8649 | 1.7005 | 2.2886 | 2.0795 | 2.3023 | 1.2682 |
| F:2 | 1.5905 | -2.7802 | 2.0436 | 2.5130 | -1.9291 | -3.1252 | 2.7689 | -2.7059 |
| F:3 | 1.5783 | 2.9756 | -2.9854 | 1.7908 | 3.0211 | -2.8259 | 1.1444 | 2.0951 |
| F:4 | -3.0390 | -2.4471 | -3.0167 | 1.9577 | 1.5902 | -2.3132 | 1.2006 | -2.8407 |
| F:5 | -3.0371 | 1.6655 | 2.8837 | 1.2081 | -2.6041 | 3.0531 | -2.4503 | 2.1271 |
| F:6 | -2.9962 | 1.9754 | 2.9014 | -2.4934 | 1.5844 | 2.2673 | 1.9671 | 3.0182 |
| F:7 | 1.5704 | 2.9286 | 3.0461 | -2.3328 | 1.2814 | 3.0470 | 2.3697 | -1.9831 |
| F:8 | 1.6138 | 1.9396 | 1.0343 | -2.7763 | 2.7191 | -2.4853 | -2.9659 | 2.1376 |
| F:9 | 1.6277 | 1.4163 | 1.9672 | 2.6387 | 2.7940 | 2.7206 | 2.6999 | 2.6381 |
| F:10 | 1.6450 | 1.8803 | -2.5929 | -2.5046 | 3.0124 | 1.7371 | 2.4362 | 2.7556 |

TABLE 6.10: Angle in radian ($\theta$) changes of harmonics throughout the tracked frames

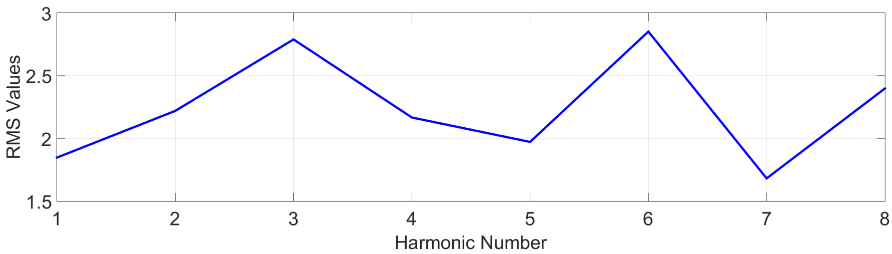


FIGURE 6.140: RMS Values of Covariance Columns for '$\theta$'

EFD models of single bubble tracked in Section 6.3.4 are shown in Figure 6.141. Figures 6.142 and 6.143 show that first four harmonics are dominant according to $a$ and $b$ features. Major axis ($a$) and minor axis ($b$) are equally dominant and with compared to rest of EFD models variance is very much less since bubble don't alter its shape dramatically during the motion.

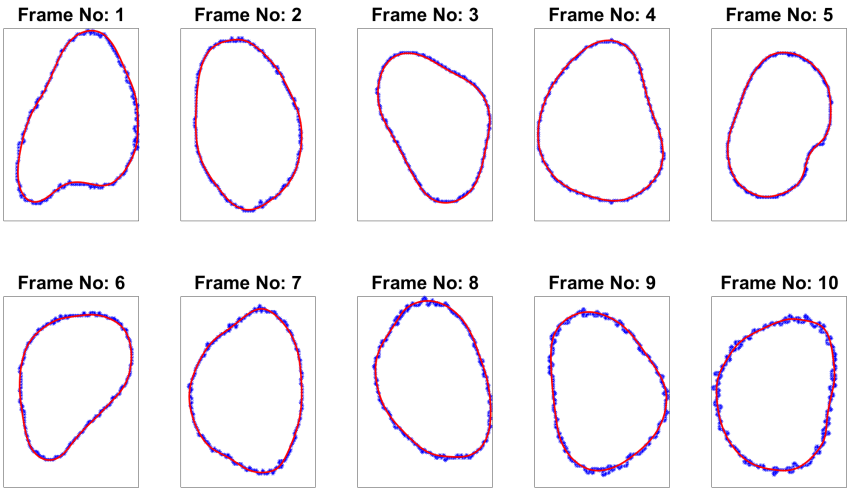


FIGURE 6.141: EFD models of tracked bubbles

| | $a_1$ | $a_2$ | $a_3$ | $a_4$ | $a_5$ | $a_6$ | $a_7$ | $a_8$ |
|---|---|---|---|---|---|---|---|---|
| F:1 | 31.8840 | 3.7984 | 0.8241 | 2.0189 | 0.6916 | 0.3009 | 0.2642 | 0.2816 |
| F:2 | 31.2679 | 1.5541 | 1.2190 | 0.5869 | 0.3569 | 0.2060 | 0.3386 | 0.1409 |
| F:3 | 32.4159 | 2.1695 | 1.7685 | 1.1726 | 0.4321 | 0.1282 | 0.1138 | 0.0544 |
| F:4 | 32.2752 | 2.4397 | 1.2102 | 1.1356 | 0.2806 | 0.1299 | 0.1021 | 0.1143 |
| F:5 | 32.3354 | 1.0127 | 2.0243 | 0.6510 | 0.6406 | 0.3562 | 0.3350 | 0.3346 |
| F:6 | 33.2968 | 2.3787 | 2.0204 | 1.2768 | 0.3148 | 0.4345 | 0.0834 | 0.1665 |
| F:7 | 31.7136 | 2.4428 | 1.8515 | 0.7716 | 0.2741 | 0.2711 | 0.1942 | 0.2021 |
| F:8 | 31.8771 | 1.9298 | 0.4561 | 1.2278 | 0.3895 | 0.4016 | 0.2172 | 0.2483 |
| F:9 | 33.7844 | 2.1801 | 0.7659 | 1.2453 | 0.3833 | 0.3133 | 0.2080 | 0.1843 |
| F:10 | 31.5473 | 2.5485 | 1.5955 | 0.1681 | 0.6694 | 0.1229 | 0.5948 | 0.2640 |

TABLE 6.11: Major axis ($a$) changes of harmonics throughout the tracked frames

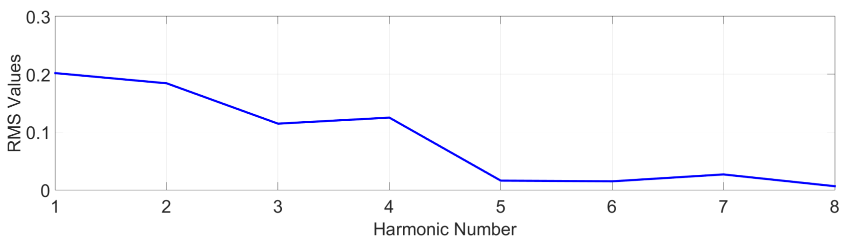


FIGURE 6.142: RMS Values of Covariance Columns for ‘a’

| | $b_1$ | $b_2$ | $b_3$ | $b_4$ | $b_5$ | $b_6$ | $b_7$ | $b_8$ |
|---|---|---|---|---|---|---|---|---|
| F:1 | 22.9447 | 1.7000 | 0.4246 | 1.0606 | 0.2652 | 0.1208 | 0.1433 | 0.1704 |
| F:2 | 25.9578 | 0.3838 | 0.7340 | 0.0116 | 0.1580 | 0.0054 | 0.1096 | 0.0206 |
| F:3 | 24.8102 | 1.3361 | 0.9764 | 0.6631 | 0.1875 | 0.0172 | 0.0218 | 0.0143 |
| F:4 | 27.2298 | 1.0895 | 0.5001 | 0.7102 | 0.0708 | 0.0579 | 0.0247 | 0.0670 |
| F:5 | 26.1694 | 0.0032 | 0.6814 | 0.1617 | 0.3330 | 0.0168 | 0.0098 | 0.0151 |
| F:6 | 23.9426 | 1.4246 | 1.4290 | 0.7738 | 0.2296 | 0.2813 | 0.0551 | 0.1187 |
| F:7 | 25.7185 | 0.7217 | 1.1968 | 0.3586 | 0.0212 | 0.0816 | 0.0212 | 0.0907 |
| F:8 | 25.5860 | 0.3521 | 0.1363 | 0.8362 | 0.0427 | 0.1098 | 0.0188 | 0.1328 |
| F:9 | 24.5585 | 0.9901 | 0.0906 | 0.1827 | 0.2629 | 0.0222 | 0.0934 | 0.0439 |
| F:10 | 26.6423 | 0.6281 | 0.7484 | 0.1300 | 0.1848 | 0.0380 | 0.0674 | 0.1826 |

TABLE 6.12: Minor axis ($b$) changes of harmonics throughout the tracked frames

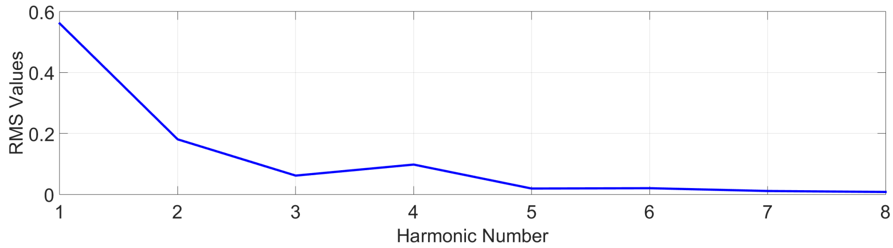


FIGURE 6.143: RMS Values of Covariance Columns for ‘b’

| | $\theta_1$ | $\theta_2$ | $\theta_3$ | $\theta_4$ | $\theta_5$ | $\theta_6$ | $\theta_7$ | $\theta_8$ |
|---|---|---|---|---|---|---|---|---|
| F:1 | -2.7167 | 1.4156 | -2.4709 | 1.5187 | 1.3238 | 1.5755 | -2.8501 | 1.1278 |
| F:2 | 2.7712 | 1.5368 | -2.6921 | 2.8054 | 2.1698 | -3.0275 | 2.7368 | -2.1760 |
| F:3 | 2.2638 | -2.6098 | 1.4908 | -2.4693 | 2.7207 | 2.2313 | 1.8292 | 2.7862 |
| F:4 | 1.6766 | -2.9527 | -2.5710 | -2.5575 | 2.6255 | 2.3748 | 2.5809 | 1.5261 |
| F:5 | -2.3331 | -1.6829 | 2.8404 | 2.8592 | 2.2661 | 2.4876 | 2.4721 | 2.4460 |
| F:6 | -2.6850 | 1.1525 | 2.0717 | 1.3086 | 2.9197 | 2.9735 | 1.1079 | -3.0380 |
| F:7 | 3.1386 | 1.9952 | -2.7382 | 2.0045 | 3.0928 | 2.3858 | -2.1043 | -2.9314 |
| F:8 | 2.3607 | 2.7525 | -3.0207 | 2.9320 | 1.7706 | 2.6121 | 2.6831 | -2.4248 |
| F:9 | 1.7683 | 3.0485 | 2.9405 | -2.9878 | 2.8733 | 1.8329 | -2.2965 | 2.2447 |
| F:10 | 1.3776 | 2.3881 | -2.1152 | 2.5395 | 2.6669 | -2.9857 | -2.2712 | 1.1325 |

TABLE 6.13: Angle in radian ($\theta$) changes of harmonics throughout the tracked frames

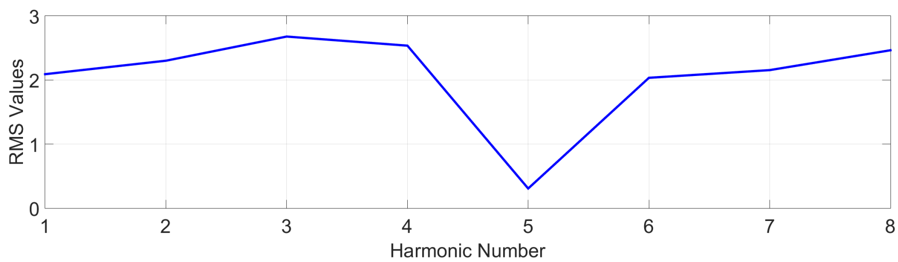


FIGURE 6.144: RMS Values of Covariance Columns for ‘$\theta$’

# Chapter 7

# Conclusion and Future Works

In this thesis, visualization system architectures for multiphase flow imaging is discussed and novel vision based methods to quantify the hydrodynamic cavitating flow and cavitation induced bubbles are proposed. First, analysis of hydrodynamic cavitation flow is performed by processing the images acquired by Particle Shadow Sizing (PSS) technique and bubbles are generated under 10 to 120 bars inlet pressures. During the process of hydrodynamic cavitation, multiphase bubbly flow forms a virtual cone which starts with the orifice and extends through the flow. Virtually obtained cone angle of multiphase flow is estimated through 3D Gaussian modeling and employing a recursive filtering, i.e. Kalman filter, which is a requisite to position the orifice of bubbly cavitating flow generator during biomedical applications. Observed newborn bubbles soon after the orifice of hydrodynamic cavitation generator probe are considered as the most destructive ones and their distributions around main jet flow is determined with the assumption of Gaussian distribution to control their catastrophic effects and estimate the operational area. Second, a new tracking-by-detection method is proposed to track the bubbles and droplets throughout the flow, which is very crucial to investigate the evolution of bubbles and examine the interactions of bubble-bubble and bubble-specimen. Proposed structural and motion characteristics based method is adapted to track single, double and triple bubbles, which enables to clarify the interactions as splitting and merging. Third, tracked single bubbles' contour edges are modeled via elliptic Fourier descriptors to extract the invariant features throughout the evolution. All proposed methods are applied to 8 bit grayscale shadow images acquired by PSS in MATLAB environment.

As a future work, laser induced double frame high speed images can be utilized to visualize the bubbles smaller than $30\mu$. Furthermore proposed methods within this thesis can be extended to explain the evolution of smaller bubbles and interactions.

# Bibliography


[1] A. K. Yetisen and L. R. Volpatti, "Patent protection and licensing in microfluidics," *Lab on a Chip*, vol. 14, no. 13, pp. 2217–2225, 2014.

[2] O. Y. Perk, M. Şeşen, D. Gozuacik, and A. Koşar, "Kidney stone erosion by micro scale hydrodynamic cavitation and consequent kidney stone treatment," *Annals of biomedical engineering*, vol. 40, no. 9, pp. 1895–1902, 2012.

[3] "Dantec Dynamics A/S." `http://www.dantecdynamics.com/`. Accessed: 2015-07-15.

[4] R. P. Feynman, "There's plenty of room at the bottom," *Engineering and science*, vol. 23, no. 5, pp. 22–36, 1960.

[5] B. J. Nelson, L. Dong, and F. Arai, "Micro/nanorobots," in *Springer Handbook of Robotics*, pp. 411–450, Springer, 2008.

[6] O. Reynolds, "An experimental investigation of the circumstances which determine whether the motion of water shall be direct or sinuous, and of the law of resistance in parallel channels.," *Proceedings of the royal society of London*, vol. 35, no. 224-226, pp. 84–99, 1883.

[7] D. Sinton and D. Li, "Microscale flow visualization," in *ASME 2002 International Mechanical Engineering Congress and Exposition*, pp. 137–144, American Society of Mechanical Engineers, 2002.

[8] Z. Itah, O. Oral, O. Y. Perk, M. Sesen, E. Demir, S. Erbil, A. I. Dogan-Ekici, S. Ekici, A. Kosar, and D. Gozuacik, "Hydrodynamic cavitation kills prostate

cells and ablates benign prostatic hyperplasia tissue," *Experimental Biology and Medicine*, p. 1535370213503273, 2013.

[9] C. Mishra and Y. Peles, "Cavitation in flow through a micro-orifice inside a silicon microchannel," *Physics of Fluids (1994-present)*, vol. 17, no. 1, p. 013601, 2005.

[10] H. K. Suh and C. S. Lee, "Effect of cavitation in nozzle orifice on the diesel fuel atomization characteristics," *International journal of heat and fluid flow*, vol. 29, no. 4, pp. 1001–1009, 2008.

[11] M. De Giorgi, A. Ficarella, and M. Tarantino, "Evaluating cavitation regimes in an internal orifice at different temperatures using frequency analysis and visualization," *International Journal of Heat and Fluid Flow*, vol. 39, pp. 160–172, 2013.

[12] R. Payri, F. Salvador, J. Gimeno, and J. De la Morena, "Study of cavitation phenomena based on a technique for visualizing bubbles in a liquid pressurized chamber," *International Journal of Heat and Fluid Flow*, vol. 30, no. 4, pp. 768–777, 2009.

[13] W. Kim, K. Park, J. Oh, J. Choi, and H.-Y. Kim, "Visualization and minimization of disruptive bubble behavior in ultrasonic field," *Ultrasonics*, vol. 50, no. 8, pp. 798–802, 2010.

[14] C. T. Crowe, *Multiphase flow handbook*. CRC press, 2005.

[15] P. Eisenberg, "Cavitation damage," tech. rep., DTIC Document, 1963.

[16] P. R. Gogate and A. B. Pandit, "A review and assessment of hydrodynamic cavitation as a technology for the future," *Ultrasonics sonochemistry*, vol. 12, no. 1, pp. 21–27, 2005.

[17] A. K. Prasad, "Particle image velocimetry," *CURRENT SCIENCE-BANGALORE-*, vol. 79, no. 1, pp. 51–60, 2000.

[18] "Measurement Principles of PIV." `http://www.dantecdynamics.com/measurement-principles-of-piv`. Accessed: 2015-07-15.

[19] C. Brossard, J. Monnier, P. Barricau, F.-X. Vandernoot, Y. Le Sant, F. Champagnat, and G. Le Besnerais, "Principles and applications of particle image velocimetry," *Aerosp Lab J*, vol. 1, pp. 1–11, 2009.

[20] A. Schroeder and C. E. Willert, *Particle image velocimetry: new developments and recent applications*, vol. 112. Springer Science & Business Media, 2008.

[21] A. K. Prasad, "Stereoscopic particle image velocimetry," *Experiments in fluids*, vol. 29, no. 2, pp. 103–116, 2000.

[22] H. Wang and G. Ergin, "Experimental investigation of jet impingement by stereo piv,"

[23] J. Kitzhofer, T. Nonn, and C. Brücker, "Generation and visualization of volumetric piv data fields," *Experiments in fluids*, vol. 51, no. 6, pp. 1471–1492, 2011.

[24] F. Durst, A. Melling, and J. H. Whitelaw, "Principles and practice of laser-doppler anemometry," *NASA STI/Recon Technical Report A*, vol. 76, p. 47019, 1976.

[25] "Measurement Principles of LDA." `http://www.dantecdynamics.com/measurement-principles-of-lda`. Accessed: 2015-07-15.

[26] N. G. Deen, B. H. Hjertager, and T. Solberg, "Comparison of piv and lda measurement methods applied to the gas-liquid flow in a bubble column," in *Proceedings of 10th Int. Symp. on Appl. of Laser Techniques to Fluid Mech.(Lisbon, Portugal, 2000)*, 2000.

[27] "Measurement Principles of PDA." `http://www.dantecdynamics.com/measurement-principles-of-pda`. Accessed: 2015-07-15.

[28] W. Bachalo and M. Houser, "Phase/doppler spray analyzer for simultaneous measurements of drop size and velocity distributions," *Optical Engineering*, vol. 23, no. 5, pp. 235583–235583, 1984.

[29] R. Ray, P. Henshaw, N. Biswas, and C. Sak, “Evaporation of water spray from a rotary bell atomizer using a phase doppler anemometer,” *Atomization and Sprays*, vol. 25, no. 7, 2015.

[30] D. Bell and D. Chapman, “Phase doppler anemometry as an ejecta diagnostic,” *Bulletin of the American Physical Society*, vol. 60, 2015.

[31] “Interferometric Mie Imaging.” `http://www.lavision.de/en/techniques/interferometric-mie-imaging.php`. Accessed: 2015-07-15.

[32] Q. Fu and W. Sun, “Mie theory for light scattering by a spherical particle in an absorbing medium,” *Applied Optics*, vol. 40, no. 9, pp. 1354–1361, 2001.

[33] “Measurement Principles of IPI.” `http://www.dantecdynamics.com/measurement-principles-of-ipi`. Accessed: 2015-07-15.

[34] C. Chao, M. P. Wan, L. Morawska, G. R. Johnson, Z. Ristovski, M. Hargreaves, K. Mengersen, S. Corbett, Y. Li, X. Xie, *et al.*, “Characterization of expiration air jets and droplet size distributions immediately at the mouth opening,” *Journal of Aerosol Science*, vol. 40, no. 2, pp. 122–133, 2009.

[35] A. Graßmann and F. Peters, “Size measurement of very small spherical particles by mie scattering imaging (msi),” *Particle & Particle Systems Characterization*, vol. 21, no. 5, pp. 379–389, 2004.

[36] S. Dehaeck and J. Van Beeck, “Multifrequency interferometric particle imaging for gas bubble sizing,” *Experiments in fluids*, vol. 45, no. 5, pp. 823–831, 2008.

[37] “Shadow Sizing.” `http://www.dantecdynamics.com/shadow-sizing`. Accessed: 2015-07-15.

[38] “Shadowgraphy.” `http://www.lavision.de/en/techniques/shadowgraphy.php`. Accessed: 2015-07-15.

[39] J. Estevadeordal and L. Goss, “Piv with led: particle shadow velocimetry (psv),” in *43rd AIAA aerospace sciences meeting and exhibit, meeting papers*, pp. 12355–12364, 2005.

[40] S. Khodaparast, N. Borhani, G. Tagliabue, and J. R. Thome, "A micro particle shadow velocimetry ($\mu$psv) technique to measure flows in microchannels," *Experiments in fluids*, vol. 54, no. 2, pp. 1–13, 2013.

[41] A. Kitagawa, K. Hishida, and Y. Kodama, "Flow structure of microbubble-laden turbulent channel flow measured by piv combined with the shadow image technique," *Experiments in Fluids*, vol. 38, no. 4, pp. 466–475, 2005.

[42] "Shadow Probe." `http://www.dantecdynamics.com/shadowstrobe`. Accessed: 2015-07-15.

[43] N. Otsu, "A threshold selection method from gray-level histograms," *Automatica*, vol. 11, no. 285-296, pp. 23–27, 1975.

[44] J. Kittler and J. Illingworth, "On threshold selection using clustering criteria," *Systems, Man and Cybernetics, IEEE Transactions on*, no. 5, pp. 652–655, 1985.

[45] J. Canny, "A computational approach to edge detection," *Pattern Analysis and Machine Intelligence, IEEE Transactions on*, no. 6, pp. 679–698, 1986.

[46] Y.-L. Chang and X. Li, "Adaptive image region-growing," *Image Processing, IEEE Transactions on*, vol. 3, no. 6, pp. 868–872, 1994.

[47] M. Kass, A. Witkin, and D. Terzopoulos, "Snakes: Active contour models," *International journal of computer vision*, vol. 1, no. 4, pp. 321–331, 1988.

[48] D. Peng, B. Merriman, S. Osher, H. Zhao, and M. Kang, "A pde-based fast local level set method," *Journal of Computational Physics*, vol. 155, no. 2, pp. 410–438, 1999.

[49] L. A. Vese and T. F. Chan, "A multiphase level set framework for image segmentation using the mumford and shah model," *International journal of computer vision*, vol. 50, no. 3, pp. 271–293, 2002.

[50] X.-F. Wang, D.-S. Huang, and H. Xu, "An efficient local chan–vese model for image segmentation," *Pattern Recognition*, vol. 43, no. 3, pp. 603–618, 2010.

[51] W. Blanz and S. L. Gish, "A connectionist classifier architecture applied to image segmentation," in *Pattern Recognition, 1990. Proceedings., 10th International Conference on*, vol. 2, pp. 272–277, IEEE, 1990.

[52] E. Trauwaert, L. Kaufman, and P. Rousseeuw, "Fuzzy clustering algorithms based on the maximum likelihood priciple," *Fuzzy Sets and Systems*, vol. 42, no. 2, pp. 213–227, 1991.

[53] F. Kettaf, D. Bi, D. Beauville, and J. Asselin, "A comparison study of image segmentation by clustering techniques," in *Signal Processing, 1996., 3rd International Conference on*, vol. 2, pp. 1280–1283, IEEE, 1996.

[54] A. Yilmaz, O. Javed, and M. Shah, "Object tracking: A survey," *Acm computing surveys (CSUR)*, vol. 38, no. 4, p. 13, 2006.

[55] V. Salari and I. K. Sethi, "Feature point correspondence in the presence of occlusion," *IEEE Transactions on Pattern Analysis & Machine Intelligence*, no. 1, pp. 87–91, 1990.

[56] C. J. Veenman, M. J. Reinders, and E. Backer, "Resolving motion correspondence for densely moving points," *Pattern Analysis and Machine Intelligence, IEEE Transactions on*, vol. 23, no. 1, pp. 54–72, 2001.

[57] T. J. Broida and R. Chellappa, "Estimation of object motion parameters from noisy images," *Pattern Analysis and Machine Intelligence, IEEE Transactions on*, no. 1, pp. 90–99, 1986.

[58] C. Rago, P. Willett, and R. Streit, "A comparison of the jpdaf and pmht tracking algorithms," in *Acoustics, Speech, and Signal Processing, 1995. ICASSP-95., 1995 International Conference on*, vol. 5, pp. 3571–3574, IEEE, 1995.

[59] R. L. Streit and T. E. Luginbuhl, "Maximum likelihood method for probabilistic multihypothesis tracking," in *SPIE's International Symposium on Optical Engineering and Photonics in Aerospace Sensing*, pp. 394–405, International Society for Optics and Photonics, 1994.

[60] D. Comaniciu and P. Meer, "Mean shift: A robust approach toward feature space analysis," *Pattern Analysis and Machine Intelligence, IEEE Transactions on*, vol. 24, no. 5, pp. 603–619, 2002.

[61] J. Shi and C. Tomasi, "Good features to track," in *Computer Vision and Pattern Recognition, 1994. Proceedings CVPR'94., 1994 IEEE Computer Society Conference on*, pp. 593–600, IEEE, 1994.

[62] H. Tao, H. S. Sawhney, and R. Kumar, "Object tracking with bayesian estimation of dynamic layer representations," *Pattern Analysis and Machine Intelligence, IEEE Transactions on*, vol. 24, no. 1, pp. 75–89, 2002.

[63] M. J. Black and A. D. Jepson, "Eigentracking: Robust matching and tracking of articulated objects using a view-based representation," *International Journal of Computer Vision*, vol. 26, no. 1, pp. 63–84, 1998.

[64] S. Avidan, "Support vector tracking," *Pattern Analysis and Machine Intelligence, IEEE Transactions on*, vol. 26, no. 8, pp. 1064–1072, 2004.

[65] A. Blake and M. Isard, *Active contours: the application of techniques from graphics, vision, control theory and statistics to visual tracking of shapes in motion.* Springer Science & Business Media, 2012.

[66] M. Bertalmio, G. Sapiro, and G. Randall, "Morphing active contours," *Pattern Analysis and Machine Intelligence, IEEE Transactions on*, vol. 22, no. 7, pp. 733–737, 2000.

[67] R. Ronfard, "Region-based strategies for active contour models," *International journal of computer vision*, vol. 13, no. 2, pp. 229–251, 1994.

[68] D. P. Huttenlocher, J. J. Noh, and W. J. Rucklidge, "Tracking non-rigid objects in complex scenes," in *Computer Vision, 1993. Proceedings., Fourth International Conference on*, pp. 93–101, IEEE, 1993.

[69] K. Sato and J. K. Aggarwal, "Temporal spatio-velocity transform and its application to tracking and interaction," *Computer Vision and Image Understanding*, vol. 96, no. 2, pp. 100–128, 2004.

[70] J. Kang, I. Cohen, and G. Medioni, "Continuous tracking within and across camera streams," in *Computer Vision and Pattern Recognition, 2003. Proceedings. 2003 IEEE Computer Society Conference on*, vol. 1, pp. I–267, IEEE, 2003.

[71] H. Yang, L. Shao, F. Zheng, L. Wang, and Z. Song, "Recent advances and trends in visual tracking: A review," *Neurocomputing*, vol. 74, no. 18, pp. 3823–3831, 2011.

[72] S. K. Zhou, R. Chellappa, and B. Moghaddam, "Visual tracking and recognition using appearance-adaptive models in particle filters," *Image Processing, IEEE Transactions on*, vol. 13, no. 11, pp. 1491–1506, 2004.

[73] A. D. Jepson, D. J. Fleet, and T. F. El-Maraghi, "Robust online appearance models for visual tracking," *Pattern Analysis and Machine Intelligence, IEEE Transactions on*, vol. 25, no. 10, pp. 1296–1311, 2003.

[74] X. Li, W. Hu, Z. Zhang, X. Zhang, and G. Luo, "Robust visual tracking based on incremental tensor subspace learning," in *Computer Vision, 2007. ICCV 2007. IEEE 11th International Conference on*, pp. 1–8, IEEE, 2007.

[75] Z. Kalal, K. Mikolajczyk, and J. Matas, "Tracking-learning-detection," *Pattern Analysis and Machine Intelligence, IEEE Transactions on*, vol. 34, no. 7, pp. 1409–1422, 2012.

[76] R. T. Collins, Y. Liu, and M. Leordeanu, "Online selection of discriminative tracking features," *Pattern Analysis and Machine Intelligence, IEEE Transactions on*, vol. 27, no. 10, pp. 1631–1643, 2005.

[77] H. Grabner and H. Bischof, "On-line boosting and vision," in *Computer Vision and Pattern Recognition, 2006 IEEE Computer Society Conference on*, vol. 1, pp. 260–267, IEEE, 2006.

[78] D.-C. Cheng and H. Burkhardt, "Bubble tracking in image sequences," *International Journal of Thermal Sciences*, vol. 42, no. 7, pp. 647–655, 2003.

[79] A. Tomiyama, Y. Makino, and I. Zun, "Bubble tracking simulation of interaction among bubbles in a bubbly upflow," in *International conference on computational modelling of free and moving boundary problems*, pp. 171–180, 1999.

[80] T. Okawa, Y. Suzuki, I. Kataoka, M. Aritomi, and M. Mori, "Numerical implementation of interfacial drag force for one-dimensional, two-way bubble tracking method," *Journal of nuclear science and technology*, vol. 37, no. 4, pp. 387–396, 2000.

[81] A. S. Basu, "Droplet morphometry and velocimetry (dmv): a video processing software for time-resolved, label-free tracking of droplet parameters," *Lab on a Chip*, vol. 13, no. 10, pp. 1892–1901, 2013.

[82] C. Jüngst, M. J. Winterhalder, and A. Zumbusch, "Fast and long term lipid droplet tracking with cars microscopy," *Journal of biophotonics*, vol. 4, no. 6, pp. 435–441, 2011.

[83] X. Qian, H. Zhu, X. Yu, and G. Chen, "Genetic algorithm based bubble matching and tracking in aerated water flows," in *Intelligent Control and Automation, 2004. WCICA 2004. Fifth World Congress on*, vol. 3, pp. 2146–2148, IEEE, 2004.

[84] T. Xue, L. Qu, and B. Wu, "Matching and 3-d reconstruction of multibubbles based on virtual stereo vision," *Instrumentation and Measurement, IEEE Transactions on*, vol. 63, no. 6, pp. 1639–1647, 2014.

[85] H. Bilen and M. Unel, "Micromanipulation using a microassembly workstation with vision and force sensing," in *Advanced Intelligent Computing Theories and Applications. With Aspects of Theoretical and Methodological Issues*, pp. 1164–1172, Springer, 2008.

[86] H. Bilen, M. Hocaoglu, E. Baran, M. Unel, D. Gozuacik, *et al.*, "Novel parameter estimation schemes in microsystems," in *Robotics and Automation, 2009. ICRA'09. IEEE International Conference on*, pp. 2394–2399, IEEE, 2009.

[87] H. Bilen, M. A. Hocaoglu, M. Unel, and A. Sabanovic, "Developing robust vision modules for microsystems applications," *Machine Vision and Applications*, vol. 23, no. 1, pp. 25–42, 2012.

[88] P. S. Maybeck, *Stochastic models, estimation, and control*, vol. 3. Academic press, 1982.

[89] R. E. Kalman, "A new approach to linear filtering and prediction problems," *Journal of Fluids Engineering*, vol. 82, no. 1, pp. 35–45, 1960.

[90] R. C. Gonzalez and R. E. Woods, "Digital image processing 3rd edition," 2007.

[91] E. R. Dougherty, R. A. Lotufo, and T. I. S. for Optical Engineering SPIE, *Hands-on morphological image processing*, vol. 71. SPIE press Bellingham, 2003.

[92] J. Serra, *Image analysis and mathematical morphology.* Academic Press, Inc., 1983.

[93] H. O. Lancaster, *Chi-Square Distribution.* Wiley Online Library, 1969.

[94] T. Kailath, "The divergence and bhattacharyya distance measures in signal selection," *Communication Technology, IEEE Transactions on*, vol. 15, no. 1, pp. 52–60, 1967.

[95] F. P. Kuhl and C. R. Giardina, "Elliptic fourier features of a closed contour," *Computer graphics and image processing*, vol. 18, no. 3, pp. 236–258, 1982.